University of New Mexico
UNM Digital Repository

Physics & Astronomy ETDs | Electronic Theses and Dissertations

9-1-2015

High Data-Rate Atom Interferometry for Measuring Dynamic Inertial Conditions

Akash Rakholia

Follow this and additional works at: https://digitalrepository.unm.edu/phyc_etds

Recommended Citation
Rakholia, Akash. "High Data-Rate Atom Interferometry for Measuring Dynamic Inertial Conditions." (2015).
https://digitalrepository.unm.edu/phyc_etds/55

This Dissertation is brought to you for free and open access by the Electronic Theses and Dissertations at UNM Digital Repository. It has been accepted for inclusion in Physics & Astronomy ETDs by an authorized administrator of UNM Digital Repository. For more information, please contact disc@unm.edu.

Akash Rakholia

Candidate

Physics

Department

This dissertation is approved, and it is acceptable in quality and form for publication:

Approved by the Dissertation Committee:

Grant Biedermann , Chairperson

Carlton Caves

Ivan Deutsch

Peter Schwindt

High Data-Rate Atom Interferometry for Measuring Dynamic Inertial Conditions

by

Akash Vrijlal Rakholia

B.S., Physics, Harvey Mudd College, 2009

DISSERTATION

Submitted in Partial Fulfillment of the
Requirements for the Degree of

Doctor of Philosophy
Physics

The University of New Mexico

Albuquerque, New Mexico

July 2015

Dedication

To my family, for their unwavering support and encouragement.

"Science is a way of thinking much more than it is a body of knowledge." – Carl Sagan

Acknowledgments

This work would not have succeeded without the contributions and experience of my fellow scientists at Sandia. I am of course indebted to my advisor, Grant Biedermann, for his guidance and expertise. The project surely would not have succeeded without his knowledge and experience in the field of atom interferometry. Beyond his technical skill in cold atom physics, I find myself fortunate to have an advisor who spent so much of his time and energy in the laboratory.

I started in lab working with graduate student Thomas Loyd who instructed me in the fundamentals of laser system construction and magneto-optical traps. I thank him for getting me started in my first venture into modern experimental physics. Hayden McGuinness joined the lab as a postdoc under the project which forms the bulk of this work. I thank him for being an excellent mentor who solidified my understanding between theory and experiment, as well as his guidance towards our first paper. I will certainly miss our poker games. Yuan-Yu "Superman" Jau provided a rare mix of theoretical and experimental expertise which I have come to admire. I always found our discussions to be enlightening, especially those outside the context of our work. The closed loop interferometer demonstration would not have succeeded without the collaboration of Draper scientists Rick Stoner, Dave Johnson, and Dave Butts.

I surely would not have enjoyed my time in lab as much without the companionship of graduate students Aaron Hankin and Andrew Ferdinand. In particular, I found Aaron Hankin to be highly motivated and approachable. I would also like to thank the remaining members of our group, Paul Parazzoli, James Chou, Cort Johnson, Peter Schwindt, George Burns for their contributions and insight. My time at Sandia overlapped with graduate students Francisco Benito and Boyan Tabakov. In fact, we found ourselves working on our dissertations simultaneously, and were able to keep each other motivated to finish. My experience at Sandia would not be complete without the support of other members of my organization, including John Sterk, Anthony Colombo, Todd Barrick, Kevin Fortier, Micheal Mangan, Amber Young, Susan Clark, and Rob Boye. In particular, John Sterk was always willing to discuss whatever random discrete mathematical problem I was fixated on.

I would like to thank Ivan Deutsch for enabling me to work at Sandia my first year. I also thank Ivan and Carl Caves for their time as my academic advisors. I found their lectures in class to be engaging, and I was happy for their support when I needed clarification or was pursuing lecture topics further.

I will never be able to repay the debt to my parents, Vrijlal and Kailas, who sacrificed so much so that my brother Milap and I could enjoy a comfortable life. From a young age, they always supported my education to the maximal degree, motivating me to pursue a career in science. I am also fortunate to have a large and close extended family who are a source of constant encouragement.

The bulk of this work was funded by Sandia National Laboratories [1] through the Laboratory Directed Research and Development program. I found the program to be sufficiently structured to motivate our work, while being flexible enough to enable other veins of research, for which I am thankful. Additional funding provided by DARPA [2].

High Data-Rate Atom Interferometry for Measuring Dynamic Inertial Conditions

by

Akash Vrijlal Rakholia

B.S., Physics, Harvey Mudd College, 2009

Ph.D., Physics, University of New Mexico, 2015

Abstract

Light pulse atom interferometers have demonstrated remarkable sensitivity and stability for acceleration and rotation rate measurement. However, typical manifestations are designed for laboratory environments and thus rely on a fixed magnitude and direction of gravity, and limited ambient rotation rate. We have enhanced the application space of atom interferometers towards more dynamic environments, with special attention for inertial navigation.

I present our work in the domain of short time-of-flight atom interferometry, whereby the magnitude of ensemble excursion is constrained. The limited interrogation time results in a significant loss of sensitivity. We recover a fraction of the lost sensitivity by operating with an enhanced duty-cycle and data-rate. To demonstrate this concept, we construct an atom interferometer accelerometer capable of operating at data-rates as high as 300 Hz with sensitivities at $\mu g/\sqrt{\text{Hz}}$ levels, which represents a competitive figure for inertial navigation application.

For the bulk of this work, we demonstrate a dual-axis sensor capable of simultaneous acceleration and rotation-rate measurements. The sensor relies on a technique

we refer to as "ensemble exchange" which provides a high flux source of ultracold atoms by swapping atomic ensembles between two MOTs. We achieve a steady-state atom number of 7×10^6 atoms/shot using a minimal loading time of a few milliseconds each shot. Furthermore, we find this technique to be robust under dynamic conditions as large as 10 g of acceleration and 20 rad/s of rotation rate, representing a significant enhancement in ultra-cold atom sample preparation.

The sensor achieves $\mu g/\sqrt{\text{Hz}}$ and $\mu\text{rad/s}/\sqrt{\text{Hz}}$ sensitivities, making this technique a compelling prospect for inertial navigation applications. Through the use of auxiliary cosensors and a real-time combinatorial loop with feedforward and feedback mechanisms, we demonstrate an unprecedented enhancement of the sensor dynamic range up to ± 20 mg. Finally, I will discuss a novel manifestation of short time-of-flight atom interferometry in a warm atomic vapor, which avoids the complication of cold sample preparation and has the potential for significantly simplified laser systems.

Contents

List of Figures

List of Tables

Glossary

Ω_{eff}	Two-photon effective Rabi Frequency.
$\mathbf{k}_{\text{eff}}$	Effective Raman wavevector.
Δ	Optical detuning. Also single-photon detuning.
δ	Microwave (hyperfine) detuning. Also two-photon detuning.
T	Interferometer interrogation time.
$\mathcal{T}$	Ensemble temperature.
g	Standard gravity. Defined as 9.80665 m/s^2 in ISO 80000-3:2006 [3].
APD	Avalanche PhotoDiode
AOM	Acousto-Optic Modulator.
EOM	Electro-Optic Modulator.
MOT	Magneto-Optical Trap.
FPGA	Field-Programmable Gate Array.
DDS	Direct Digital Synthesizer.
VHDL	Very high speed integrated circuit Hardware Description Language

Chapter 1

Introduction

Since the de Broglie hypothesis, and subsequent Davisson-Germer experiment, atom interferometry has proven to be a useful tool for fundamental tests of quantum mechanics and precision metrology [4]. Modern techniques involve using pulses of light to impart a specific and controlled momentum recoil, in order to coherently separate, redirect, and recombine atomic wavepackets [5, 6]. One particular application space involves precise measurement of an atom's inertial dynamics, i.e. acceleration and rotation.

An atom in vacuum is an exquisite inertial reference. A long mean free path ensures the kinematics are purely Newtonian. Atom interferometers seek to exploit this inherent stability for a precise measurement of the atom's motion under gravity or the motion of the platform with respect to the atom. Such techniques have yielded a wide variety of applications, including gravimetry [7], gravity gradiometry [8, 9], seismology [10], near-surface force characterization [11, 12], and inertial navigation [13, 14]. Other more fundamental applications have been suggested including measurement of the fine-structure constant [15, 16], measurement of the Newtonian gravitational constant G [17, 18, 19, 20], gravitational wave detection [21, 22], and tests of the equivalence principle [23, 24, 25]. There are also many

proposed experiments for atom interferometers in space [26, 27, 28]. In this work, we are primarily concerned with adapting light pulse atom interferometry towards a field-worthy navigation-grade inertial sensor.

1.1 Atom Interferometry

The most basic light pulse atom interferometer uses Doppler-sensitive Raman transitions [29] in a $\pi/2 - \pi - \pi/2$ pulse configuration to coherently separate, redirect, and recombine atomic wavepackets. The stimulated Raman transition drives atomic population between two typically long lived states via an intermediary interaction state. In the Doppler-sensitive configuration, the lasers are aligned such that the net photon recoil is on the order of the intermediary state, which is typically that of an optical photon. This enables the atomic wavefunction to separate beyond several times its de Broglie wavelength, while maintaining state coherence.

The concept behind the Doppler-sensitive Raman transition and construction of the interferometer is shown in Fig. 1.1. A $\pi/2$ pulse refers to a Doppler-sensitive Raman pulse tuned such that the atomic state is driven to an equal superposition of ground and excited state. The excited state arm of the interferometer receives an additional momentum recoil of $\hbar\mathbf{k}_{\text{eff}}$, where $\mathbf{k}_{\text{eff}}$ is the effective Raman wavevector. This causes the states to separate spatially and coherently over time. After some interrogation time T, a π pulse inverts the atomic populations, such that the the states are redirected towards one another. After another period of T, a final $\pi/2$ pulse recombines the wavepackets, forming the interferometer.

At each pulse, the optical phase of the laser is imprinted onto the atomic state. This phase is a function of the frequency of the laser, time, the wavevector of the laser, and position. With this pulse configuration, the frequency and time components drop out, and the result is a position-dependent phase encoded in the atomic state of the

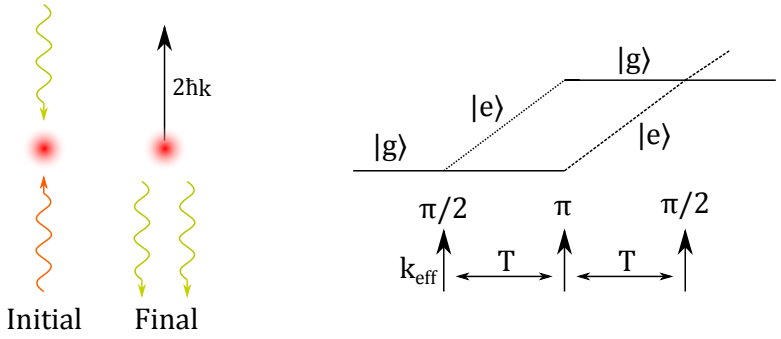

Figure 1.1: Concept behind the Doppler-sensitive Raman transition and light pulse atom interferometer. Left: The stimulated Raman transition drives atomic population between two states via a third intermediary state. In the Doppler-sensitive configuration, the atom absorbs from one of the optical fields and emits into the other, in the opposing direction. This results in a net momentum recoil, the magnitude of which is twice the photon recoil from each field. Right: By using a $\pi/2 - \pi - \pi/2$ pulse sequence of these transition, we coherently and precisely separate, redirect, and recombine atomic wavepackets, forming the interferometer.

atom. To first order, the phase shift is given by

$$\Delta\phi = \mathbf{k}_{\text{eff}} \cdot (\mathbf{a} - 2\mathbf{v} \times \mathbf{\Omega})T^2, \tag{1.1}$$

where $\mathbf{a}$ is the acceleration of the atoms, $\mathbf{\Omega}$ is the rotation rate, and $\mathbf{v}$ is the initial velocity. A precise readout of the phase $\Delta\phi$ results in a precise determination of $\mathbf{a}$ and $\mathbf{\Omega}$. The fundamental limit of phase readout is given by the shot noise limit $1/\sqrt{N}$, where N is the number of atoms participating in the interferometer. Furthermore, the sensitivity scales as the square of the interrogation time T. Thus, atom interferometers typically use cold atomic ensembles prepared by magneto-optical traps [30], which have been demonstrated to be a robust and adaptable source of ultracold atoms. Atomic fountains are often employed, which launch the atoms in the vertical direction and allowing them to fall under gravity, increasing the total available interrogation time. Typical implementations use cold atomic ensembles with on the order of a million atoms and an interrogation time on the order of a couple hundred milliseconds, resulting in a sensitivity on the order of 10 n$g/\sqrt{\text{Hz}}$. The most sensitive

atom interferometer uses a 10 m tall vacuum chamber to increase the interrogation time to 1 s, achieving an inferred sensitivity of 6.7×10^{-12} g per shot [31, 32]. Similar to atomic clocks, these systems have also demonstrated remarkable stability [33, 20]. These systems may also be configured as gyroscopes by using a flux of atoms either from an atomic beam [34] or fountain-launched cold atom ensembles [13].

These atom interferometers are typically designed for a laboratory environment in which the direction and magnitude of acceleration (including gravity) and rotation rate (including Earth's rotation) are fairly constant. This poses a number of challenges for adapting such a technology for inertial navigation applications where the inertial conditions are far more dynamic. To better understand some of these challenges, we present a brief overview of inertial navigation technology and requirements.

1.2 Inertial Navigation

Inertial navigation refers to a technique which dynamically calculates the position and velocity of a moving object using accelerometers and gyroscopes without the need for an external reference [35]. Typical applications involve navigation for ships, aircraft, spacecraft, and guided missiles. The acceleration and rotation rate from the sensors are integrated twice to deduce the position. Thus, the error is proportional to the square of time. For long travel times, highly sensitive and stable accelerometers and gyroscopes are imperative.

The first use of inertial navigation is generally considered to be in 1942 by the German V-2 missile [37]. While the sensor technology consisting of mechanical accelerometers and gyroscopes had been available for decades, this was the first application combining the sensors for full navigational information. The first of such systems were gimballed [36]. A set of motorized gimbals stabilizes the inertial plat-

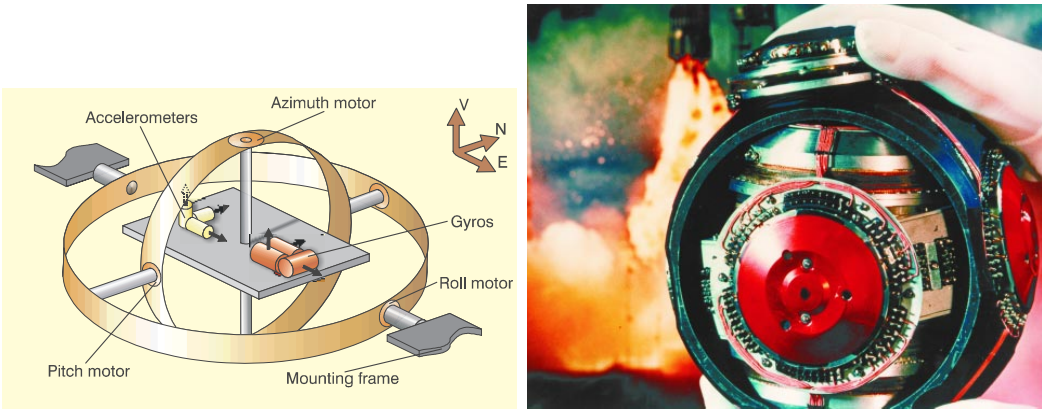

Figure 1.2: Concept and implementation of a gimballed inertial measurement unit. Figures from [36]. Left: A set of gimbals keeps an accelerometer and gyroscope relatively stable using inertial information derived from the sensors. Right: Picture of a Marconi FIN1000 inertial platform.

form upon which the accelerometer and gyroscope are mounted. Feedback from the accelerometer and gyroscope is directed to the motorized gimbals.

However, there are a number of limitations to gimballed systems in terms of mechanical complexity. The gimbals add sources of complication such as extra motors, thermal drift, and mechanical resonances. A strapdown system is desirable, where the accelerometer and gyroscope share the same inertial frame as the target vehicle. However, to accommodate this the sensors must have the same performance as before, but with an increased dynamic range by about 10^5.

The enabling technology for strapdown systems was the ring laser gyroscope (RLG) [36]. First demonstrated in 1963 [38], the RLG consists of a cyclic optical resonator having two counter-propagating lasers over the same path. In what is known as the Sagnac effect [39], rotations induce a small difference in the time it takes each path to propagate through the cycle. This causes a tiny shift in the frequency of the two laser paths, resulting in a standing wave moving around the ring which may be detected. The fiber optic gyroscope (FOG) works on a similar principle except the light is injected into an optical fiber circuit from an external

coherent source [40]. This technology represents the state of the art in inertial navigation, and development of this technology is still proceeding. A high performance modern inertial navigation system achieves a sensitivity at 1 mdeg/$\sqrt{\text{Hr}}$ levels [36], or approximately 0.3 μrad/s/$\sqrt{\text{Hz}}$, stable for 1 hr. A navigation grade accelerometer achieves a bias error on the order of 10 μg [36]. This provides a metric by which we will evaluate the performance of our sensor.

Since the advent of GPS, it has proven to be a reliable, robust, and economical method for navigation, even down to the consumer level. Nevertheless, there remain applications where an alternative to GPS is desirable [35]. First, GPS operates at frequency bands in the GHz range, which are susceptible to jamming. Secondly, GPS doesn't operate in space beyond the network of satellites, which orbit at $20,000$ kilometers. Finally, while GPS has been demonstrated to be highly robust, a backup option is desirable.

1.3 Measurement Overview

The requirements for a successful inertial navigation system are high sensitivity, high stability, large dynamic range, and compact size [36]. Atom interferometers have clearly demonstrated the first two. The inertial sensitivity of atom interferometers remains unparallelled. The stability of such systems derives from that of cold atomic fountain clocks [41], which have since become the de-facto standard for timekeeping in the United States [42, 43] and around the world [44, 45]. Recent developments in optical transition based clocks [46, 47] have surpassed the performance in microwave-based clocks. Furthermore, compact atomic clock devices have been proposed [48, 49] and successfully demonstrated [50, 51]. As an added advantage the system requires no external calibration, as the scale factor ultimately derives from a well-known and fixed atomic transition. Because of these merits, there is great interest in adapting atom interferometers for field use [9, 52, 53, 54, 55].

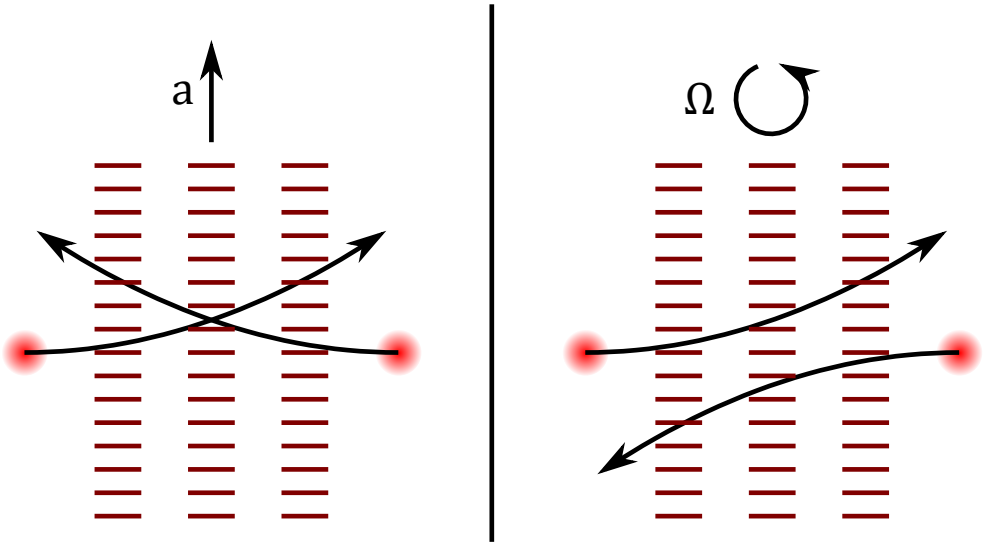

Figure 1.3: Concept behind the dual-axis atom interferometer. Two atomic ensembles are launched towards one-another. During the trajectory of the ensembles, the optical phase of the laser is imprinted onto the atomic state. The laser functions analogous to a ruler, encoding inertial information into this phase. A readout of this phase corresponds to a measurement of the curvature of the path. This curvature contains information of both the acceleration and rotation rate. In the case of an acceleration, the ensembles displace in the same direction, and oppositely for rotations, enabling us to decouple the signals.

Unfortunately, large dynamic range and compact size remain elusive. Indeed, to achieve many of these advantages atom interferometers are configured under laboratory conditions with a fixed direction of gravity and limited dynamic conditions. In particular, the ballistic trajectory of the ensemble remains largely constant over a distance of centimeters or even meters. Furthermore, the length of the trajectory requires the use of large vacuum chambers. We seek to address both of these issues by moving to a small time-of-flight.

To restrict the displacement of the ensemble during a ballistic trajectory, we limit the time-of-flight (ToF) to a few milliseconds [56, 57]. This prevents excessive excursion of the ensemble even under dynamic conditions. However, this significantly reduces the sensitivity of the interferometer, due to the T^2 scaling of the atomic phase

shift. As such, it is imperative to maximize the bandwidth of the interferometer and recover some of the lost sensitivity. However, MOTs typically take 100s of milliseconds to load a significant atomic ensemble from vapor. Compared with a few milliseconds of interrogation, this severely limits the duty cycle and thus the potential performance of our apparatus. Fortunately, the short time-of-flight enables us to employ recapture [58].

As stated earlier, by limiting the time-of-flight to a few milliseconds, even under $\sim 1\ g$ of acceleration the atomic ensemble is still well within the capture volume of the MOT. Thus, by enabling the trap immediately after the experiment, we are able to *recapture* a significant proportion of the ensemble ($\sim 90\%$) into the MOT. This significantly reduces the time required to load atoms for the next shot of the experiment. In fact, we are able to achieve a comparable atom number ($\sim 10^6$) to many cold atom experiments by only loading for a few milliseconds each shot. This significantly increases the duty cycle from less than 5% to above 50%.

Our first apparatus thus employed recapture to operate a high data-rate atom interferometer accelerometer. For this device, we were only concerned with constructing an accelerometer. By starting from rest, the rotation sensitivity vanishes and we are left with the acceleration sensitivity. However, an accelerometer is insufficient for inertial navigation. A full sensor requires acceleration and rotation sensitivity along 3 orthogonal axes, which we refer to as a 6-axis sensor. We wish to demonstrate this principle by constructing a dual-axis sensor (acceleration and rotation) using the same techniques as our accelerometer. To include rotational sensitivity, we need to impart a large initial velocity to the atoms. However, this makes recapture problematic. With the large initial velocity, even after a short time-of-flight the ensemble is too far away from the trap to be recaptured. Another problem is that the atomic phase shift is the sum of acceleration and rotation components. To extract these terms, we require some means of decoupling them. We solve both of these problems using a technique which we call ensemble exchange [59].

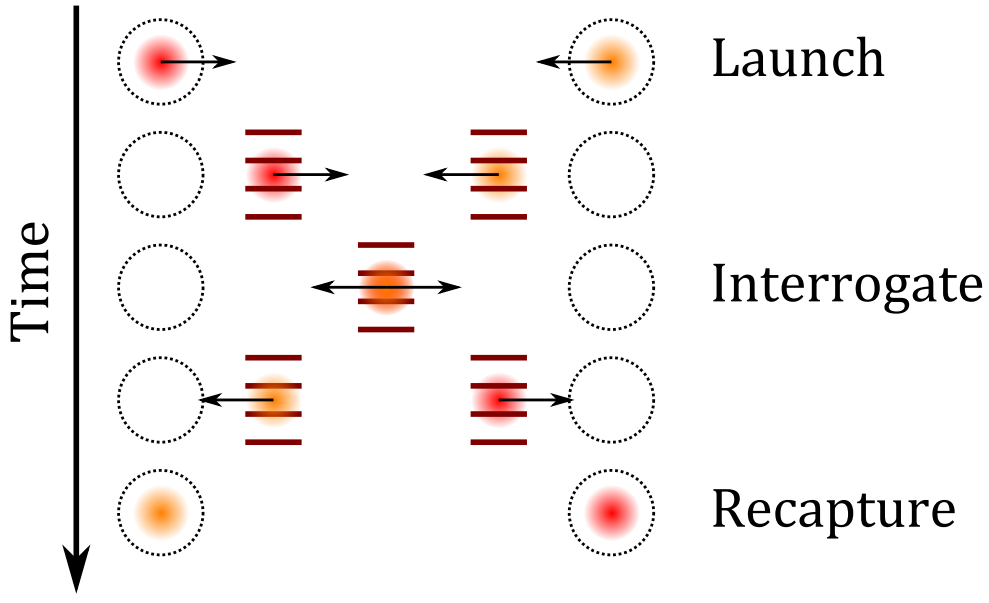

Figure 1.4: Concept behind the dual-axis high data-rate atom interferometer. We restrict the time-of-flight of the ensemble to a few milliseconds. This limits the displacement of the ensemble to less than 1 mm in inertial conditions on the order of 1 g. This enables us to recapture the ensemble in the opposite trap after the interrogation. In turn, the time required to load the ensemble for the next cycle is significantly reduced, enabling high data-rate operation.

The basic principle is that we use two ensembles separated by some distance and launch them towards each other with opposing velocities which are equal in magnitude ($\mathbf{v}_a = -\mathbf{v}_b$) [60, 10]. By operating interferometers on each ensemble, we read out phase shifts ϕ_a and ϕ_b. We may then read out the acceleration and rotation components as

$$\phi_{\text{acc}} = \mathbf{k}_{\text{eff}} \cdot \mathbf{a} T^2 \tag{1.2}$$

$$\phi_{\text{rot}} = \mathbf{k}_{\text{eff}} \cdot (-2\mathbf{v} \times \mathbf{\Omega}) T^2, \tag{1.3}$$

where $\phi_{\text{acc}} = \phi_+ = (\phi_a + \phi_b)/2$ and $\phi_{\text{rot}} = \phi_- = (\phi_a - \phi_b)/2$. This is shown in Fig. 1.3. To support a small time-of-flight, we decrease the distance between the ensembles down to a few centimeters.

The second half of this technique deals with the recapture problem. After the experiment, instead of recapturing in the same trap, we simply recapture in the *opposite* trap. Hence, the ensembles "exchanged" positions. By timing this recapture, we can ensure sufficient overlap between the ensemble and the trapping volume. Thus, our plan is to launch, interrogate, and recapture the atoms, all within a few milliseconds to minimize displacement of the ensemble. This concept is shown in Fig. 1.4.

We also seek to demonstrate a compact design. While our laser systems are still bulky free-space optics, we develop a compact sensor head with a volume on the order of a few liters. This isn't representative of the absolute size constraint of the device, but rather facilitates development while demonstrating the feasibility of a compact design.

1.4 Overview

This dissertation details work performed at Sandia National Laboratories in the domain of applied atom interferometry, with primary focus on the ensemble-exchange device. Chapter 2 details the theory behind atom interferometry and magneto-optical traps, with emphasis on application of this theory to practical systems. Chapter 3 discusses the high data-rate atom interferometer accelerometer, with results published in Applied Physics Letters ([58]). This experiment provided key insights towards the construction of the dual-axis device, presented in the next three chapters. Chapter 4 details the construction of the apparatus, laser system, and operational details. Chapter 5 characterizes the performance of the device as both an inertial sensor and a source of ultracold atom flux. Chapter 6 investigates the dynamic limits of the apparatus, as well as an enhancement of the dynamic range of the sensor by a factor of 40 through closed-loop operation. Many of these results are published in Physical Review Applied ([59]). Chapter 7 explores the novel warm vapor atom interferometer concept (in preparation [61]). Finally, Chapter 8 concludes with the prospect for

high data-rate atom interferometry.

Chapter 2

Theory

We present the theory of light-pulse atom interferometry. Beyond the fundamental principles of light-pulse atom interferometry, we also consider the effect of ensemble spatial and velocity distribution on Raman pulse efficiency. Furthermore, we present the theory of magneto-optical traps, with an emphasis on the kinematics as atoms are being captured.

2.1 Light Pulse Atom Interferometer

The light-pulse atom interferometer uses stimulated Raman transitions to coherently separate, redirect, and recombine atomic wavepackets. The Raman beams are configured in a Doppler-sensitive configuration whereby the photon recoil is on the order of that of an optical photon, which represents an increase over that of a microwave photon by 5 orders of magnitude.

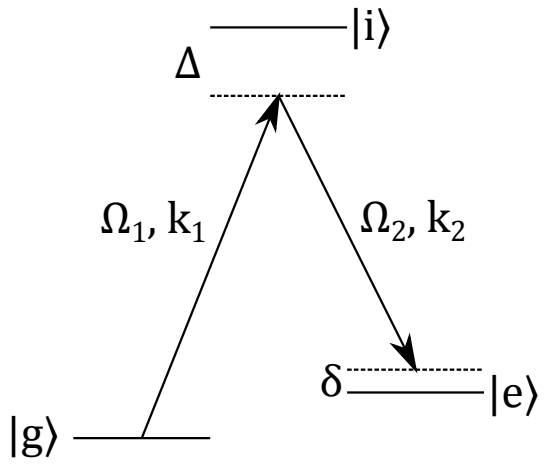

Figure 2.1: The three-level atom model. Two ground states $|g\rangle, |e\rangle$ interact via an intermediary third state $|i\rangle$. Two laser beams with Rabi frequencies Ω_1, Ω_2 and wavevectors k_1, k_2 couple each of the ground states to the interaction state. The difference in the laser frequencies is detuned from the hyperfine transition by δ, and the magnitude is detuned from the interaction state by Δ.

2.1.1 Stimulated Raman Transitions

We follow an analysis similar to [29] and consider a three level atom in a λ configuration with ground states $|g\rangle, |e\rangle$ and interaction state $|i\rangle$. We assume the energy difference between the ground and interaction state E_{gi} is much greater than that of the ground and excited state, E_{ge}. We also assume two optical fields coupling $|g\rangle$ and $|e\rangle$ to the interaction state, as shown in Fig. 2.1.

The Hamiltonian for the system is given by the sum of the atomic Hamiltonian and the interaction Hamiltonian: $\hat{H} = \hat{H}_a + \hat{H}_{\text{int}}$, where

$$\hat{H}_a = \omega_{ge} |e\rangle \langle e| + \omega_{gi} |i\rangle \langle i| \tag{2.1}$$

is the atomic Hamiltonian. The interaction Hamiltonian is $\hat{H}_{\text{int}} = -\hat{\mathbf{d}} \cdot \hat{\mathbf{E}}$, where $\hat{\mathbf{d}}$ is the electric dipole moment operator for the transition. The electric field operator

for the two optical fields is given by

$$\hat{\mathbf{E}} = \frac{1}{2}\mathbf{E}_1 e^{i(\mathbf{k}_1 \cdot x - \omega_1 t)} + \frac{1}{2}\mathbf{E}_2 e^{i(\mathbf{k}_2 \cdot x - \omega_2 t)} + c.c. \tag{2.2}$$

By the rotating wave approximation, we assume the first term couples only states $|g\rangle$ and $|i\rangle$, while the second couples $|e\rangle$ and $|i\rangle$. We thus define the Rabi frequencies as

$$\begin{aligned} \Omega_1 &= -\frac{1}{2\hbar} \langle g| \hat{\mathbf{d}} \cdot \hat{\mathbf{E}} |i\rangle \\ \Omega_2 &= -\frac{1}{2\hbar} \langle e| \hat{\mathbf{d}} \cdot \hat{\mathbf{E}} |i\rangle , \end{aligned} \tag{2.3}$$

and write the interaction Hamiltonian,

$$\hat{H}_{\text{int}} = \hbar\Omega_1^* e^{i(\mathbf{k}_1 \cdot x - \omega_1 t)} |i\rangle \langle g| + \hbar\Omega_2^* e^{i(\mathbf{k}_2 \cdot x - \omega_2 t)} |i\rangle \langle e| + c.c., \tag{2.4}$$

where we assume Δ is sufficiently large to neglect spontaneous emission. For now we will ignore the momentum component. We will revisit it later. The equations of motion are then,

$$\begin{aligned} i\hbar\dot{c}_g &= \hbar\Omega_1 e^{-i\omega_1 t} c_i \\ i\hbar\dot{c}_e &= \hbar\Omega_2 e^{-i\omega_2 t} c_i + \hbar\omega_{ge} c_e \\ i\hbar\dot{c}_i &= \hbar\Omega_1^* e^{i\omega_1 t} c_g + \hbar\Omega_2^* e^{i\omega_2 t} c_e + \hbar\omega_{gi} c_i. \end{aligned} \tag{2.5}$$

We now make the substitution

$$\begin{aligned} c_g &= \tilde{c}_g \\ c_e &= \tilde{c}_e e^{i\omega_{ge} t} \\ c_i &= \tilde{c}_i e^{i\omega_{gi} t}, \end{aligned} \tag{2.6}$$

and Eq. 2.5 becomes

$$\begin{aligned} i\dot{\tilde{c}}_g &= \Omega_1 e^{-i(\omega_{gi}-\omega_1)t}\tilde{c}_i \\ i\dot{\tilde{c}}_e &= \Omega_2 e^{-i(\omega_{gi}-\omega_{ge}-\omega_2)t}\tilde{c}_i + \omega_{ge}\tilde{c}_e \\ i\dot{\tilde{c}}_i &= \Omega_1^* e^{i(\omega_1-\omega_{gi})t}\tilde{c}_g + \Omega_2^* e^{i(\omega_2-\omega_{gi}+\omega ge)t}\tilde{c}_e + \omega_{gi}\tilde{c}_i. \end{aligned} \tag{2.7}$$

We now define the single and two-photon detunings as $\Delta = \omega_{gi} - \omega_1$ and $\delta = (\omega_1 - \omega_2) - \omega_{ge}$, as shown in Fig. 2.1. Writing Eq. 2.7 in terms of these, we have

$$\begin{aligned} \dot{\tilde{c}}_g &= -i\Omega_1 e^{-i\Delta t}\tilde{c}_i \\ \dot{\tilde{c}}_e &= -i\Omega_2 e^{-i(\Delta+\delta)t}\tilde{c}_i \\ \dot{\tilde{c}}_i &= -i\Omega_1^* e^{i\Delta t}\tilde{c}_g - i\Omega_2^* e^{i(\Delta+\delta)t}\tilde{c}_e. \end{aligned} \tag{2.8}$$

We now assume that $\Delta \gg \Omega_1, \Omega_2, \delta$. In an approximation known as adiabatic elimination, we note that the terms $\dot{\tilde{c}}_g$ and $\dot{\tilde{c}}_e$ oscillate much more slowly than $\dot{\tilde{c}}_i$. We thus integrate this last expression assuming constant values for $\tilde{c}_g$ and $\tilde{c}_e$. We then have,

$$\tilde{c}_i = -\frac{\Omega_1^*}{\Delta}e^{i\Delta t}\tilde{c}_g - \frac{\Omega_2^*}{\Delta+\delta}e^{i(\Delta+\delta)t}\tilde{c}_e. \tag{2.9}$$

Substituting this equation into the ground and excited state equations in Eq. 2.8, we find

$$\dot{\tilde{c}}_g = i\frac{|\Omega_1|^2}{\Delta}\tilde{c}_g + i\frac{\Omega_1\Omega_2^*}{\Delta}e^{i\delta t}\tilde{c}_e, \tag{2.10}$$

$$\dot{\tilde{c}}_e = i\frac{\Omega_1^*\Omega_2}{\Delta}e^{-i\delta t}\tilde{c}_g + i\frac{|\Omega_2|^2}{\Delta}\tilde{c}_e, \tag{2.11}$$

where we ignored the higher order terms in the expansion of $\Omega^2/(\Delta+\delta)$. We find the dynamics thus reduce to that of a two-level system, with the two-photon Rabi

frequency $\Omega_{\text{eff}} = 2\Omega_1\Omega_2/\Delta$ and detuning δ. The solution is then given by,

$$\begin{aligned} |c_g(t)|^2 &= \frac{\Omega_{\text{eff}}^2}{\Omega_{\text{eff}}^2 + \delta^2} \sin^2\left(\frac{\sqrt{\Omega_{\text{eff}}^2 + \delta^2}\, t}{2}\right) \\ |c_e(t)|^2 &= \frac{\delta^2}{\Omega_{\text{eff}}^2 + \delta^2} + \frac{\Omega_{\text{eff}}^2}{\Omega_{\text{eff}}^2 + \delta^2} \cos^2\left(\frac{\sqrt{\Omega_{\text{eff}}^2 + \delta^2}\, t}{2}\right). \end{aligned} \tag{2.12}$$

The atomic population thus undergoes coherent Rabi oscillations between the ground and excited state at the generalized two-photon Rabi frequency $\tilde{\Omega}_{\text{eff}} = \sqrt{\Omega_{\text{eff}}^2 + \delta^2}$. A pulse of duration $t = \pi/\tilde{\Omega}_{\text{eff}}$ (known as a "π pulse") inverts the atomic population. Similarly, a pulse of duration $t = (\pi/2)/\tilde{\Omega}_{\text{eff}}$ (known as a "$\pi/2$ pulse") generates an equal superposition between ground and excited states. The atom interferometer is constructed from a sequence of such pulses.

2.1.2 Atom Interferometer

We construct the atom interferometer using a $\pi/2-\pi-\pi/2$ pulse sequence of Doppler-sensitive Raman transitions. In the Doppler-sensitive configuration, the laser beams are counter-propagating, each containing one of the two frequencies needed for the transition. The atom absorbs a photon from one laser and receives a momentum recoil of $+\hbar\mathbf{k}$. The excited atom then undergoes stimulated emission into the other laser, and receives a momentum recoil of approximately $-(-\hbar\mathbf{k})$. There exists a small difference due to the hyperfine frequency. The total momentum recoil is thus approximately $2\hbar\mathbf{k} = \hbar\mathbf{k}_{\text{eff}}$. The important thing to note here is that the total momentum recoil is that of an optical photon, which is orders of magnitude larger than the momentum recoil of a microwave photon. Secondly, the momentum recoil has a very precise magnitude, limited in principle by the frequency stability of the Raman laser. Typical experiments readily achieve a fractional stability of 10^{-8} in this respect. However, there are additional sources of error stemming from the direction

of the wavevector which must be considered, such as the wavefront of a Gaussian beam.

The atom interferometer utilizes this large, precise momentum transfer to coherently separate, redirect, and recombine atomic wave packets. Assume the initial state of the atom is given by $|\psi_0\rangle = |g, \mathbf{p}_0\rangle$, where $|\mathbf{p}_0\rangle$ is the initial momentum state of the atom. The first pulse ($\pi/2$) generates a coherent superposition state,

$$|\psi_1\rangle = \frac{1}{\sqrt{2}}\left(|g, \mathbf{p}_0\rangle + e^{i\phi_1}\,|e, \mathbf{p}_0 + \hbar\mathbf{k}_{\text{eff}}\rangle\right), \tag{2.13}$$

where $\phi_n = \mathbf{k}_{\text{eff}} \cdot \mathbf{x}_n - \omega t_n$ is the phase of the light field during the nth pulse. The internal state of the atom becomes entangled with its external momentum state. For some interrogation time T_1, the atomic wavepackets separate beyond several times its de Broglie wavelength. The second pulse (π) reverses the momentum state so that

$$|\psi_2\rangle = \frac{1}{\sqrt{2}}\left(e^{i\phi_2}\,|e, \mathbf{p}_0 + \hbar\mathbf{k}_{\text{eff}}\rangle + e^{i(\phi_1-\phi_2)}\,|g, \mathbf{p}_0\rangle\right), \tag{2.14}$$

thus redirecting the wavepackets. After a time T_2, the final pulse ($\pi/2$) recombines the wavepackets, so that

$$|\psi_3\rangle = \frac{1}{\sqrt{2}}\left(e^{i(\phi_2-\phi_3)}\,|g, \mathbf{p}_0\rangle + e^{i(\phi_1-\phi_2)}\,|e, \mathbf{p}_0\rangle\right). \tag{2.15}$$

The relative phase between the states is given by $\Delta\phi = (\phi_1 - \phi_2) - (\phi_2 - \phi_3) = \phi_1 - 2\phi_2 + \phi_3$. If we assume $T_1 = T_2 = T$, the frequency component of the phase drops out and we are left with

$$\begin{aligned} \Delta\phi &= \mathbf{k}_{\text{eff}} \cdot (\mathbf{x}_1 - 2\mathbf{x}_2 + \mathbf{x}_3) \\ &= \mathbf{k}_{\text{eff}} \cdot \left(\frac{\mathbf{x}_1 - 2\mathbf{x}_2 + \mathbf{x}_3}{T^2}\right) T^2, \end{aligned} \tag{2.16}$$

where we multiplied and divided by T^2. We note that the factor $(\mathbf{x}_1 - 2\mathbf{x}_2 + \mathbf{x}_3)/T^2$ represents the finite difference formula for curvature, which we deconstruct into ac-

celeration and rotation components as

$$\frac{\mathbf{x}_1 - 2\mathbf{x}_2 + \mathbf{x}_3}{T^2} \approx \ddot{\mathbf{x}} = \mathbf{a} - 2\mathbf{v} \times \mathbf{\Omega}, \tag{2.17}$$

where $\mathbf{v}$ is the initial velocity of the atoms, and $\mathbf{a}$ and $\mathbf{\Omega}$ are the acceleration and rotation, respectively. Note that these inertial quantities are measured with respect to the laser, which we refer to as the "platform". Thus, these inertial quantities are encoded in the total phase shift as,

$$\Delta\phi = \mathbf{k}_{\text{eff}} \cdot (\mathbf{a} - 2\mathbf{v} \times \mathbf{\Omega})T^2. \tag{2.18}$$

2.1.3 Inhomogeneous Rabi Flopping

In practice given an ensemble of atoms, we usually do not have each atom experience the same Rabi frequency and detuning. A Gaussian laser beam results in a spatial distribution of Rabi frequencies. The Doppler-shift gives rise to a velocity-dependent detuning. Typically we use large beams with high intensity (large transform-width) to mitigate this effect. However, there is only a limited amount of power available. Thus, it is important to make optimal use of the power available. We wish to model Rabi flopping under these conditions. The probability of state transfer from Eq. 2.12 is given by,

$$P(t, \Omega, \delta) = \frac{\Omega^2}{\Omega^2 + \delta^2} \sin^2\left(\frac{\sqrt{\Omega^2 + \delta^2}\ t}{2}\right). \tag{2.19}$$

Assuming the interrogation laser travels along $\mathbf{k}_{\text{eff}} = k_{\text{eff}}\hat{\mathbf{z}}$, Ω and δ are given by,

$$\Omega(x, y) = \Omega_{\text{eff}} \exp\left(-\frac{x^2 + y^2}{2(\sigma_{x,\text{laser}})^2}\right) \tag{2.20}$$

$$\delta(v_z) = k_{\text{eff}} v_z, \tag{2.21}$$

where $\sigma_{x,\text{laser}}$ is the spatial extent of the Raman beam (half the beam waist). For the ensemble, we assume a Gaussian spatial distribution and a Maxwell-Boltzmann

velocity distribution. These are given by,

$$g_x(x,y,z) = \frac{1}{(2\pi)^{3/2}(\sigma_{x,\text{ensemble}})^3}\exp\left(-\frac{x^2+y^2+z^2}{2(\sigma_{x,\text{ensemble}})^2}\right) \tag{2.22}$$

$$g_v(v_x,v_y,v_z) = \frac{1}{(2\pi)^{3/2}(\sigma_v)^3}\exp\left(-\frac{v_x^2+v_y^2+v_z^2}{2(\sigma_v)^2}\right), \tag{2.23}$$

where $\sigma_{x,\text{ensemble}}$ is the spatial extent of the ensemble, and $\sigma_v = \sqrt{k\mathcal{T}/m}$. We find the ensemble average Rabi flopping by integrating over these distributions,

$$P_{\text{avg}}(t) = \int_{-\infty}^{\infty}\int_{-\infty}^{\infty} P(t,\Omega(x,y),\delta(v_z))\; g_x(x,y,z)\; g_v(v_x,v_y,v_z)\; \mathrm{d}^3x\; \mathrm{d}^3v. \tag{2.24}$$

We note that the integrals over z, v_x, v_y average to 1. We numerically evaluate this integral as a function of t, the ratio of the ensemble size to Raman beam size $r_x = \sigma_{x,\text{ensemble}}/\sigma_{x,\text{laser}}$, and the ratio of the Doppler width to the transition width $r_\delta = k_{\text{eff}}\sigma_v/(\Omega_{\text{eff}}/2)$. First, we plot the Rabi flopping for various values of r_x and r_δ from 0 to 2 in Fig. 2.2. We note here that the population transfer efficiency drops to 50% around $r_x = 1, r_\delta = 1$. Also the π pulse lengths increase for larger r_x and decrease for larger r_δ. This is expected since for larger r_x, we are averaging atoms that see slower Rabi frequencies. For larger r_δ, the Rabi flopping occurs at the generalized Rabi frequency $\tilde{\Omega}_{\text{eff}} = \sqrt{\Omega_{\text{eff}}^2+\delta^2}$, and is thus faster for higher detuning.

Now, we consider the maximum population transfer efficiency, $\mathcal{E}$ as a function of r_x and r_δ. This was numerically calculated by finding the maximum transfer probability at each point (r_x, r_δ) from 0 to 2. A plot of this function is shown in Fig. 2.3. As expected, the pulse efficiency is maximal with small r_x and r_δ and falls off when they approach unity. We find we may estimate the efficiency in this range with

$$\mathcal{E}(r_x,r_\delta) \approx \exp\left(-\frac{r_x^2}{2\sigma_x^2}-\frac{r_\delta^2}{2\sigma_\delta^2}\right), \tag{2.25}$$

where we numerically fit and find $\sigma_x = 1.3$ and $\sigma_\delta = 1.7$. The rms error over this range is 3%.

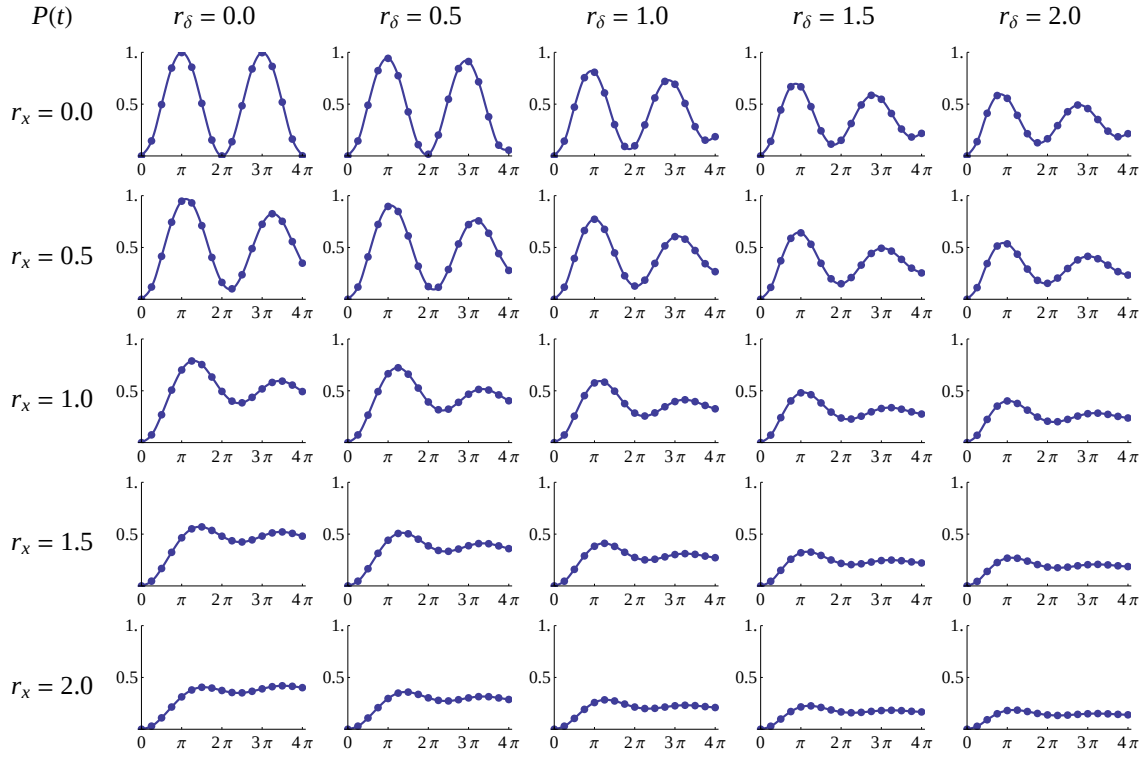

Figure 2.2: Rabi flopping under an inhomogeneous Rabi frequency and detuning. The parameters r_δ and r_x represent the ratio of ensemble detuning (via the Doppler-shift) and spatial distribution with respect to the transition with and Raman beam waist. We observe significant loss of atomic coherence when either of these ratios is 1 or greater.

We now assume a fixed ensemble size and temperature, as well as a finite amount of power for the Raman laser. We leave the beam waist of the laser ω as a free parameter. Clearly $r_x \propto 1/\omega$ by definition. The peak intensity scales as $I \propto 1/\omega^2$. The single-photon Rabi frequencies scale as $\Omega_{1,2} \propto \sqrt{I}$, so that the two-photon Rabi frequency scales as $\Omega_{\text{eff}} \propto I$. Thus, we have $r_\delta \propto \omega^2$. With these relationships and data from Fig. 2.3, we may optimize the size of our Raman beams given a known ensemble size and temperature.

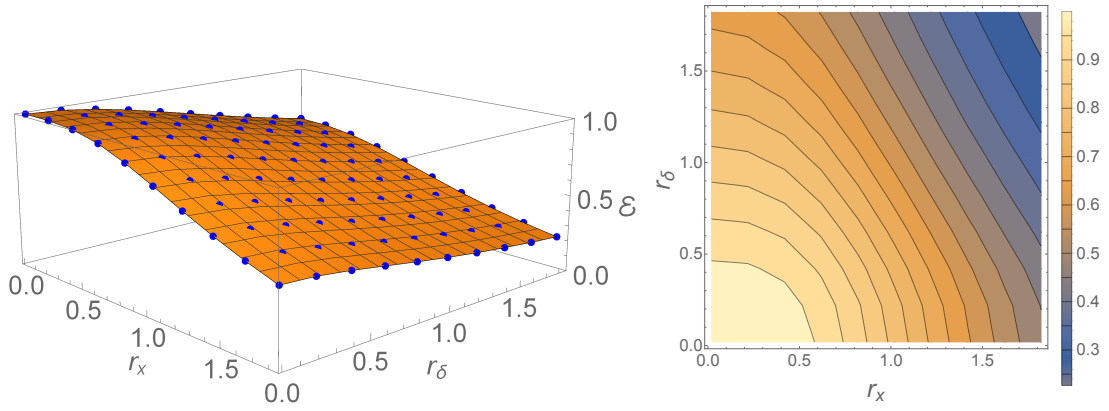

Figure 2.3: Raman pulse efficiency as a function of r_x and r_δ. We find the pulse efficiency decreases similarly with respect to each of these parameters. Left: Data calculated by numerically integrating Eq. 2.24. The surface is a guide for the eye. Right: Contour plot of the same data. We find the pulse efficiency decreases to 50% in approximately a circle defined by $r_x^2 + r_\delta^2 = 1$. This presents a useful metric for evaluating our experimental pulse efficiency.

2.2 Magneto-Optical Trap

The Magneto-Optical Trap (MOT) uses principles of laser cooling to produce a cold sample of neutral atoms. Since the first demonstration [30], it has become the workhorse of modern cold atom physics. The relatively simple design enables the MOT to serve as the starting point for many experiments. For our purposes, simplicity is necessary to facilitate miniaturization of the sensor. Furthermore, for our particular application it is imperative to understand the dynamics of MOTs, so that we may understand their response to inertial motion. While many experiments use the MOT simply as a source of some number of cold atoms before proceeding to the physics, in a sense the MOT *is* the physics for our experiment. Thus, we present the theory of the magneto-optical trap with an emphasis on the dynamics as atoms relax into the trap.

The MOT consists of a set of lasers which provide the dissipative cooling force and a set of magnetic field coils which in combination with the lasers forms a trapping

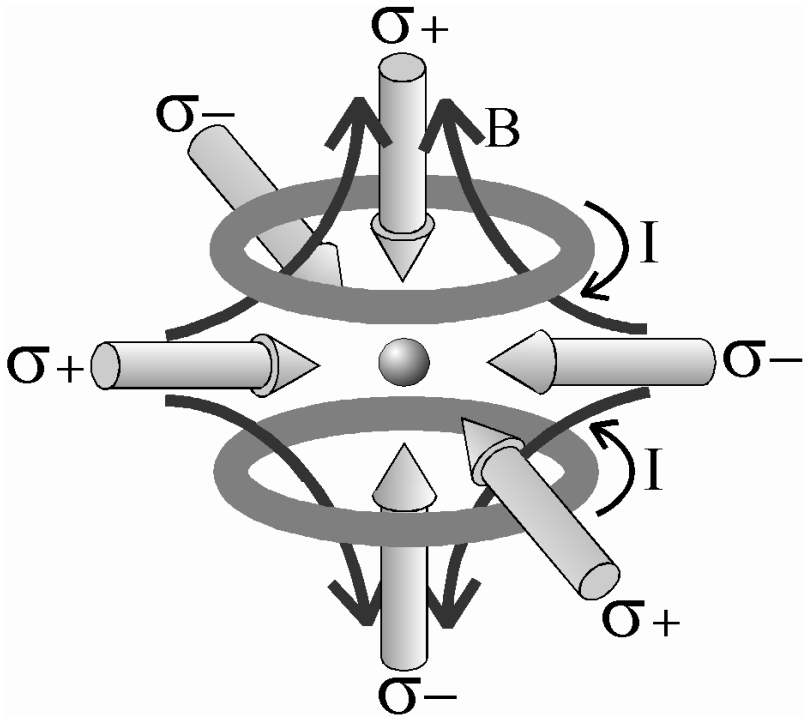

Figure 2.4: A diagram depicting the laser and magnetic coil configuration in a typical MOT. Six cooling lasers form optical molasses in three dimensions. The magnetic field generated by a pair of anti-Helmholtz coils, in conjunction with laser polarization, provides a three dimensional harmonic trapping force.

force. A diagram depicting the coil and laser configuration is shown in Fig. 2.4. Typically alkali metals are used due to the relatively simplicity of the atomic energy levels. We will consider the interaction of a two level atom with a near-resonant laser. This interaction is described by the optical Bloch equations [62, 63]. From this, we calculate the photon scattering rate,

$$\gamma = \left(\frac{\Gamma}{2}\right) \frac{s_0}{1 + s_0 + (2\Delta/\Gamma)^2}, \tag{2.26}$$

where Γ is the excited state lifetime, $s_0 = I/I_{\text{sat}}$ is the saturation parameter, I_{sat} is the saturation intensity of the transition, I is the intensity of the laser, and Δ is the detuning. Now we consider the scattering rates from a pair of counter-propagating lasers detuned by $-\delta_{\text{laser}}$. As the atoms move towards one of the lasers, the Doppler effect shifts the frequency of that laser closer to resonance by $\delta_{\text{doppler}} = \mathbf{k}\cdot\mathbf{v}$, increasing

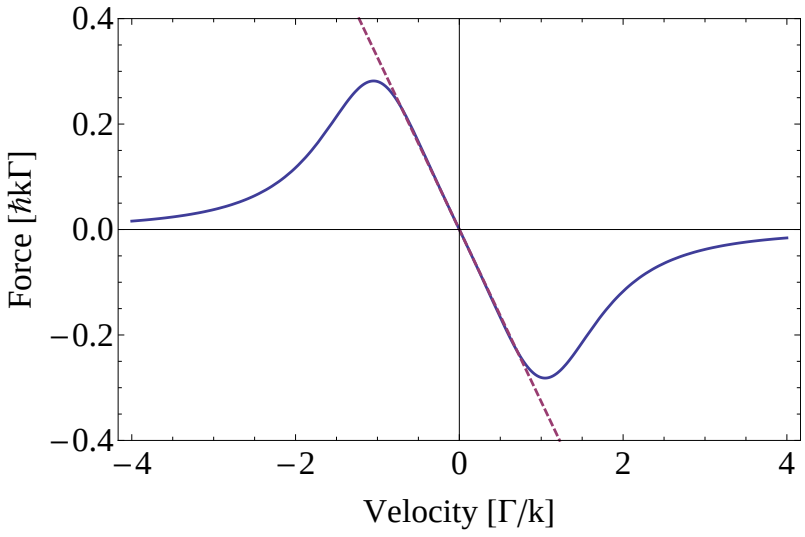

Figure 2.5: MOT cooling force in one dimension. The force is linear when the magnitude of the velocity is less than the capture velocity, given by $v_c = \Gamma/k$.

the photon scattering rate. Thus, the photon scattering rate increases in the direction opposite to the velocity, producing a damping force over a large number of photon recoils [64]. Three such pairs of such lasers oriented orthogonally provide a damping force in all directions, known as optical molasses [65]. We take $s_0 = 2, \delta_{\text{laser}} = \Gamma/2$ and plot this damping force in Fig. 2.5. We note that all velocity classes feel some damping force in the "colder" direction, even for $\mathbf{k} \cdot \mathbf{v} \gg \Gamma$. However, it is useful to define a capture velocity $v_c = \Gamma/k$ within which the force is approximately linear. Expanding the force in the linear regime gives us,

$$\mathbf{F}_{\text{cooling}} \approx -\frac{8 s_0 \delta \hbar k^2}{\Gamma(1 + s_0 + (2\delta/\Gamma)^2)^2}\mathbf{v}, \quad v < v_c. \tag{2.27}$$

Theoretically this damping force should cool to zero velocity. However, this nearly continuous force is the result of many discrete photon scatters. We can thus treat these photon scatters as generating a random walk of momentum with step size $\Delta p = \hbar k$ and frequency $1/\Delta t = 2\gamma$ [63]. This corresponds with a diffusion coefficient $D_0 = 2(\Delta p)^2/\Delta t = 4\gamma(\hbar k)^2$. From Brownian motion theory, we may calculate the temperature in steady-state as $k_B \mathcal{T}_D = D_0/\beta$. This is the Doppler temperature

given by $k_B\mathcal{T}_D = \hbar\gamma/2$. There are many independent derivations of this parameter. Interestingly, this parameter is independent of wavelength, mass, and intensity [63]. In practice, due to sub-Doppler processes the ensemble temperature is well below this level.

We now note that real atoms are not two-level atoms. Fortunately, alkali metals have what are known as cycling transitions, which allow us to make this approximation. In the D_2, $n^2S_{1/2} \rightarrow n^2P_{3/2}$ manifold, the transition $\left|F = I + \frac{1}{2}, m_F = \pm(I + \frac{1}{2})\right\rangle \rightarrow \left|F' = I + \frac{3}{2}, m'_F = \pm(I + \frac{3}{2})\right\rangle$ forms a closed system under appropriate light polarization. In practice however, off resonant scatter leaks population out of this system. Thus, typically a repumping laser is used to cycle atoms out of the $\left|F = I - \frac{1}{2}\right\rangle$ manifold and back into $\left|F = I + \frac{1}{2}\right\rangle$.

Thus far, we have described the damping force of the MOT. The spatially-dependent potential utilizes the Zeeman effect, where magnetic sublevels of an atomic state shift by an amount proportional to the applied magnetic field. This results in a frequency shift given by $\delta_{\text{Zeeman}} = \mu' B/\hbar$, where μ' is the effective magnetic moment for the transition used. In the case of the cycling transition described above, $\mu' = \mu_B$. The total detuning is then given by

$$\begin{aligned} \Delta &= -\delta_{\text{laser}} + \delta_{\text{Doppler}} + \delta_{\text{Zeeman}} \\ &= -\delta_{\text{laser}} + \mathbf{k}\cdot\mathbf{v} + \mu'\mathbf{B}(\mathbf{x})\cdot\hat{\mathbf{p}}/\hbar, \end{aligned} \tag{2.28}$$

where $\hat{\mathbf{p}}$ is the polarization vector of the light field. If we assume a linear magnetic field, the atomic transition experiences an energy shift proportional to the distance from the trap center. Then similar to the Doppler shift $\mathbf{k}\cdot\mathbf{v}$, the atom experiences a trapping force from the Zeeman shift $\mu'\mathbf{A}\cdot\mathbf{x}/\hbar$, where $A = \nabla|B|$ is the magnetic field gradient. Following this analogy, we find the capture distance to be $x_c = \Gamma\hbar/(\mu' A)$ and the capture volume V_c as the sphere which corresponds to this distance. The potential which corresponds to this force is shown in Fig. 2.6. Making a similar

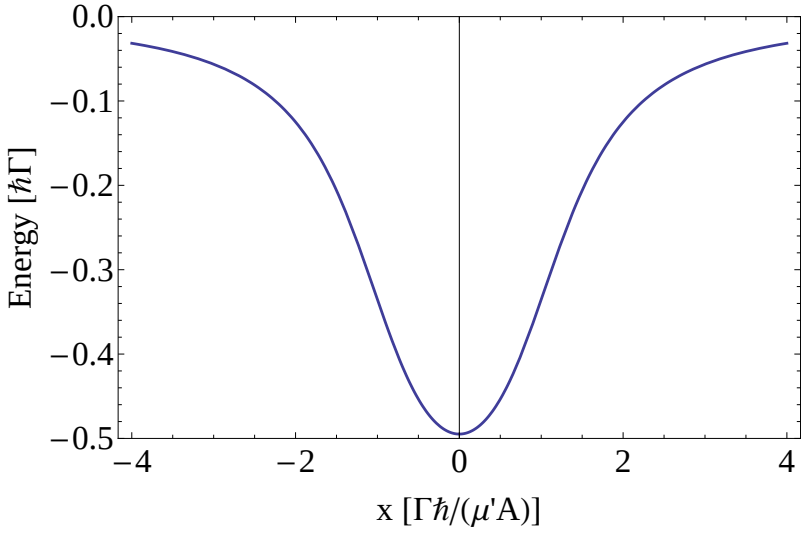

Figure 2.6: MOT trapping potential in one dimension. The length-scale of the trap is determined by the capture distance $x_c = \Gamma\hbar/(\mu' A)$.

approximation as 2.27, we find the trapping force

$$\mathbf{F}_{\text{trapping}} \approx -\frac{8 s_0 \delta \mu' A k}{\Gamma(1 + s_0 + (2\delta/\Gamma)^2)^2}\mathbf{x}, \quad x < x_c. \tag{2.29}$$

We may thus write the total force as,

$$\begin{aligned} \mathbf{F} &= \mathbf{F}_{\text{cooling}} + \mathbf{F}_{\text{trapping}} \\ &\approx -\beta \mathbf{v} - \kappa \mathbf{x}, \end{aligned} \tag{2.30}$$

where β and κ are read directly from 2.27 and 2.29. This equation represents a damped harmonic oscillator, with spring constant κ and damping coefficient β. The oscillation frequency is thus $\omega_{\text{MOT}} = \sqrt{\kappa/m}$, where m is the mass of the atom. The damping ratio is given by $\zeta_{MOT} = \beta/(2\sqrt{m\kappa})$. Substituting in values for ^{87}Rb and assuming a typical 10 G/cm field gradient, we find $\omega_{MOT} \approx 2\pi \times 1$ kHz and $\zeta_{MOT} \approx 2$. Thus, the motion is overdamped with a characteristic restoring time of $\tau_{MOT} \approx 2$ ms.

In practice, we use a pair of quadrupole magnetic field coils which create a zero of the magnetic field and a linear gradient in all directions. The closed form solution

for the magnetic field from a pair of coils of radius a, separated from the origin by a distance b with current I is given by (in cylindrical coordinates) [66] ,

$$\begin{aligned}
\mathbf{B} &= B_r\hat{\mathbf{r}} + B_z\hat{\mathbf{z}} \\
B_r &= \frac{I\mu_0}{2a}\frac{\gamma_1}{\pi\sqrt{Q_1}}\left(E(k_1)\frac{1+\alpha^2+\beta_1^2}{Q_1-4\alpha} - K(k_1)\right) \\
&\quad -\frac{I\mu_0}{2a}\frac{\gamma_2}{\pi\sqrt{Q_2}}\left(E(k_2)\frac{1+\alpha^2+\beta_2^2}{Q_2-4\alpha} - K(k_2)\right) \\
B_z &= \frac{I\mu_0}{2a}\frac{1}{\pi\sqrt{Q_1}}\left(E(k_1)\frac{1-\alpha^2-\beta_1^2}{Q_1-4\alpha} + K(k_1)\right) \\
&\quad -\frac{I\mu_0}{2a}\frac{1}{\pi\sqrt{Q_2}}\left(E(k_2)\frac{1-\alpha^2-\beta_2^2}{Q_2-4\alpha} + K(k_2)\right),
\end{aligned} \tag{2.31}$$

where $\alpha = r/a$, $\beta_1 = (b-x)/a$, $\beta_2 = (-b-x)/a$, $\gamma_i = \beta_i/\alpha$, $Q_i = (1+\alpha)^2 + \beta_i^2$, $k_i = \sqrt{4\alpha/Q_i}$, and $K(k)$ and $E(k)$ are the complete elliptic integral functions of the first and second kind, respectively. To first order, we may approximate this near the origin as,

$$\mathbf{B} \approx -\frac{1}{2}\frac{\mathrm{d}B}{\mathrm{d}z}r\hat{\mathbf{r}} + \frac{\mathrm{d}B}{\mathrm{d}z}z\hat{\mathbf{z}}, \tag{2.32}$$

where we refer to $A = \mathrm{d}B/\mathrm{d}z$ as the axial field gradient and $\mathrm{d}B/\mathrm{d}r = -(1/2)A$ as the radial field gradient. This approximation is valid assuming $r \ll a$ and $z \ll b$. We presented the full analytic solution so that we may consider the effect of small magnetic field coils where these assumptions may not necessarily be valid. Given the parameters above, we have $A = 3\mu_0 I a b^2/(a^2+b^2)^{5/2}$ [67]. For a review of coil design including inductance and thermal management, see reference [68].

There were many assumptions made here in this derivation of MOT dynamics. First off, that the saturation parameter is constant in space. In reality, the saturation parameter follows the Gaussian intensity profile of the laser beams. Secondly, we were largely concerned with the dynamics within the capture velocity and capture volume. As stated previously, being outside of this regime doesn't necessarily preclude the possibility of falling into the trap. Finally, the model does not take into account

beam alignment, polarization purity, and practical magnetic field geometry. These factors are particularly important when discussing recapture, which depends heavily on the atoms' kinematics as they fall into the trap. As such, we have developed a simulation which takes all of these factors into account. Details of the simulation are shown in Appendix B. Application of the simulation to the recapture problem is the subject of future work.

2.2.1 Recapture

The well-known MOT loading equation [69] describes the number of atoms in the MOT as a function of time. The model assumes a constant loading rate of atoms from vapor with a loss rate dominated by background collisions in proportion to the number of atoms in the trap. This background limited lifetime is typically on the order of $1 - 60$ s depending on the quality of the vacuum. We extend this equation by including recapture between discrete shots of the experiment. We model the atom number of each shot n as a constant recapture fraction r_0, with a loss rate β and linear loading rate α. Furthermore, we assume a cycle time T_c, and a fraction of the cycle η reserved for recapture. The atom number may then be modeled as the sequential sum of atoms loaded from vapor, atoms recaptured, and atoms lost of background collisions. If we assume no density-induced losses, the atom number is given by the geometric sequence,

$$N_{n+1} = \alpha\eta T_c + (r_0 - \beta T_c)N_n, \tag{2.33}$$

with solution,

$$N_n = \frac{\alpha\eta T_c}{1-r}(1 - r^n), \tag{2.34}$$

where $r = r_0 - \beta T_c$ is the net recapture efficiency. This assumes that the recapture time ηT_c is sufficiently larger than the MOT relaxation time, in order to recapture most of the available atoms. When the number of atoms which were not recaptured

equals the number of atoms loaded from vapor, we achieve a steady-state atom number N_s, given by

$$N_s = \lim_{n\to\infty} N_n = \frac{\alpha\eta T_c}{1-r} = \frac{\alpha\eta T_c}{\beta T_c + (1-r_0)}. \tag{2.35}$$

For $r_0 < 1$ under low vapor pressure ($\beta T_c \ll 1 - r_0$), the loss rate is dominated by imperfect recapture. Thus, the steady-state atom number $N_s = \alpha\eta T_c/(1-r_0)$ grows linearly in α. Under higher vapor pressure ($\beta T_c \gg 1 - r_0$), the loss rate is dominated by background vapor collisions, resulting in steady state atom number $N_s = \eta\alpha/\beta$. Assuming constant trap parameters, α and β are both proportional to vapor pressure. Therefore, similar to canonical MOT loading, the ratio α/β and thus the total atom number are constant. By simulating MOT loading from background, with $r_0 = 1, \eta = 1$, and in the limit of small T_c, N_n becomes the usual MOT loading equation,

$$N(t) = \frac{\alpha}{\beta}(1 - e^{-\beta t}), \tag{2.36}$$

thus demonstrating correct behavior of the model in the appropriate limits.

We will use these equations to obtain an accurate calculation of the MOT recapture efficiency. In particular, Eq. 2.34 provides a method by which we can measure the recapture efficiency independent of the total atom number. By turning on the trap and fitting this expression as a function of n, we may extract the recapture efficiency independently of the total atom number, the scale factor of which generally contains large uncertainties.

Chapter 3

High Data-Rate Accelerometer

In this chapter, we present a high data-rate atom interferometer accelerometer. While the device functions as a stand-alone accelerometer, it also served as a prototype experiment for the dual-axis sensor. The experimental apparatus was designed to illustrate many of the principles which will be employed in the dual-axis sensor, including small MOT beams, small quadrupole coils, recapture, and high data-rate. We intentionally omit may of the details concerning laser system design and construction as the system is similar to the final version, presented in the next chapter.

The experiment itself is fairly straightforward. We prepare an ensemble of cold atoms in a MOT. The trap is released, and the atoms fall ballistically for a few milliseconds. We perform the Raman interrogation, and readout the atomic state. From the atomic population in each of the hyperfine states, we may extract the inertial information. After the experiment, the atoms are still well within the capture volume of the MOT. We reactivate the trap, recapturing most of the ensemble. After the ensemble relaxes back to the center of the trap and atoms are loaded from vapor, the cycle begins anew.

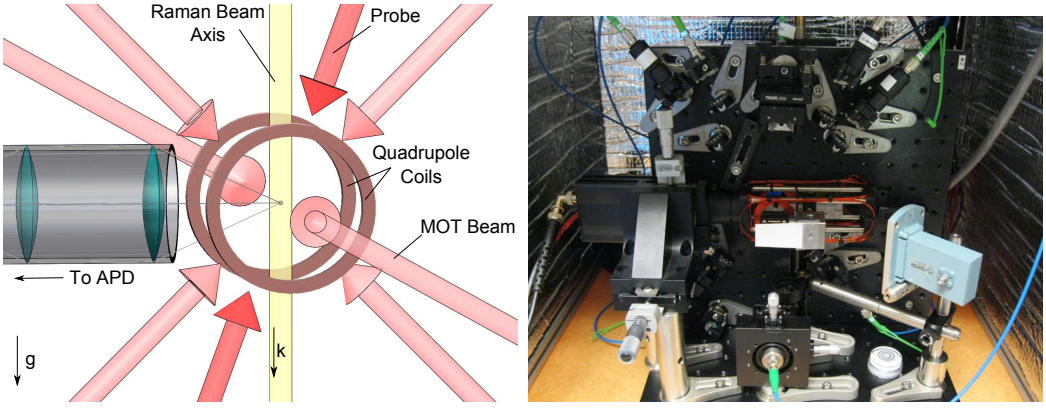

Figure 3.1: A diagram and picture of the high data-rate accelerometer apparatus. Left: The arrangement of laser beams for the experiment. The Raman beam axis is oriented to coincide approximately with the direction of gravity. Right: We build the optomechanical frame using free-space optical components mounted around a T-shaped vacuum cell. We employ compact trapping and bias magnetic coils to investigate the feasibility of a compact arrangement. Figure reprinted from [58].

3.1 Experiment

The experimental apparatus is shown in Fig. 3.1. It consists of a magneto-optical trap of ^{87}Rb with cooling light, repump light, quadrupole coils, and bias coils. The vacuum cell is a quartz cell of dimensions $14 \times 16 \times 80$ mm^3 at a vapor pressure of 2×10^{-9} torr. The source for the atoms is a getter driven at 3.6 A. Additionally, the experiment has a probe laser, a pump laser, the two Raman lasers, and an avalanche photodiode. The cooling laser provides a total of 70 mW of power locked 9 MHz red of the $|F = 2\rangle \rightarrow |F = 3'\rangle$ D2 transition in ^{87}Rb. The light is split into three beams collimated to a $1/e^2$ diameter of 5.2 mm and retro-reflected. The repump laser consists of 1 mW of light resonant with the $|F = 1\rangle \rightarrow |F = 2'\rangle$ transition to prevent accumulation in the dark state. The trapping field is generated from a pair of quadrupole coils of diameter 32 mm. The corresponding axial field gradient is 7.8 G/cm. The resulting loading rate of atoms into the MOT is 4×10^4 atoms/ms.

The experiment proceeds as follows. At the start of the experiment, the MOT

atoms are sub-Doppler cooled to 5.5 μK. The atoms are then pumped into the $|F = 1\rangle$ manifold with a 100 μs depump pulse resonant with the $|F = 2\rangle \rightarrow |F = 2'\rangle$ D2 transition. This was chosen over the more traditional D1 transition (which limits the off-resonant scatter) due to a simplified laser system whereby an AOM simply downshifts the master laser to this transition. Furthermore, this depump pulse is performed without any repumping light, enabling the entire $|F = 1\rangle$ manifold to be populated. This simplified optical pumping scheme reduces the number of atoms available in the clock transition to approximately 43% of the available atoms. However, we find that this pumping scheme greatly simplifies the apparatus by making the D2 off-resonant scatter negligible and maintaining the cold ensemble temperature. Furthermore, while the atoms remaining in the $m = \pm 1$ sublevels contribute a small amount of background noise, they are easily recaptured allowing for shorter recapture time, thus enabling a faster data-rate. After pumping, the atoms are interrogated with the Raman beams.

The Raman master laser consists of a home-built external cavity diode laser (ECDL) locked 1.2 GHz red of the $|F = 2\rangle \rightarrow |F = 3'\rangle$ transition. The two phase-coherent fields are generated by injection locking two laser diodes to the zero and first order sideband of an electro-optic modulator (EOM) driven at the hyperfine frequency, $\nu_{\mathrm{hf}} \approx 6.8$ GHz. These beams are coupled into orthogonal axes of the same polarization maintaining fiber, where they are once again separated at the experiment and redirected so that one of the frequencies travels upwards and the other downwards. The beams are collimated to a $1/e^2$ diameter of 5.5 mm, corresponding to a Rabi frequency of $\Omega_{\mathrm{eff}} = 2\pi \times 161$ kHz.

This method adds additional phase noise from the optical path length when compared with other methods which use a common path for both beams [56]. These methods involve the atoms falling ballistically under gravity for greater than 10 ms. The atoms accumulate velocity until the resulting Doppler-shift separates the two resonance conditions for the interferometer, and enables operation of a Doppler-

sensitive interferometer. We find this delay of 10 ms to be excessively constraining in the operation of a high data-rate accelerometer, and thus opted for separate beams which have no such delay but generate additional phase noise.

After the interferometer, the population in $|F = 2\rangle$ and total atom number are detected by atomic florescence from two 100 μs pulses consisting of probe and probe with repump. The probe beam consists of 5.2 mW of light locked resonant with the $|F = 2\rangle \rightarrow |F = 3'\rangle$ D2 transition. This beam is retro-reflected to balance the photon scattering force and facilitate recapture. 1.2% of the atomic florescence is collected into an avalanche photodiode (Hamamatsu c5640-1). This figure is calculated from the imaging optics, as well as a window which defines the imaged area. At the time of detection, the atoms have fallen approximately 1 mm or less dependent on the interrogation time of the interferometer. This places them well within the capture volume of the MOT, so the trapping coils and cooling light are immediately enabled to recapture the ensemble. Additional loading from vapor replenishes the remaining atoms, and after a few milliseconds the cycle begins anew.

3.2 Performance

We evaluate the performance of the apparatus in two stages. We first consider the number of atoms in steady-state operation which presents an absolute limit to the sensitivity. This is driven primarily by the recapture efficiency. We then evaluate the interferometer itself, and discuss methods by which we may enhance the sensitivity and stability.

3.2.1 Recapture

Given a fixed cycle time, there exists some optimal recapture duration and interrogation time. The recapture duration must be sufficiently long to maintain reasonable atom number while sufficiently short to allow for maximal interrogation. We optimize this parameter for maximal sensitivity, and we find this optimal recapture duration to be on the order of 2 ms over a range of data-rates, which is comparable to the trap relaxation time $\tau_{\mathrm{MOT}} = 3$ ms. This optimal sensitivity occurs at approximately the same atom number of 2×10^5. We typically find this number to favor longer interrogation times over higher atom number. This is clearly indicative of the T^2 scaling of the sensitivity. Furthermore, this suggests the dominant noise sources are not atom shot noise limited.

We find the recapture efficiency to range from 95% to 85% at this optimal recapture duration, depending on data-rate and time-of-flight. This recapture efficiency is primarily limited by the recapture duration relative to the relaxation time of the trap, as the vast majority of atoms are well within the MOT capture volume and would be recaptured given sufficient time. We find the total atom number is primarily limited by the loading rate of the atoms. Our vacuum limited lifetime of $\tau = 1$ s is well above what is necessary for such a short interrogation. According to Eq. 2.35, we may expect to gain over an order of magnitude more atoms by moving to a higher vapor pressure. However, we found that the quality of our getters was limiting the purity of the source at higher currents.

3.2.2 Interferometer

We demonstrate operation of the interferometer with a cycle time of 10 ms (100 Hz) and an interrogation time of 3.415 ms. We believe this represents a favorable trade-off between being sufficiently fast for the dynamics we intend to investigate, while also

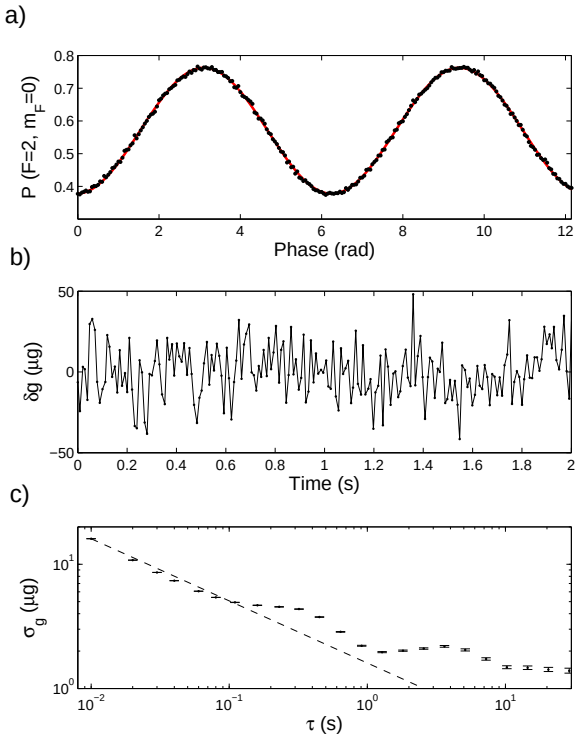

Figure 3.2: High data-rate accelerometer fringe results. a) We plot the interferometric fringe by sweeping the phase of the third Raman pulse. This plot is normalized to the number of atoms pumped into $|F = 1, m_F = 0\rangle$. b) A trace of the interferometer output at mid-fringe demonstrates high data-rate operation. c) The Allan deviation of a mid-fringe trace reveals the presence of systematic drift in the interferometer phase. Figure reprinted from [58].

demonstrating favorable sensitivity. Results are shown in Fig. 3.2. Part (a) shows the interferometer fringe by scanning the relative phase of the third Raman pulse. Part (b) shows a mid-fringe time record converted to units of acceleration. Part (c) is the corresponding Allan deviation. The shot to shot phase noise of 31 mrad corresponds to a sensitivity of 1.1 $\mu g/\sqrt{\text{Hz}}$. However, the stability of the device vanishes on a timescale of approximately 1 s. The dominant contribution to this noise source is found to be the optical phase due to path length variations. We find the magnitude of this noise to be 21 mrad at 100 Hz. Furthermore, we use a magnetometer to measure variations in the ambient magnetic field. We calculate the

noise contribution from the second-order Zeeman effect to be 15 mrad. This may be readily mitigated through the use of magnetic shielding. We attribute the remainder of the noise to a combination of detection, atom shot noise, and platform stability.

We seek to demonstrate the performance of the device over a range of data-rates. This is done by varying the time-of-flight, optimizing the duty-cycle at each rate for maximal sensitivity. We varied the data-rate from 50 Hz to 330 Hz. During this measurement, we noted the phase noise was approximately constant at 30 mrad/shot dropping by a mere 25% at higher data rates. This demonstrates that the noise in our system is largely due to the systematics described above. Additionally, we generally found each data point to optimize in favor of higher interrogation duration and lower atom number. This again indicates that the experiment was not limited by atom shot noise. The results are shown in Fig. 3.3. We find the sensitivity to vary from approximately 0.5 $\mu g/\sqrt{\text{Hz}}$ to 40 $\mu g/\sqrt{\text{Hz}}$. The duty cycle varies from 75% to 30% at higher bandwidths. This is consistent with an approximately constant recapture time, limited by the trap relaxation time τ_{MOT}. Additionally, the state-preparation and sub-Doppler cooling durations were also constant. Thus, there is a favorable increase in interrogation time at lower data-rates. This experiment also indicates successful operation with a 16 ms time-of-flight. That is, a significant number of atoms are still recaptured.

3.2.3 Gravity Measurement

As a demonstration of the acceleration sensitivity of the interferometer, we conducted a measurement of local gravity in the laboratory. This measurement was not intended to be a highly sensitive or accurate measurement of local gravity, but rather a demonstration of a high data-rate, absolute gravimeter.

We measure local gravity by measuring the interferometer phase shift as a function of the interrogation time T, as it is varied from 0 ms to 7 ms. The result is

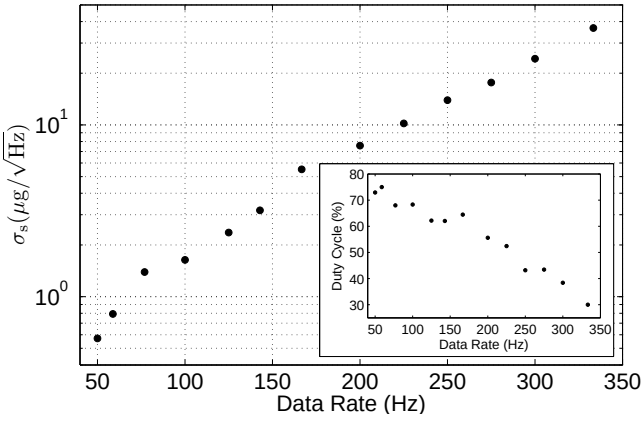

Figure 3.3: Performance of the accelerometer over a range of data-rates. We vary the data-rate of the experiment and optimize the interrogation time for maximal sensitivity at each data-rate. Inset: The duty cycle varies from 70% to 30% due to the optimization of the interrogation time and constant-time stages in the experiment (such as sub-Doppler cooling). Figure: The sensitivity of the device ranges from 0.5 $\mu g/\sqrt{\text{Hz}}$ to 40 $\mu g/\sqrt{\text{Hz}}$. It follows a $T^{3/2}$ scaling, indicating the phase noise to be largely constant. Figure reprinted from [58].

a chirped sine wave from which we may read out a continuous phase exceeding 2π radians. The total phase is given by,

$$\phi = \mathbf{k}_{\text{eff}} \cdot \mathbf{g}((1 + 2/\pi)\tau_\pi T + T^2), \tag{3.1}$$

where τ_π is the duration of a π pulse [70]. This equation varies from Eq. 2.18 as it contains the next higher order term proportional to T, which takes the finite Raman pulse duration into account. We note that in the limit of $T \gg \tau_\pi$, this additional term vanishes. There exists an additional term with this correction proportional to τ_π^2, which we ignore. The result of the measurement is shown in Fig. 3.4. The Raman beam was aligned to gravity using a weighted mass. We estimate the error of this procedure to be approximately 1 mrad. We find the value of local gravity to be $g = 9.79164 \pm 1 \times 10^{-5}$ m/s. This is in agreement with the measured benchmark [71] when taking into account the height difference of the measurements and the uncertainty of the direction of gravity. We note that this measurement was not

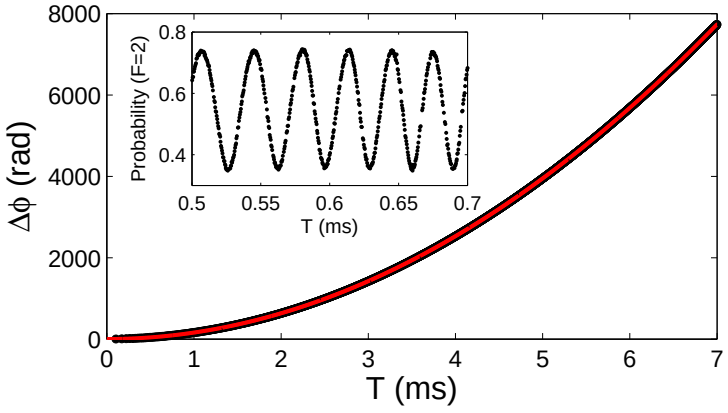

Figure 3.4: Demonstration of local gravity measurement with the accelerometer. A sweep of the interrogation time T results in a chirped sine wave (inset). Fitting to the local phase of this curve enables us to track the global phase over several thousand radians. We then fit the global phase and find the value of local gravity to be $g = 9.79164 \pm 1 \times 10^{-5}$ m/s. This is in agreement with an independent measurement [71]. Figure reprinted from [58].

intended as a precision measurement of gravity, but rather a demonstration of the device as an absolute accelerometer.

3.3 Sensor Enhancements

This prototype experiment confirmed many of the fundamental techniques which our ensemble exchange device will employ. First of all, recapture of the ensemble after interrogation has been successful at reaching target atom number and duty cycle. In fact, we find recapture enables significantly enhanced duty cycle, even with a 16 ms time-of-flight, and likely beyond. Secondly, the apparatus has demonstrated operation at and beyond our target data-rate. This demonstrates sufficient flexibility of our control system, and validates the use of high data-rate as a means of recovering some of the lost sensitivity. Finally, the apparatus has demonstrated the feasibility of a compact design, including compact trapping and bias coils, as well as

optomechanics.

The experiment also revealed many optimizations which we may apply towards the next apparatus. The first of these is the vapor pressure limitation from getters. At higher getter currents there was significant outgassing of species other than rubidium, which increased the background vapor pressure without comparable increases of loading rate. One possibility is to use higher quality getters, but a more permanent solution which doesn't require replacement and testing is desired. This inspired the use of a pure rubidium source from a crushed ampoule. These are typically used in conjunction with a differential pump to control the vapor pressure. However, this would represent a significant increase in system size and complexity. Thankfully, the vapor pressure of rubidium at room temperature corresponds to a background limited lifetime on the order of 0.1 s, which is sufficient for our purposes. Thus, we opted for a solution with a temperature controlled pure rubidium source without the use of a differential pump.

Another optimization lies with the Raman delivery system. While using separate fibers enabled the increased data-rate, the resulting phase noise due to optical path length fluctuations ended up limiting the sensitivity. Fortunately, the launch velocity of the atoms in the ensemble exchange device enables us to use techniques which places the two Raman colors on the same optical fiber and uses the Doppler shift to separate the resonance conditions. This is described in greater detail in the next section. The third optimization is in the size of the MOT beams. Increasing the size of the MOT beams increases the MOT capture volume. While this may not significantly improve recapture efficiency for the static device, it would likely increase the magnitude of dynamic stimuli the apparatus may endure. Finally, this experiment clearly demonstrated the need for magnetic shielding, as well as the necessity of a mechanically-stable design.

Chapter 4

Dual-Axis Sensor Apparatus and Experiment

We now present the construction of the sensor head and laser system for the ensemble-exchange device. This apparatus is designed to load and cool two MOTs from vapor located a few centimeters apart. The ensembles are then launched towards each other, and the Raman interrogation takes place during their ballistic trajectory. Finally, the atomic populations in each of the hyperfine states are detected, and the ensembles are recaptured in the opposing trap. We design the sensor head as a compact device which would serve as the physics package of an inertial sensor. The laser system is designed using bulk optics in free-space, and occupies a couple square meters. The engineering of a compact laser system was beyond the scope of this project. Our objective instead was to demonstrate successful operation within a compact physics package, in contrast to bulky vacuum systems and optomechanical delivery systems. We present this chapter in three sections describing the laser system, sensor head design, and the timing of the experiment.

4.1 Laser System

The laser system consists of the light and electronics necessary for trapping, launching, interrogating, and detecting the cold atomic ensembles. The system consists of a seeding and locking stage, an amplification and frequency-shifting stage, and a Raman stage. Each stage is on separate breadboards connected with optical fiber, should a mobile application be desired.

4.1.1 Seeding and Locking Stage

The seeding and locking stage provides a stable reference frequency for trapping, detection, and Raman light. The master laser consists of a Vescent Photonics CECL Laser Module, which provides 30 mW of light at 780 nm. Using standard saturated absorption spectroscopy techniques (sat. spec.) and an acousto-optic modulator (AOM), the laser is locked 53 MHz red of the $|F = 2\rangle \rightarrow |F = 2'/3'\rangle$ crossover transition in ^{87}Rb. This provides access to the $|F = 2\rangle \rightarrow |F = 2'\rangle$ and $|F = 2\rangle \rightarrow |F = 3'\rangle$ pumping and detection transitions using approximately 80 MHz AOMs single and double passed, respectively. However, we currently use a separate pumping laser on the D1 line, but opted to preserve the original master laser configuration.

We use 1 mW of the master laser light as a reference for the Raman offset lock. The remaining power is directed towards a double passed AOM which performs the sub-doppler cooling frequency and intensity ramp. This light, which is 140 MHz blue of the $|F = 2\rangle \rightarrow |F = 3'\rangle$ probe transition with a power of 5 mW is directed towards the amplification and frequency-shifting stage.

Additionally, this stage contains a separate repumping laser (EYP-DFB-0780-00080-1500-SOT02-0000) at 780 nm. This laser is locked to the $|F = 1\rangle \rightarrow |F = 1'/2'\rangle$ crossover transition using sat. spec. An AOM shifts the frequency to the $|F = 1\rangle \rightarrow |F = 2'\rangle$ transition and acts as a shutter, so 10 mW of power is directed towards

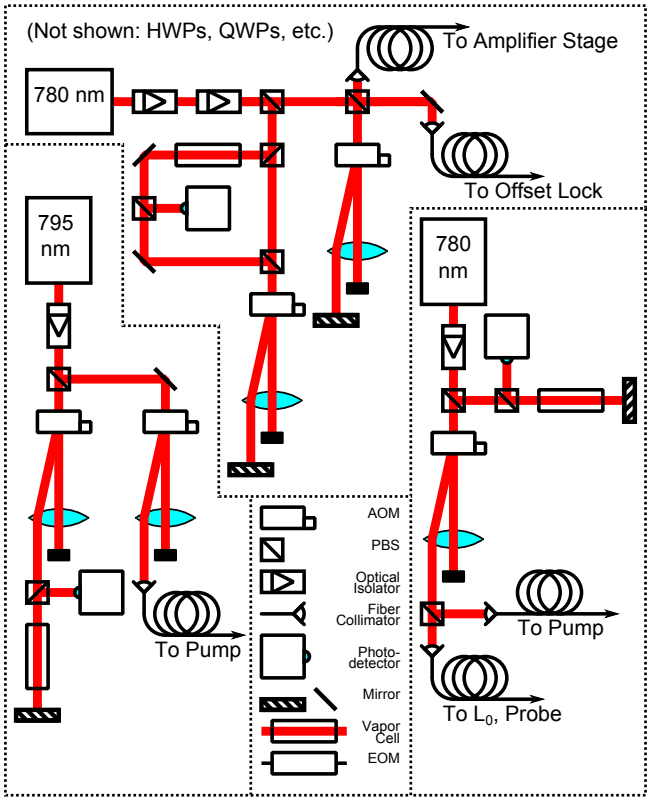

Figure 4.1: Diagram of the master laser stage. For clarity, certain optical elements such as half-wave plates and quarter-wave plates are omitted. A master laser at 780 nm provides the seed light for cooling and detection, resonant with $|F = 2\rangle$. A second laser at 780 nm provides the repumping light resonant with $|F = 1\rangle$. A laser at 795 nm provides the optical pumping light, resonant with $|F = 2\rangle$.

the sensor head for trapping, pumping, and detection. Another laser (EYP-DFB-0795-00080-1500-TOC03-000x) on the D1 transition at 795 nm provides the light for optical pumping. This laser is locked using sat. spec. to the $|F = 2\rangle \rightarrow |F = 2'\rangle$. By using a D1 laser, we suppress off-resonant pumping and achieve a 92% state polarization.

4.1.2 Amplification and Frequency-Shifting Stage

The reference 5 mW seeds an injection locked laser, amplifying it to 30 mW. This then serves as a seed laser for a tapered amplifier (Eagleyard EYP-TPL-0780-01000-3006-CMT03-0000). The 300 mW output is split into four branches: probe, and three cooling beams. Each branch is double passed through AOMs, bringing the frequency down to the $|F = 2\rangle \rightarrow |F = 3'\rangle$, and tunable by 20 MHz. The probe beam is locked on resonance, while the remaining beams are detuned 11 MHz red of resonance to serve as the cooling beams. One beam (designated L_0) is directed orthogonal to the launch direction of the ensembles, and contains zero frequency shift. The other two beams (designated L_+ and L_-) are directed 45° to the launch direction, and are blue and red detuned 2.2 MHz from the cooling frequency (respectively) to generate optical molasses in a moving frame at 2.5 m/s. These beams are delivered to the sensor head with optical fiber, where the L_0 beam is combined with repump light from the seeding and locking stage.

4.1.3 Raman Stage

The Raman master laser is an external cavity diode laser (ECDL) which generates 40 mW of power at 780 nm with a linewidth of 1 MHz. We use 1 mW of power with 1 mW of power from the master laser to generate a beatnote signal on a 12 GHz photodiode (Newfocus 1580-B). An error signal is generated by mixing in a reference oscillator and detecting a frequency-dependent phase shift introduced by a delay line [72]. This provides a robust and tunable locking scheme, locking the Raman beam 1 GHz red of the $|F = 2\rangle \rightarrow |F = 3'\rangle$ transition.

The remaining power seeds an injection locked laser, amplifying it to 100 mW. This output is split and directed towards two electro-optic modulators (EOMs), driven at the hyperfine frequency. The zero and a first order sideband of this light

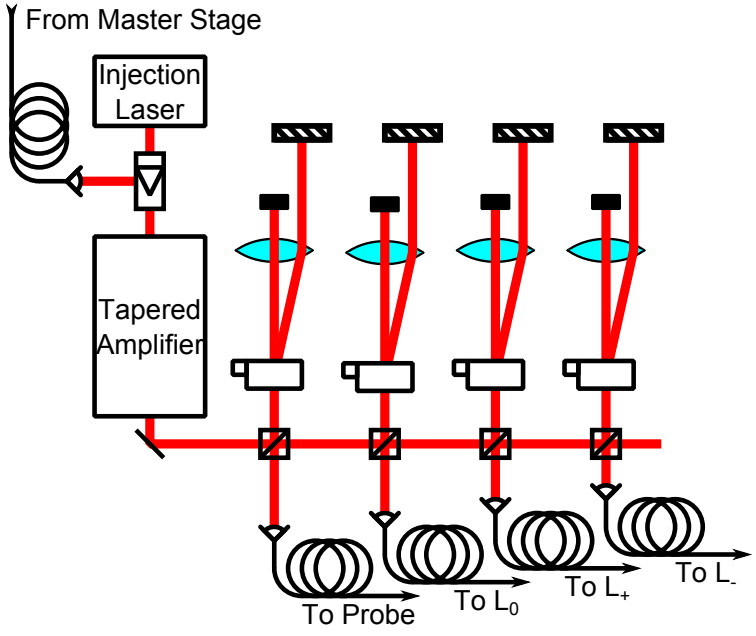

Figure 4.2: Laser amplifier and frequency-shifting stage. This stage amplifies light from the master 780 nm laser. This light is then split into the MOT and probe beams according to the detuning necessary to achieve the moving molasses.

generates the stimulated Raman transition. Two independent frequencies are needed to lock in to the Doppler shift and phase shift of each interferometer. A schematic of the microwave frequency chain is shown in Fig. 4.4. The hyperfine RF frequencies are generated from a 10 MHz oven-controlled crystal oscillator (OCXO), which is then multiplied up to 100 MHz by a phased locked oscillator (PLO). This is then directed to a distribution amplifier which provides a stable reference frequency for the whole lab. A Dielectric Resonator Oscillator (DRO) multiplies the frequency up to 6.8 GHz. Finally, the two channels of a DDS supply 34 MHz frequency modulation through two single-sideband modulators, configured to enhance the upper sideband. These are amplified, and directed towards the electro-optic modulators. The RF power is set so that the first order sidebands are approximately the same amplitude as the carrier. Further tuning is optimized to nullify the differential light shift.

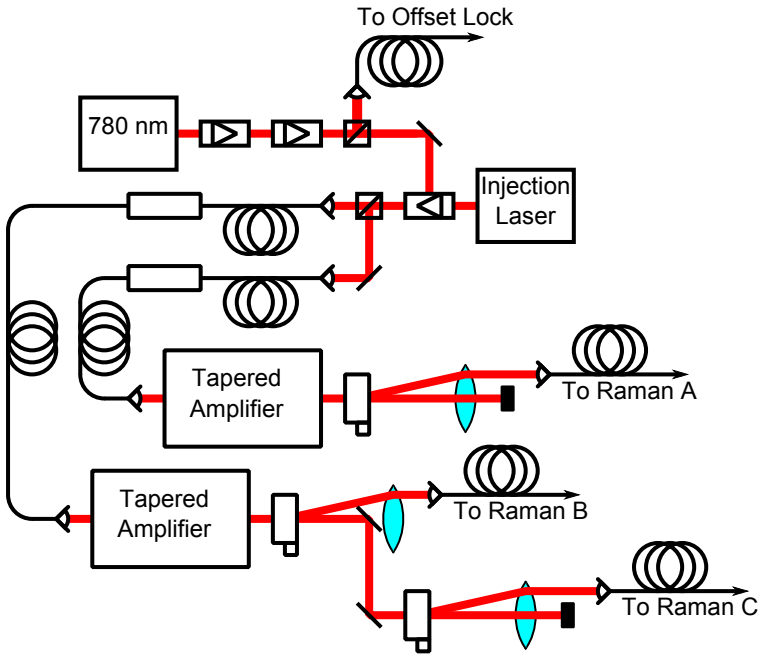

Figure 4.3: Raman laser stage. The Raman master laser is locked 0.9 GHz red of the master laser reference using a phase-sensitive beatnote lock. This light is then amplified and delivered to two electro-optic modulators which generate sidebands near the hyperfine frequency. The light is again amplified and delivered to the Raman laser modules. The original design contained a single EOM and TA, and provided light for all three Raman beams.

Each of these beams is amplified by a TA (Eagleyard EYP-TPL-0780-01000-3006-CMT03-0000), and switched using AOMs. The beams are delivered to the sensor head via optical fiber, with a peak power of 80 mW per beam. One tapered amplifier supplies power for the leftmost Raman beam (labeled A), while the other is switched between the middle and right beams (labeled B and C, respectively). Earlier designs featured just a single EOM and TA supplying power for all three beams.

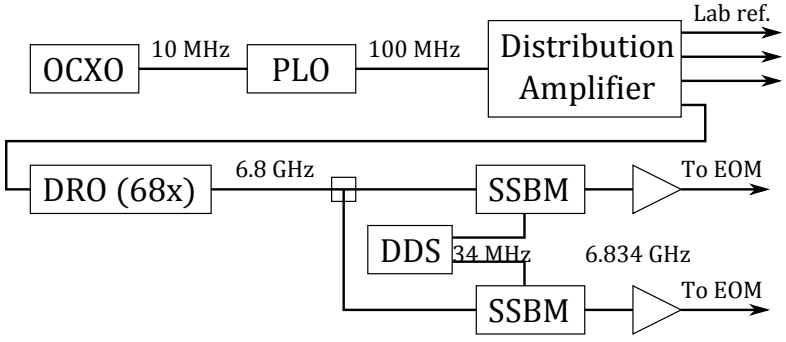

Figure 4.4: Schematic of microwave frequency generation. An oven-locked crystal oscillator and phase locked oscillator form a stable 100 MHz reference for the lab. A dielectric resonance oscillator multiplies the frequency to 6.8 GHz, and the RF is split. A modulation of approximately 34 MHz is mixed in using a DDS and two single-sideband modulators to reach the hyperfine frequency. The use of a single DDS ensures phase coherence between the two frequencies. The output of the SSBMs is amplified and directed to two EOMs. The original design used a single SSBM and EOM.

4.2 Sensor Head

There has been great interest in constructing compact magneto-optical traps for field deployment. Some of the techniques employ fabrication [73] of pyramid MOTs [74] or diffraction MOTs [75]. This has motivated investigations in the number of atoms achieved as a function of laser beam size and intensity [76] and other experimental parameters. A review of these techniques and advances in this field may be found in [77]. Unfortunately, the requirement of launching the atoms prevents the use of many of these techniques, as most of them employ the use of a single laser beam. However, application of these techniques towards an atom interferometer accelerometer is feasible.

As such, we have opted to use a traditional six-beam MOT engineered with a compact design. The sensor head consists of a vacuum system and a compact optomechanical assembly. The assembly resides in a 2 foot by 2 foot magnetically shielded

box constructed from Mu-metal. Optical fibers and electrical cabling are delivered through a 1.5 inch cylindrical Mu-metal sleeve. The light is split using evanescent waveguides configured as coupler arrays located inside the magnetic shielding.

4.2.1 Vacuum System

The vacuum system is built around a $20 \times 30 \times 60$ mm^3 quartz cell with 3 mm thick walls. The system consists of the cell, a pure Rb source from a crushed ampoule, an ion pump, and vapor density window probe. The Rb vapor pressure is controlled through the use of a cold point, typically maintained at 20 °C using a thermoelectric cooler mounted to the neck of the Rb source. This maintains a vapor pressure of approximately 2×10^{-7} torr.

4.2.2 Optomechanical Frame

The optomechanical frame is built around the vacuum cell and supports the necessary optics for trapping, launching, interrogating, and detecting the cold atomic ensembles. A conceptual diagram of the sensor is shown in Fig. 4.5. Additionally, a CAD model is shown in Fig. 4.6 and pictures of the sensor in Fig. 4.7. It was machined out of the insulator G10 to diminish eddy currents [78], and maintains a thermal expansion coefficient similar to that of aluminum. The time-constants for magnetic field switching are on the order of 20 μs. This ensures a sufficiently stable magnetic field during the interrogation time of our high bandwidth experiment.

The optomechanical frame uses optical access along four independent geometric planes to densely pack the required 19 optical beams and achieve a compact design. Furthermore, the frame is designed to be modular with detachable cooling, detection, and Raman assemblies. In fact, throughout the lifetime of the apparatus both the detection and Raman assemblies were replaced. The cooling assembly uses compact

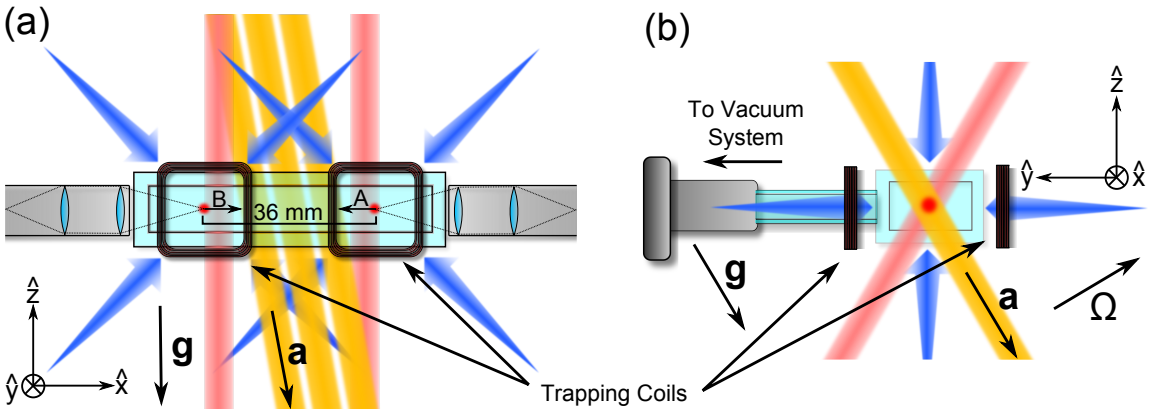

Figure 4.5: Diagram of the sensor head design. a) Front view. The cooling beams are shown in blue, probe beams in pink, and Raman beams in yellow. Detuning the outer and inner cooling beams blue and red of the cooling frequency (respectively) results in optical molasses moving towards the center of the cell. The ensembles then undergo state-preparation, Raman interrogation, and detection before being recaptured on the opposing trap. b) Side view. The design boasts four planes of optical access in a compact geometry. The direction of acceleration measurement is given by the direction of the Raman beams. The rotation measurement direction is $\mathbf{k}_{\text{eff}} \times \mathbf{v}$, pointing towards the front at a slight angle. Figure reprinted from [59].

flexure mounts with free space fiber mounts and polarization control. We find that a useful and compact simplification is to employ uncollimated cooling beams that diverge freely from the fiber at a half-angle of 5 degrees [8]. The detection modules feature counter-propagating and balanced detection beams for each ensemble, and polarization control. The detection beams each consist of a probe locked to the $|F = 2\rangle \rightarrow |F = 3'\rangle$ transition to measure the population in $|F = 2\rangle$ and a repumper locked $|F = 1\rangle \rightarrow |F = 2'\rangle$ transition to measure the total atom number.

The Raman beams are delivered to the experiment by a common optical fiber. The Raman assembly collimates the light, and splits it into three beams using half-wave plates and polarizing beamsplitters. Normally, this would generate a Doppler-free interferometer, since the beams are traveling along the same direction. However, we orient the beams 10° from the perpendicular of the launch direction, and retro-reflect by a common mirror. This projects a component of the beam along the launch

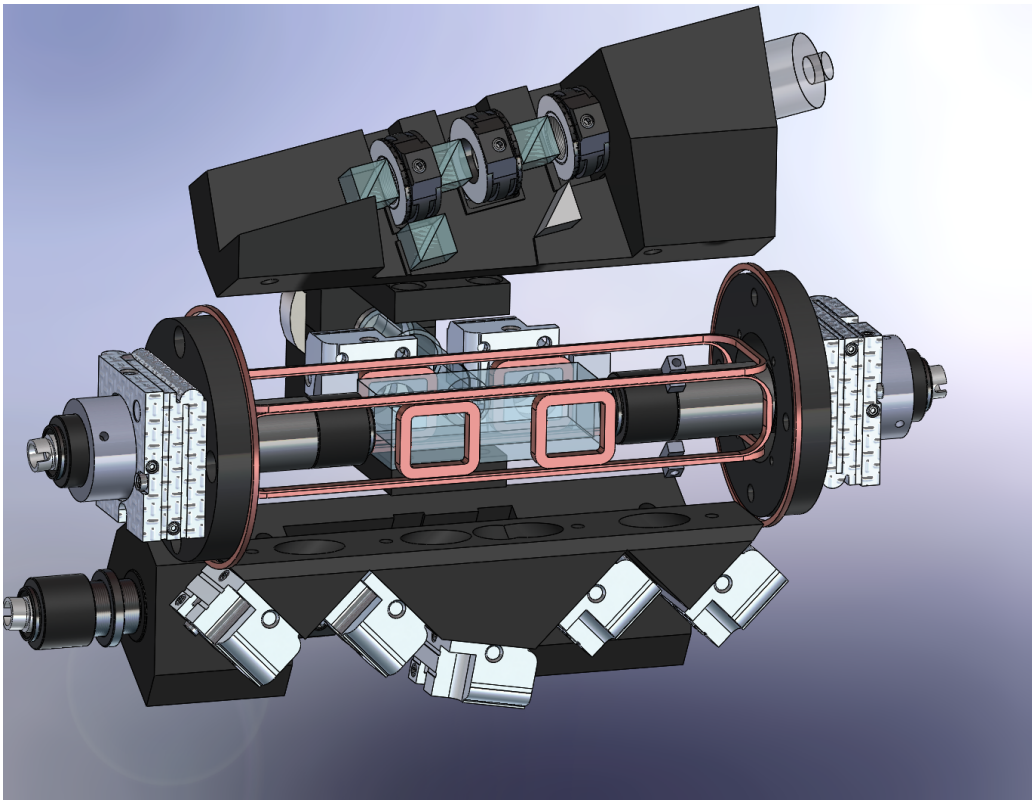

Figure 4.6: CAD model of the sensor head. Half the cooling assembly, one probe module, and the mounting frame are not shown for clarity. The optomechanical frame is machined from G10.

velocity. This results in a Doppler shift for both the original beam and the retro-reflected beam, but opposite in direction. Thus, by selecting a detuning of magnitude $\mathbf{k}_{\text{eff}} \cdot \mathbf{v} = k_{\text{eff}} v \sin(10°)$, we generate a resonant Doppler-sensitive interaction using one of the original beams and the other retro-reflected beam. This eliminates systematic phase noise from having the beams be delivered by different fibers, using the mirror as a common inertial reference. The second advantage of this technique is that the alignment is simplified immensely. If the beams were independent, each beam would have to be precisely aligned to close the interferometer. That is, at the end of the experiment the two arms of the interferometer must align to within the de-Broglie wavelength of the atom. With our experiment, this corresponds to an angular

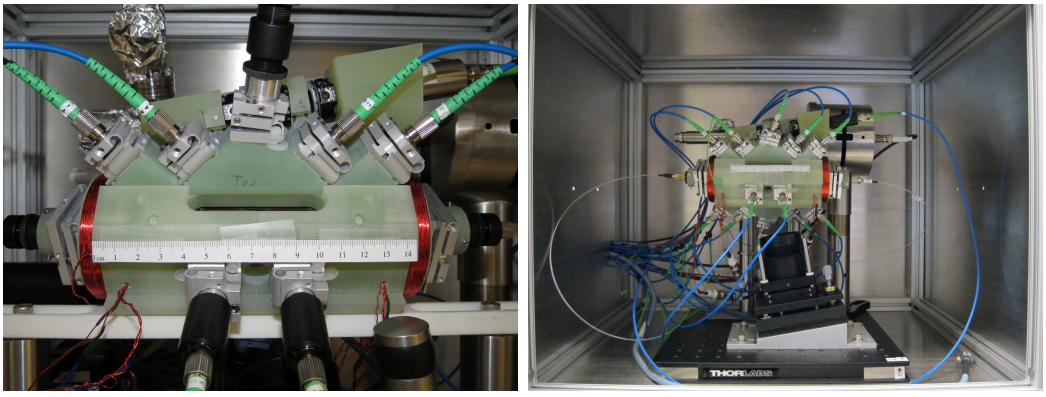

Figure 4.7: Pictures of the assembled sensor head. The vacuum cell is not visible from this viewpoint. The front detection module is removed for clarity. The right picture shows the magnetic shielding and Raman retro-reflecting mirror.

resolution of approximately 1 μrad or 0.2 arcsecond. Fortunately, by this technique and the law of reflection, the direction of $\mathbf{k}_{\text{eff}} = \mathbf{k}_1 - \mathbf{k}_2$ is orthogonal to the surface of the mirror, independent of the direction of the input light. However, this input light must be aligned to the mirror orthogonal to preserve the Rabi frequency, due to the finite beam size. This constraint is significantly more relaxed, with a resolution of 10 mrad which is 4 orders of magnitude higher.

The original Raman module contained a single fiber input which was split into three with half-wave plates and polarizing beamsplitters. There were a couple drawbacks to this design. First, the beamsplitters were fixed, and thus so were the Raman beam orientations. The Raman wavevector was still fixed, but any deviation in the input beam results in reduced pulse efficiency. Furthermore, there was a fixed offset between the center of the Raman beam and the center of the ensemble. Secondly, by using a single Raman beam the detunings and offset phase for each interferometer were fixed. Finally, there was additional dead-time in the experimental cycle as the ensembles traveled from pumping region to the Raman beams, and from the Raman beams to the detection region. This limited our interrogation time to $T = 4.0$ ms. Since then, we have upgraded to a system which supports three independent Raman

beams which may be individually positioned and oriented. This allows us to align the center of the beam with the center of the ensemble, and separate the beams further, increasing our interrogation time to $T = 4.5$ ms. Furthermore, the separate beams allow us to set independent phases and frequencies for all but the middle (second) pulse, which is shared between the interferometers.

4.2.3 Magnetic Field Geometry

The quadrupole trapping magnetic field is generated from two pairs of trapping coils (approximately 16 mm in length) located 36 mm apart. At this separation distance, there is a great deal of interference between the quadrupole pairs. Therefore, the magnetic field geometry changes based on the relative alignment of the quadrupole field polarities (parallel or anti-parallel). In particular, we are concerned with two factors. First, how significantly the location of the trap center shifts. Second, the distance over which the field gradient is maintained may limit the capture volume of our MOT.

We calculate the magnetic field geometry in both the parallel and anti-parallel case. See Fig. 4.8. First, we note that the parallel case shifts the magnetic field zero by 2 mm towards the center. The anti-parallel case shifts the zero 2 mm away from the center. Thus, the magnitude of the shifts is the same in both cases, and must be taken into account when aligning the cooling beams. Next, in the parallel case we observe an additional zero at the center of the cell. However, the polarity of the field is opposite to that of the primary traps. Thus, taking into account both the alignment and polarization of the cooling beams, it is highly unlikely that any atoms would be trapped in the center. Finally, we observe that in the parallel case, the magnetic field gradient vanishes approximately 5 mm towards the center of the cell. In the anti-parallel case, the gradient in maintained for over 10 mm. Thus, we decided to configure our magnetic field coils to use the anti-parallel alignment.

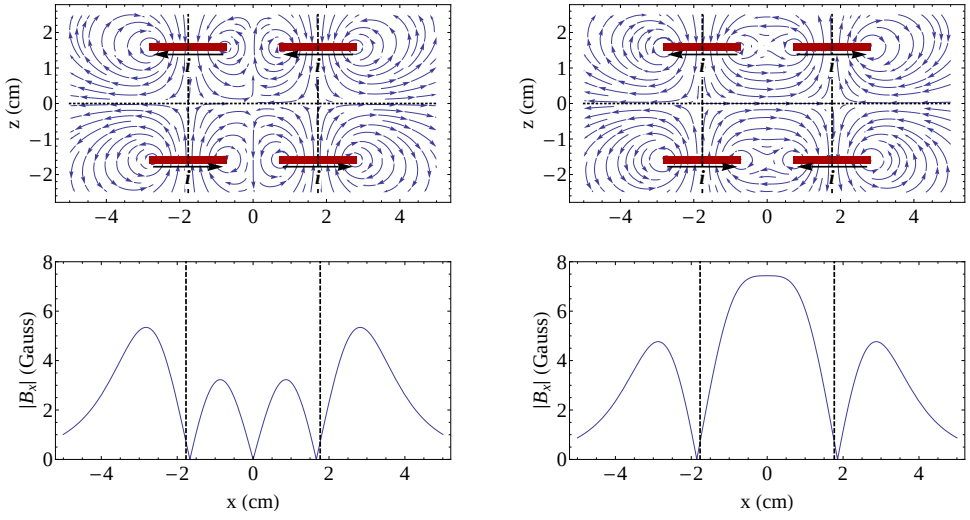

Figure 4.8: Magnetic field geometry from quadrupole coil pair in close proximity. The left and right arrangements are configured with the quadrupole axes parallel and anti-parallel, respectively. The bottom plots depict the magnitude of the magnetic field in an axis between the coils, along which the ensembles would launch and travel. The parallel geometry reveals the presence of an additional field zero at the center of the cell. While this wouldn't trap atoms (since the cooling beams are polarized oppositely to this) there is a significant reduction of the magnetic field gradient. The anti-parallel geometry maintains this gradient. Both configurations generate a slight offset in the magnetic field zero, which much be accounted for when aligning the cooling beams.

We also employ compact bias coils in three directions which are slightly larger than the size of our vacuum cell. Thus, we must consider any fringing effects of the magnetic field during the interrogation, which would result in frequency errors due to the second-order Zeeman shift. We calculate the magnetic field of our bias coils numerically, and find the error to be less than 1 mG over the ensemble trajectory.

4.3 Timing Sequence

Given a fixed interrogation time on the order of a few milliseconds, it is imperative to minimize the cycle time of the experiment in order to increase bandwidth and

maximize sensitivity. Therefore, a strict timing sequence must be maintained which makes optimal use of the available cycle time. Even a loss of 1 ms could result in significant loss of sensitivity.

4.3.1 Ensemble Exchange Timing

A conceptual diagram of the timing sequence is shown in Fig. 4.9. The timing cycle begins with atoms trapped in a MOT, and the quadrupole field is shut off. Over 0.2 ms, the L_+ and L_- beams are detuned to generate optical molasses in the moving frame and launch the atoms. A detuning of 2.2 MHz results in an ensemble velocity of 2.5 m/s.

Then, over 1 ms all cooling beams are ramped down by 40 MHz and the power is lowered by 90% to sub-Doppler cool the atoms. In this process known as Sisyphus cooling or polarization-gradient cooling, the oppositely-polarized MOT beams interfere, and form a standing-wave pattern which has a spatially-dependent polarization [79]. As atoms move through this potential landscape, they lose kinetic energy in favor of potential energy at the potential maxima. They then undergo optical pumping into the lower energy state, having shed their potential energy into the light-field. The process is repeated over many cycles, drawing analogy to the figure Sisyphus from Greek mythology, who for all eternity was condemned to roll a boulder up a mountain only to have it roll down again. The decrease of cooling power and increase in optical detuning are to suppress resonant photon scatter which limits the ensemble temperature to the Doppler temperature. Theoretically, the temperature limit for this process is given by the recoil limit, which is 362 nK for the D2 transition in ^{87}Rb. In practice, this temperature is difficult to achieve, limited by the time available for cooling, polarization purity, and intensity & frequency control. Typical experiments achieve a temperature of a few μK [80].

After the cooling process, the cooling beams are shut off, and the atoms are illu-

minated by the D1 pumping beam for 100 μs, which pumps 92% of the atoms into $|F = 2, m_F = 0\rangle$. This optical pumping technique uses the fact that the $|F = 2, m_F = 0\rangle \rightarrow |F' = 2, m_F = 0\rangle$ transition with π-polarized light is forbidden. Thus, by tuning a laser resonant with $|F = 2\rangle$ to this transition and repumping the atoms from $|F = 1\rangle$, the atomic population cycles until it reaches the $|F = 2, m_F = 0\rangle$ state, which is dark to the pumping laser. By leaving the repumping laser on for 10 μs longer than the depumping laser, we ensure the $|F = 1\rangle$ state is completely depopulated. Many cold atom experiments perform additional state purification where a microwave π pulse transfers the atoms from $|F = 2, m_F = 0\rangle$ to $|F = 1, m_F = 0\rangle$. The atoms remaining in the $|F = 2\rangle$ manifold are then blasted away with resonant light. However, we find it beneficial to maintain these spectator atoms in the ensemble in order to facilitate loading for the next shot of the experiment. At this stage, the temperature of the ensemble is approximately 30 μK. We believe this temperature is limited by the ensemble velocity, as the atoms leave the cooling beam volume during the sub-Doppler cooling process. The atoms are now traveling ballistically towards the other end of the cell. At this stage, we would perform the interferometer which we describe in subsection 4.3.2.

After the interferometer, the atoms are now located near the opposite end of the cell, just before the traps. The transition probability is detected by fluorescence detection from two 100 μs pulses. These pulses are comprised of probe and probe with repump light to measure the population in $|F = 2\rangle$ and the total atom number. The scattered light is imaged into a multi-mode fiber and directed into an Avalanche PhotoDiode (APD) [Hamamatsu C5460-01]. A total of 0.5% of the scattered light reaches the APD. The atom number is calculated from the photodiode signal by calculating the photon scattering rate from the probe, which in conjunction with the fraction of scattered light imaged, photodiode quantum efficiency, and amplifier gain results in a scale factor for volts into atom number.

Finally, the traps are activated and the ensembles are recaptured in the opposing

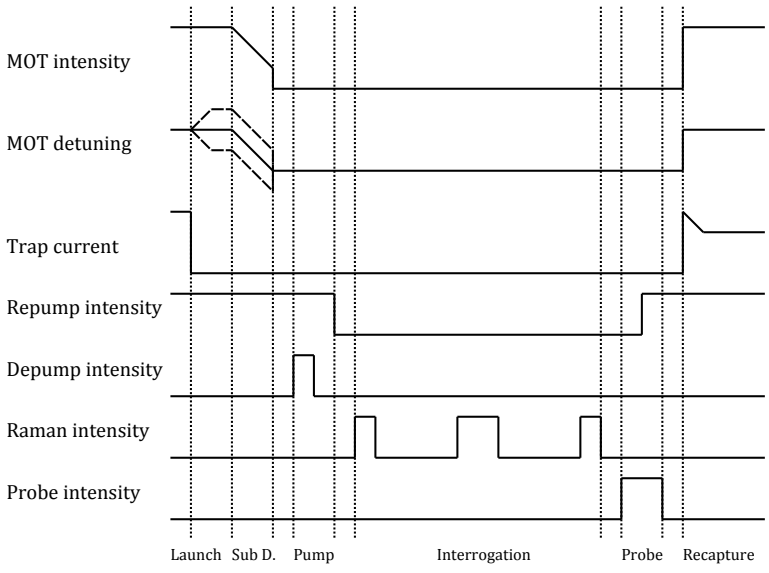

Figure 4.9: Timing diagram of the experiment (not to scale). This diagram depicts the entire experimental cycle, lasting approximately 10 ms to 20 ms. Unlike many cold atom experiments, the loading and recapture duration of a few milliseconds is on a timescale similar to the other stages of the experiment. Optimizing this cycle to make optimal use of the allotted time is critical to achieving maximal sensitivity. Most of these parameters were determined empirically by optimizing for maximal atom number and sensitivity.

trap zone. One optimization we discovered was to activate the traps before the ensemble reaches the trap center. This allows the ensemble to relax into the trap while loading atoms from vapor as early as possible. Atoms are recaptured and loaded over 4 ms, during which the atom number reaches the original steady-state value. Then, the next cycle of the experiment begins again. Another technique we discovered was to begin the recapture process with a high magnetic field gradient, limited by the maximum current supplied to the coils. This decreased the trap time-constant τ_{MOT}, and thus allowed the ensemble to quickly relax towards the trap center. Then, as the number of trapped atoms increased we slowly ramped down the field gradient over 2 ms to increase the trap volume. We found that this increased our steady-state atom number by 10%. Furthermore, we believe it is possible to

optimize this technique further and observe additional gains.

We constructed a video of the ensemble exchange process by varying the delay trigger of a CCD camera (Lumenera LM135) over multiple shots of the experiment. Select frames from this video are shown in Fig. 4.10, with the full video available at [81]. At the middle of the video, the trapping beams are turned off so that the Raman interrogation may take place without additional photon scatter. We found that by taking a series of pictures at a fixed time prior to recapture (13 ms), we may optimize the alignment of the cooling beams in favor of ensemble size and position with respect to the trap center.

4.3.2 Interferometer Timing

The timing of the Raman pulses is constrained by the ensemble velocity and Raman beam separation. We assume an ensemble velocity of 2.5 m/s which was used for most of the experiment. The original Raman module used a single input fiber with beams separated by 1 cm. The interferometer begins with all three beams pulsed 3 ms from the start of the cycle, separating the wavepackets. At this point, the atoms have been ballistic for 1.5 ms. Then, 4 ms later the beams are pulsed again as the two ensembles are spatially overlapped, redirecting the wavepackets. Finally, after another 4 ms the beams are pulsed, recombining the paths and forming the interferometer. After 0.5 ms, the detection takes place as described previously, and the atoms are recaptured for the next shot.

An FPGA maintains a set of frequency and phase registers for the first two pulses, and a second set for the final pulse. The frequency and phase values are programmed to the Raman DDS 20 μs before the first and third pulses. The second pulse uses the frequency and phase values of the first pulse. The frequency values are chosen to be an intermediary value between the two ensemble resonances. This will be described in greater detail in the next chapter.

The timing for this experiment is constrained by the fixed separation of the Raman beams. Indeed, as described previously there is additional dead time of 0.5 ms between the optical pumping and Raman interrogation, and between Raman interrogation and detection. This is due to the time it takes the ensemble to travel between the various laser beams. Ideally, the separation distance of the Raman beams is increased to eliminate this dead time. This is one of the issues addressed with the upgraded Raman module, as will be described later.

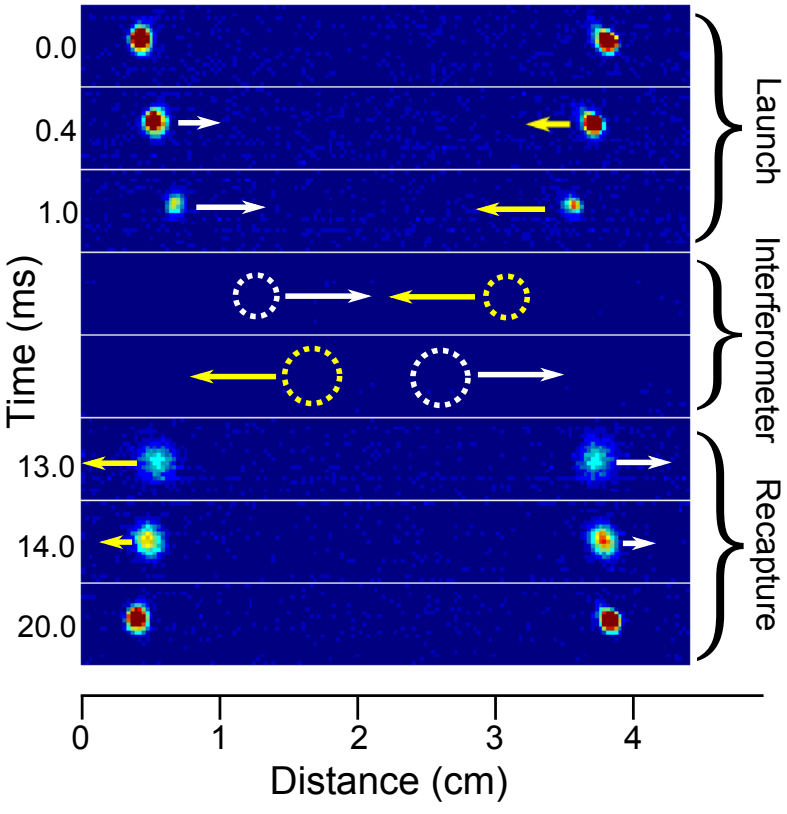

Figure 4.10: Frames from a movie [81] demonstrating ensemble exchange. The launching step includes sub-Doppler cooling which decreases the intensity of the cooling light, resulting in reduced photon scatter. The cooling beams are shut off during the Raman interrogation to reduce photon scatter. The traps are activated prior to the ensemble reaching the trap center. This allows the ensembles to decelerate into the traps, while giving an extra millisecond for vapor loading. The recapture duration is extended to 7 ms for this video to allow for higher atom number and thus a more clear picture. Figure reprinted from [59].

Chapter 5

Dual-Axis Sensor Performance

We now demonstrate and evaluate the performance of the apparatus in two parts. We first consider the magnitude of the flux of ultracold atoms provided by the ensemble-exchange technique, independent of the interferometer. This enables us to evaluate the potential of the ensemble-exchange technique when applied to other cold atom experiments. The latter half deals with the performance of the interferometer itself.

5.1 Ensemble Exchange

We quantify the performance of the ensemble exchange technique by both the achieved atom number and recapture efficiency. By treating these metrics independently, we may consider both our achieved performance loading the ensemble from vapor, as well as an enhanced (although more complex) system loading from another source, such as a 2-D MOT. The performance of such a system may be predicted by using the same recapture efficiency, but scaling up the loading rate accordingly.

5.1.1 Recapture Efficiency

We measure our recapture efficiency using two methods. First, we observe the atomic fluorescence as atoms load into the trap, on a timescale of τ_{MOT}. There are two elements to this process. First, atoms are loaded into the trap from a nearby ensemble (recapture). This is a highly complicated process based on a wide set of parameters including MOT capture volume, imaging volume, capture velocity, ensemble spatial distribution, and ensemble velocity distribution. However, we have found we can approximate this loading process as a Gaussian curve, with width τ_r which is on the order of τ_{MOT}. The second element to this loading process is loading atoms from atomic vapor. In this timescale where $\tau_{\mathrm{MOT}} \ll \tau_{\mathrm{bkgd}}$, we may approximate the vapor loading as linear in time. Thus, the total trap loading function is given by:

$$N(t) = N_0(1 - e^{-t^2/(2\tau_r^2)}) + \alpha t. \tag{5.1}$$

By fitting to this curve, we calculate the recapture efficiency as $r = N(t_r)/N_0$, where t_r is the total time spent recapturing. Fig. 5.1 shows the signal from an APD as atoms enter the trap. By fitting this function, we find a recapture efficiency of 85%. We note that this recapture efficiency includes the background collisional loss as the ensemble travels to the loading region.

The second method we use to determine recapture efficiency is based on equation Eq. 2.33. Here, we monitor the total atom number over multiple shots of the experiment, and over a range of vapor pressures. Given an independent measurement of α vs β, this enables us to calculate the recapture efficiency and steady-state atom number as a function of vapor pressure, which we quantify with the parameter β. This independent measurement was carried out by measuring MOT loading rates *without* ensemble exchange, over a range of vapor pressures. As expected, we found a constant ratio for α/β.

We now carried out the experiment with ensemble exchange. Beginning with zero atoms, we trigger the cycle to begin and ensemble exchange builds the population

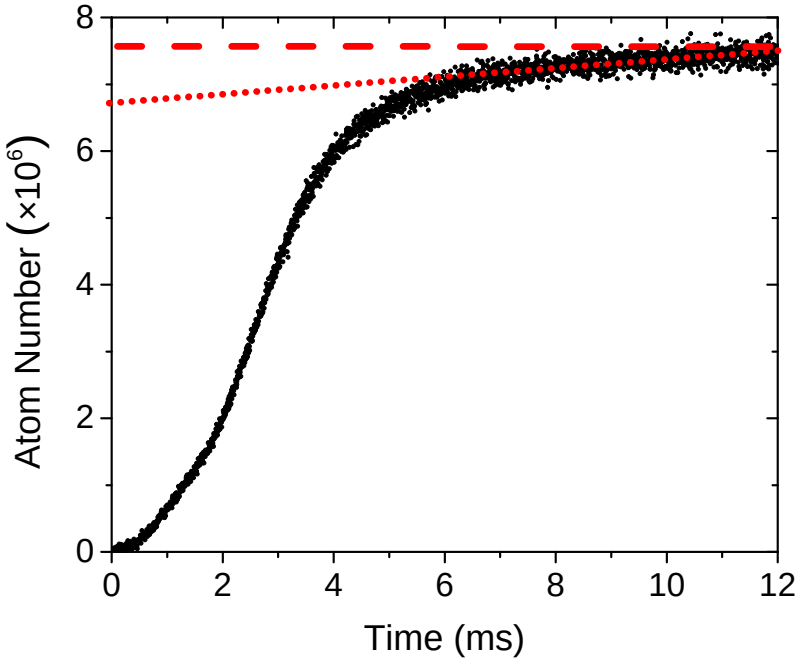

Figure 5.1: APD signal as the ensemble is being recaptured. The initial bump represents recapture of the ensemble. There is an overall linear trend corresponding to the loading of atoms from vapor. By subtracting out this contribution and dividing by the total atom number, we find a recapture efficiency of 85%. Figure reprinted from [59].

to a steady-state over approximately 40 cycles. This growth is depicted in the inset of Fig. 5.2. By fitting N_n as a function of shot index n, as per Eq. 2.33, we are able to derive the recapture efficiency r and steady-state atom number N_s. In this particular inset, we have $r = 89\%$ and $N_s = 4.2 \times 10^6$. Given the ratio of α/β calculated previously, we may derive the atom loss coefficient $\beta = 3.3$ 1/s.

We now perform this measurement over a range of vapor pressures, again quantified by β. We control the vapor pressure by closing the valve to the Rb source for 1 week and allowing the system to pump down. Then, we opened the valve and took the measurement periodically as the pressure built over the course of a few hours. Fig. 5.2 shows the recapture efficiency r and steady-state atom number N_s as a function of the vapor pressure. We find the recapture efficiency to be linear in β,

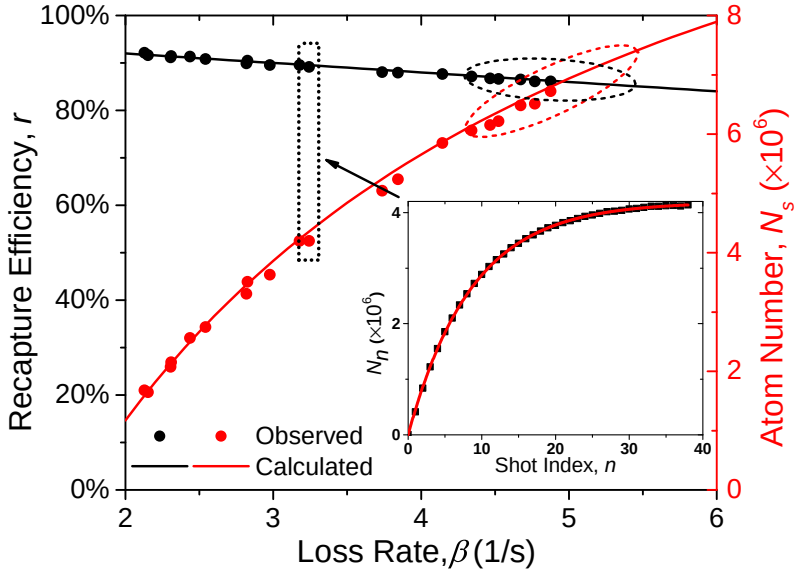

Figure 5.2: Atom number and recapture efficiency over a range of vapor pressures. Inset: Atom number as a function of shot index. The atomic population builds over approximately 40 cycles until it reaches steady-state. This is fit to Eq. 2.34 to extract the recapture efficiency and total atom number. Figure: We plot this recapture efficiency r and total atom number N_s as a function of vapor pressure, quantified by the background-limited loss rate β. Dashed circles show the typical operating regime for the interferometer. Figure reprinted from [59].

as expected by the definition $r = r_0 - \beta T_c$. We extrapolate this expression to zero background loss ($\beta = 0$) and find a base recapture efficiency $r_0 = 96\%$. This indicates that simply as a function of the ensemble overlap with the trapping volume, 96% of atoms are recaptured. This suggests that increasing the time-of-flight even further is feasible. The figure also depicts our typical operating parameters, corresponding to approximately 7×10^6 atoms.

From these measurements, we find the ensemble-exchange technique provides a consistent and robust flux of ultracold atoms with minimal loading time. Furthermore, we find our data agrees well with the theory presented earlier. By increasing the size and power of the MOT beams, we suspect achieving 1×10^7 atoms is feasible, along with a higher time-of-flight.

5.2 Interferometer

We now conduct an analysis of the interferometer performance. We construct the interferometer using a $\pi/2 - \pi - \pi/2$ pulse sequence of Doppler-sensitive Raman transitions. The Raman laser is split into three beams which provide the light for the transition at three places along the atomic trajectory. The available light must be optimized for each of the three pulses, as well as the two ensembles. As such, the data below represents the performance when optimizing conditions for all three pulses simultaneously, thus optimizing the interferometer readout.

5.2.1 Doppler-Sensitive Raman Pulse

Rabi flopping of the Raman pulse is shown in Fig. 5.3. These plots are generated by sweeping the duration of a Raman pulse, delayed by $0, 4, 8$ ms from the start of the interferometer. This pulses all three beams simultaneously, enabling us to observe Rabi flopping when the ensemble is overlapped with any of the three beams. The spatial and velocity distribution of the ensemble reduce the π pulse efficiency to 70% for the first pulse. The expanding spatial distribution decreases the pulse efficiency over time, down to 40% for the final pulse 9 ms later. The Rabi frequency is tuned to be approximately equal for all three pulses by balancing the beam intensity. Since both ensembles share the same duration Raman pulse, it is necessary to optimize the alignment to be balanced between the ensembles as closely as possible to ensure the same Rabi frequency. In practice, this is a difficult alignment as for this experiment, the relative alignment of the Raman beams is fixed. However, we manage to find a sufficient compromise.

A frequency scan of the Raman hyperfine detuning is shown in Fig. 5.4. We generate this plot by sweeping the Raman DDS frequency which drives the EOM. The two resonances result from the Doppler shift as a component of the Raman beams

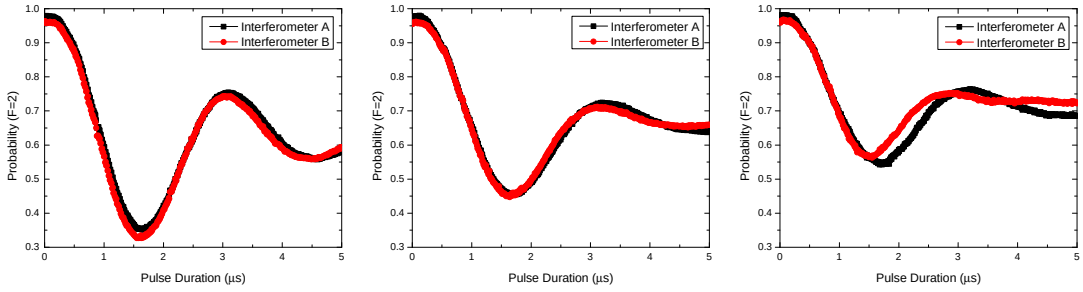

Figure 5.3: Rabi flopping for each of the three interferometer pulses. The expanding spatial distribution of the ensemble causes the pulse efficiency to decrease from 70% to 40%. The Rabi frequency is approximately $\Omega_{\text{eff}} = 2\pi \times 300$ kHz.

is projected along the launch velocity of the atoms, as described in subsection 4.2.2. By choice of resonance, this enables us to select a particular direction of the Raman wavevector $\mathbf{k}_{\text{eff}}$, generating the Doppler-sensitive transition. Due to the sign of the Doppler shift, given a choice of resonance we have one interferometer operating at $+\mathbf{k}_{\text{eff}}$ and the other at $-\mathbf{k}_{\text{eff}}$. From our launch velocity of 2.5 ms, we calculate a Doppler shift of $k_{\text{eff}} v \sin(10°) = 2\pi \times 1.1$ MHz, which is what we observe in the figure.

The two plots in the figure correspond to the time of the Raman pulse, either 2 ms or 11 ms from launch. As the atoms travel their ballistic trajectory, the resonances separate. This is due to the Doppler shift corresponding to the atoms' velocity as the accelerate under gravity. The magnitude of this chirp is given by $\mathbf{k}_{\text{eff}} \cdot \mathbf{g} = 2\pi \times 24.7$ kHz/ms. With a single Raman beam apparatus, we are unable to correct for this chirp. Thus, we select an intermediate frequency for all three pulses. This maintains interferometer contrast for both ensembles, although at a reduced amplitude. Furthermore, this drives pulses off resonance, which compromises the stability of the interferometer. With our closed loop interferometer where we add an independent Raman laser, we may correct for this shift in the first and third pulses. However, the second pulse uses a single Raman beam which is shared for

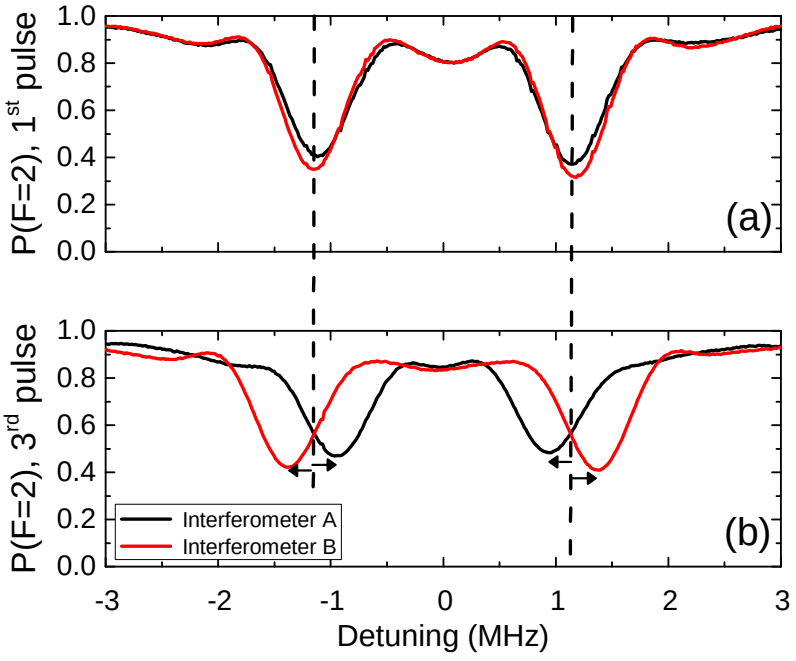

Figure 5.4: Frequency scan of the Raman hyperfine detuning, δ. (a) Two resonances are revealed corresponding to opposite directions of the Raman wavevector. (b) Gravitational acceleration and the Doppler-shift cause the resonances to separate by $\mathbf{k}_{\text{eff}} \cdot \mathbf{g} = 2\pi \times 24.7$ kHz/ms. We choose an intermediate resonance frequency to drive both interferometers simultaneously. Figure reprinted from [59].

the interferometers, and is still driven off-resonantly. Unfortunately, this represents a fundamental limitation in the stability performance of the design, which will be explained in further detail.

5.2.2 Interferometer

The interferometer fringe is shown in Fig. 5.5 for a $T = 4.1$ ms interferometer. We construct this figure by scanning the phase of the RF oscillator for the Raman EOM just before the final pulse. We achieved an interferometer contrast of 20%. This fringe includes the components from Earth gravity and rotation. We note that the gravitational phase shift is opposite for each interferometer, due to the

reversed $\mathbf{k}_{\text{eff}}$ vector. Thus, it is possible to set an arbitrary relative phase between the interferometers with appropriate choice of interrogation time T. This allows us to choose a phase ϕ such that both interferometers are mid-fringe. As shown in the figure, we choose a T such that there is a relative π phase between the interferometers. Furthermore, we find that this rejects detection noise in the rotation component of the signal.

We set the interferometers to mid-fringe and monitor the noise in the signal over 60 seconds. We find the phase noise of each interferometer to be $\delta\phi_a = \delta\phi_b = 22$ mrad/shot. The corresponding acceleration and rotation rate components of the phase noise are $\delta\phi_- = 19$ mrad/shot and $\delta\phi_+ = 11$ mrad/shot. The acceleration component of the phase is noisier by a factor of 2 due to vibrations of the retro-reflecting mirror. The resulting acceleration and rotation rate sensitivities are 0.9 $\mu g/\sqrt{\text{Hz}}$ and 1.1 $\mu\text{rad/s}/\sqrt{\text{Hz}}$, which represent competitive figures for inertial navigation.

It is worth noting the potential performance of this approach under optimal conditions. Let us assume a shot noise limited signal on the 4×10^6 atoms we achieved, with 100% fringe contrast. The corresponding phase noise is 0.5 mrad per interferometer. Using an identical interrogation time and bandwidth, we find optimal sensitivities of 33 n$g/\sqrt{\text{Hz}}$ and 70 nrad/s$/\sqrt{\text{Hz}}$. While the estimates of shot noise limited sensitivity and maximal fringe contrast may be overzealous, we believe a sensor achieving 100 n$g/\sqrt{\text{Hz}}$ and 100 nrad/s$/\sqrt{\text{Hz}}$ is feasible.

5.2.3 Noise Analysis

To account for sources of noise in our experiment, we conduct an investigation of a microwave interferometer and Doppler-sensitive Raman interferometer with ultra-short interrogation time $T = 10$ μs. This eliminates many of the systematic effects such as magnetic field gradient and high Doppler-sensitivity. The results are shown in Fig. 5.6. We find the contrast of the microwave interferometer is much higher,

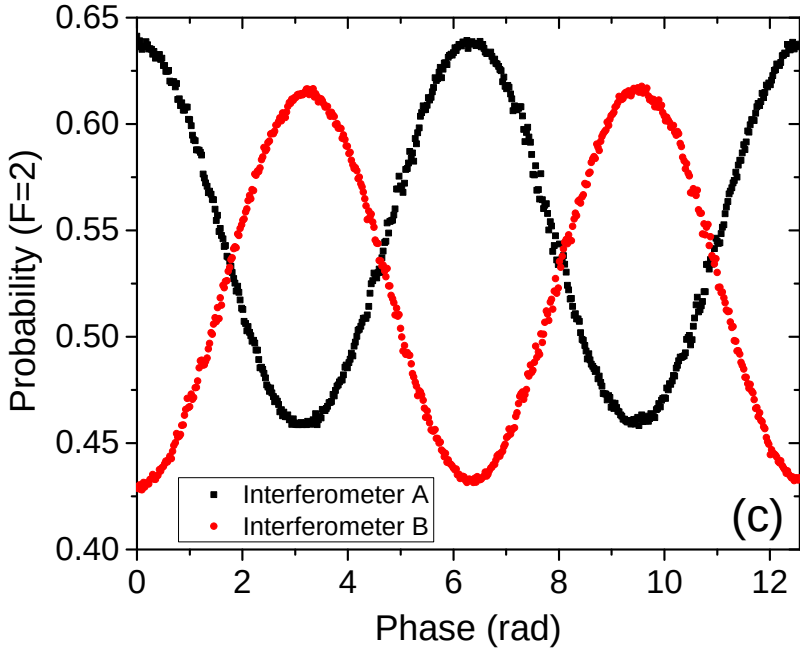

Figure 5.5: Interferometer fringes. We measure a fringe contrast of approximately 20%. We find that by tuning T to set a π phase shift between the interferometers, we may reject detection noise in the rotation signal. Figure reprinted from [59].

again indicating the limited pulse efficiency of the Raman transition. The phase noise of the microwave interferometer is $\delta\phi = 3.3$ mrad/shot. The phase noise of the Raman interferometer is $\delta\phi = 9.6$ mrad/shot. We find the signal noise of the interferometers to be comparable, at 1.15×10^{-3} per shot and 1.36×10^{-3} per shot for the microwave and Raman interferometer, respectively. This indicates that the noise of the interferometers derives primarily from background detection noise, rather than any sources of phase noise. The detection background noise overwhelms the total noise in the Raman interferometer, due to reduced fringe contrast. Furthermore, we find the Raman interferometer noise to be comparable to that of the rotational component of the phase noise. This again indicates the contribution of vibrational noise on the acceleration component of the signal. We find increasing the interrogation time adds a negligible amount of noise after accounting for the reduced fringe contrast.

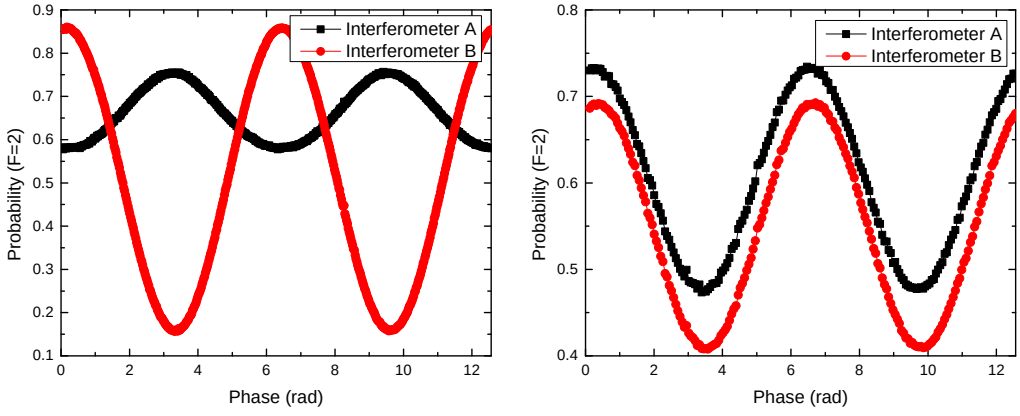

Figure 5.6: Microwave and Raman interferometers with ultra-short interrogation time $T = 10$ μs. Left: Microwave interferometer with 70% fringe contrast. The spatial separation of the ensembles results in a substantial difference in Rabi frequency. The interferometer was optimized to favor interferometer B. Right: Raman interferometer with 28% fringe contrast.

Thus, we determine the primary source of noise in our system stems from reduced fringe contrast and detection noise. As discussed previously, the population transfer efficiency is limited is limited by ensemble spatial distribution and ensemble temperature. Furthermore, selecting an intermediate resonance frequency for the second and third pulses further reduces population transfer efficiency. A combination of these effects results in a reduced fringe contrast of 20%. Accounting for the fraction of the ensemble imaged, 1×10^6 atoms contribute to the noise while 2×10^5 contribute to the signal. This represents a non-inertial phase noise of 5 mrad per interferometer. We find the electronic noise, background scatter, and photon shot noise to be below 0.1 mrad, and thus are negligible. We thus attribute the remainder of the noise to frequency and intensity noise of the probe.

Improving this fringe contrast would immediately represent a higher sensitivity, as the apparatus is not phase-noise limited. One possibility is the use of composite pulses. A composite pulse refers to a sequence of a small number of pulses which act analogous to a π or $\pi/2$ pulse, but with enhanced robustness to field strength and

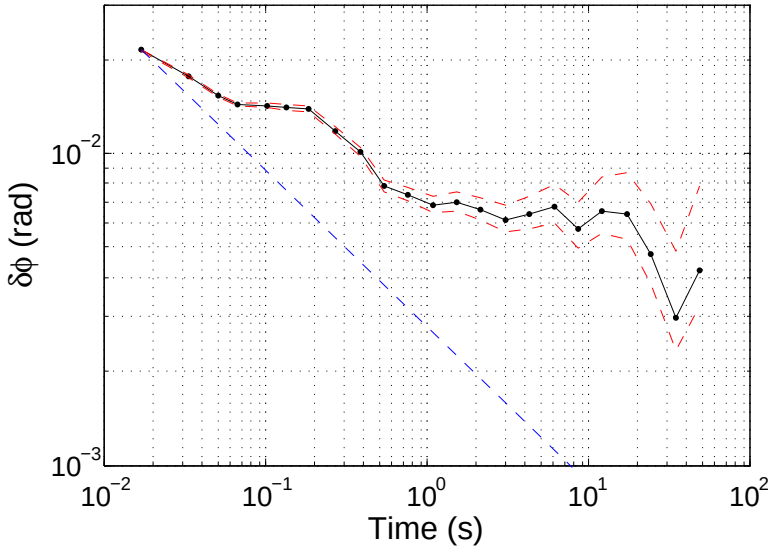

Figure 5.7: Allan deviation of the interferometer phase. We find a stability floor of approximately 3 mrad.

detuning. These have been employed since early NMR based systems [82]. Recent work [83, 84, 85] demonstrates successful application of composite pulse techniques towards atom interferometry.

5.3 Stability

Throughout the experiment, achieving long-term stability remained elusive. We believe the technical challenges associated with achieving long-term stability have been demonstrated in other systems, and do not limit the potential of our technique towards a fieldable device. Nevertheless, we present an analysis of the sources of systematic error in our experiment.

A plot of the Allan deviation of the interferometer phase is shown in Fig. 5.7. This plot was generated from a mid-fringe time record of the interferometer. We find these results to be fairly typical, with a stability floor of a few milliradians.

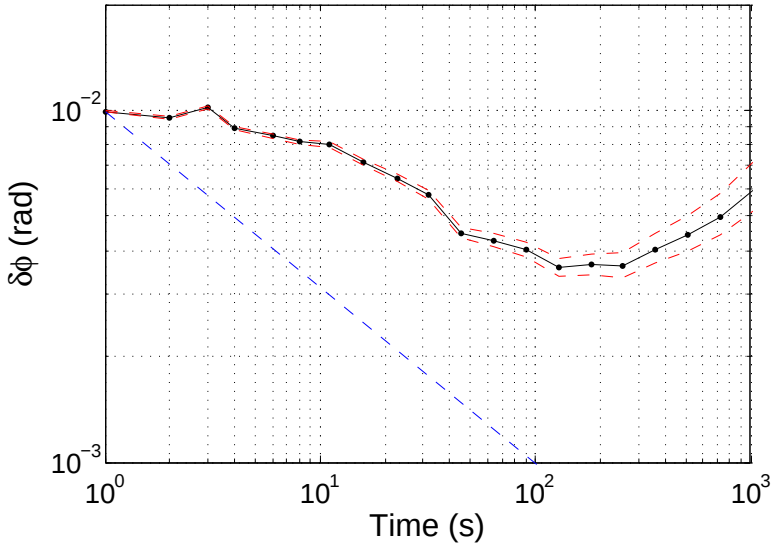

Figure 5.8: Allan deviation of the interferometer phase, rejecting detection noise errors. We sweep the interferometer fringe over 1 s and extract the phase by a fit. The noise floor is approximately 3 mrad.

Our first assumption was that our detection method was unstable. Uncertainties in the arrival time and position of the ensemble result in a systematic error of the population readout. This in turn results in a systematic error in the readout of the interferometric phase. To mitigate this, we sweep the interferometer fringe over 1 s and fit the resulting sine wave. The fringe offset and contrast should mirror any detection readout error, and enable us to make a precise readout of the phase. An Allan deviation of those results is shown in Fig. 5.8. We again observe a similar noise floor of a few milliradians. This suggests that there is indeed a systematic phase error, independent of detection noise.

To simplify our analysis, we conducted an investigation of the stability of a microwave interferometer. This will allow us to determine if the systematic error is a consequence of clock stability or something specific to the Raman transition. However, we first demonstrate a phase readout algorithm robust against detection errors.

5.3.1 Fringe-Compensation Algorithm

We seek to make the interferometer robust against systematic long-term instabilities involving the ensemble exchange and detection. Fortunately, the ensemble exchange operates at a rate greater than the timescale for many of this systematic effects. In this section, we describe an algorithm we use to dynamically scan the fringe and mitigate many of these systematics.

The naive method is to simply scan the entire fringe rapidly with respect to the drift timescale. This allows us to correct errors in the mid-fringe offset and fringe amplitude. However, this comes with a loss of sensitivity as the interferometer passes the top and bottom of the fringe. Averaging the sensitivity over the fringe, we have

$$\delta\phi_{\text{avg}} = \frac{\delta\phi}{2\pi}\int_0^{2\pi} |\cos(\phi)|\mathrm{d}\phi = \frac{2}{\pi}\delta\phi. \tag{5.2}$$

Thus, we find that we lose approximately 40% of our sensitivity. We may mitigate this by only scanning points close to the middle of the fringe, thus maintaining maximal phase sensitivity. Suppose we were to scan the points $\delta\phi$, $-\delta\phi$, $\pi-\delta\phi$, $\pi+\delta\phi$, where $\delta\phi < \pi/2$. We assume our signal $s(t)$ is governed by a slowly varying amplitude $a(t)$, offset $c(t)$, and phase $\phi(t)$. Thus, we have

$$s(t,\phi') = a(t)\sin(\phi(t)+\phi') + c(t), \tag{5.3}$$

where $\phi(t)$ is our true signal and $\phi' = [\delta\phi, -\delta\phi, \pi-\delta\phi, \pi+\delta\phi]$. Let s_1, s_2, s_3, s_4 represent a successive data points through this scan. We then find that we can cancel the slowly varying fringe and offset as follows.

$$A = \left[\left(\frac{s_1+s_2}{2}\right) - \left(\frac{s_3-s_4}{2}\right)\right]/(2\cos(\Delta\phi)), \tag{5.4}$$

$$B = (s_3-s_4)/(2\sin(\delta\phi)), \tag{5.5}$$

$$\phi = \arctan(A/B). \tag{5.6}$$

A simulation of this algorithm is shown in Fig. 5.9. The simulated data assumes a white noise background phase with varying amplitude and fringe offset. The direct

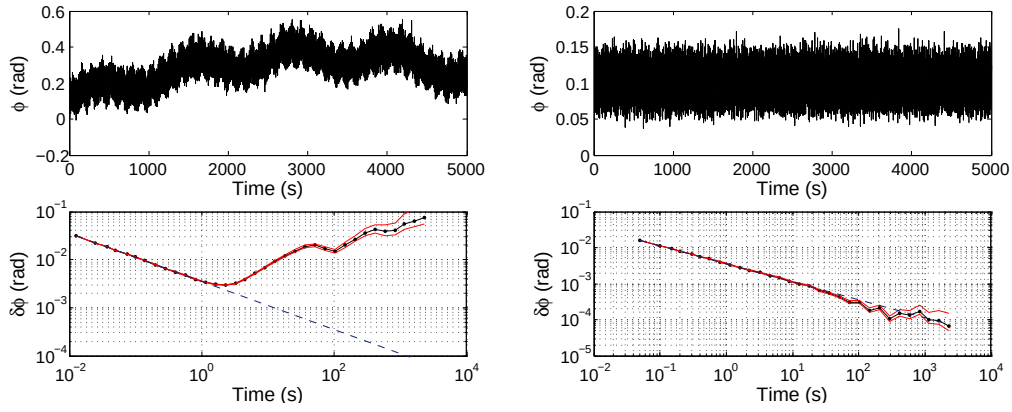

Figure 5.9: Simulation of the fringe-scanning algorithm. Left: Tracking the phase by sitting mid-fringe. The Right: Correcting the fringe with $\pi/8$ phase modulation.

calculation which sits mid-fringe and assumes constant contrast and offset is shown on the left. The Allan-deviation corresponding to this data is qualitatively similar to the results we observe, with the phase starting to wander from $1 - 10$ s. The data on the right implements this algorithm with a phase modulation $\delta\phi = \pi/8$. While this cuts down the data rate by a factor of 4, we see the algorithm successfully maintains fringe stability up to 1000 s. It is possibly to modify this algorithm by maintaining a memory of previous fringe amplitudes and offsets and maintaining a running, weighted average. This would enable calculation of the interferometer phase with each data point, maintaining the original data rate.

We note that this algorithm only corrects for systematic errors in the amplitude and offset which are uncorrelated with ϕ, such as detection. It is possible that a change in fringe contrast is due to a shift in resonance frequency, which would result in a systematic phase. In fact, analysis of the systematic noise sources in our experiment indicate this to be the case.

Using this algorithm, we investigate the stability of a microwave clock. We find the algorithm is effective in enhancing the noise floor past the detection-limited stability. The result is shown in Fig. 5.10. We find a noise floor of 6×10^{-5} rad, which

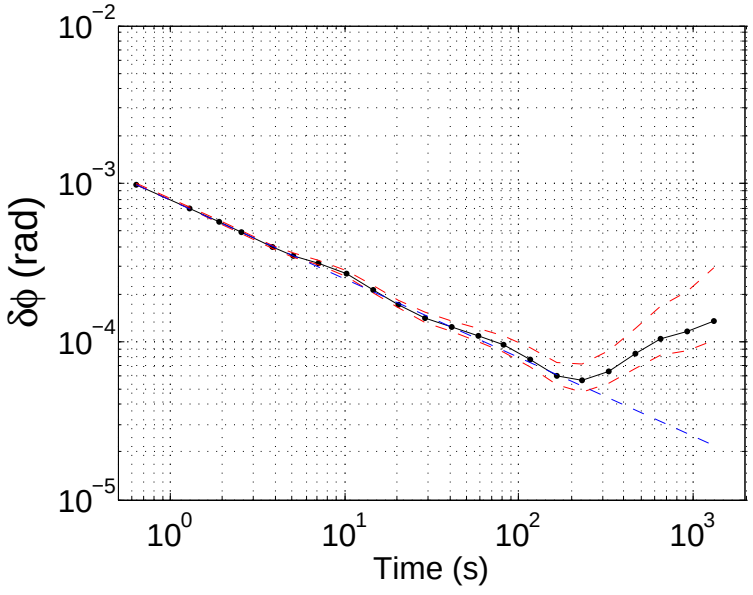

Figure 5.10: Allan deviation of the microwave interferometer phase. The noise floor rests below 10^{-4}.

is far below the noise floor of the Doppler-sensitive interferometer. This suggests that the atom interferometer noise floor is technical in nature, rather than fundamental.

5.3.2 Off-Resonant Pulses

We present an analysis on the effect of off-resonant Raman pulses on the interferometer phase. While resonant pulses are robust against variations in pulse duration and intensity (i.e. second order sensitivity), such is not the case with off-resonant pulses [86].

For simplicity, we will consider an off-resonant microwave pulse on a two-level atom. This enables us to ignore the effects of ensemble spatial and velocity distribution. In the case of a Raman pulse, we would have to integrate over these quantities. Nevertheless, we find this analysis to be illuminating in understanding sources of long-term instability in the atom interferometer.

Let $\hat{H}$ be the Hamiltonian for the two level atom,

$$\hat{H} = -\frac{\hbar\delta}{2}\hat{\sigma}_z + \frac{\hbar\Omega_0}{2}\hat{\sigma}_x, \tag{5.7}$$

where Ω_0 is the Rabi frequency and δ is the detuning. The corresponding time-evolution operator $\hat{U}(t,\phi)$ with phase ϕ is given by,

$$\hat{U}(t,\phi) = e^{-i\hat{H}t/\hbar}e^{-i\phi\hat{\sigma}_z}. \tag{5.8}$$

We construct the interferometer with our $\pi/2-\pi-\pi/2$ pulse sequence and scanning the phase of the third pulse,

$$p_g = \left|\langle g|\,\hat{U}(\pi/2,\phi)\hat{U}(\pi,0)\hat{U}(\pi/2,0)\,|g\rangle\right|^2, \tag{5.9}$$

where we expressed time in units of $1/\Omega_0$, such that $\Omega = \Omega_0/t$. This expression has components which are in-phase and in-quadrature with the applied oscillator phase ϕ. We calculate the total phase with respect to this offset and find a systematic phase shift given by

$$\Delta\phi = \cot^{-1}\left(\frac{3}{2\Omega}\sqrt{\frac{1}{\delta^2}+\frac{1}{\Omega^2}}\frac{\delta^2+\Omega^2\cos^2(\theta/2)}{\sin(\theta)+2\cos(\theta/4)\sin(\theta/2)}\right), \tag{5.10}$$

where $\theta = (1/\Omega_0)\sqrt{\Omega^2+\delta^2}$. Defining $\Delta\Omega = \Omega - \Omega_0$ and expanding this expression to first order in δ and $\Delta\Omega$, we find the approximation

$$\Delta\phi = \frac{2}{3}\frac{\delta}{\Omega_0}\frac{\Delta\Omega}{\Omega_0}. \tag{5.11}$$

Thus, the combination of a frequency shift with Rabi frequency variation results in a first-order systematic shift on the interferometer phase. To investigate this systematic phase shift, we carried out this experiment using microwave pulses on our apparatus. The microwave intensity and detuning were scanned by approximately $\pm 0.1\Omega_0$ near resonance. Results of the experiment are shown in Fig. 5.11. Red dots correspond to measured data points, while the plotted function is Eq. 5.10 with no free parameters. The experiment reveals the model to accurately describe sources of

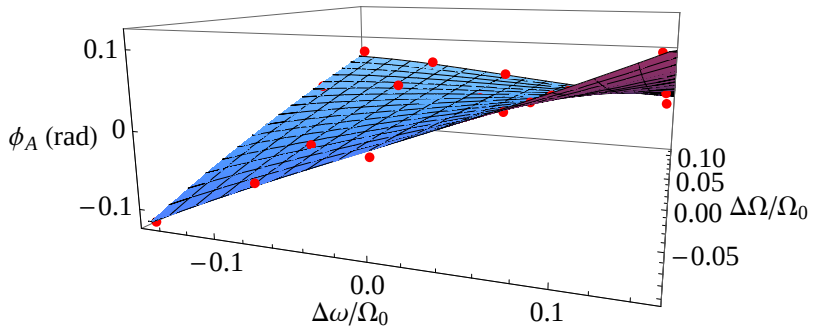

Figure 5.11: Demonstration of systematic phase shift with off-resonant pulses. Red data points are experimental data from the phase of a microwave interferometer as a function of detuning and Rabi frequency error. The surface is a plot of Eq. 5.10 with no free parameters.

systematic phase errors. The deviation from the function is within the stability of the fringe, as limited by Rabi frequency.

This analysis has revealed a limitation of the apparatus, suggesting an avenue for further development. While we may tune the first and third pulses to resonance with the upgraded two Raman beam system, the second (middle) pulse must be shared by the two interferometers. Thus, this pulse will always be driven off-resonantly. This causes variations in Raman beam intensity to result in a systematic phase shift. While it may be possible to servo the intensity of this beam, this comes at the cost of increased system complexity. Furthermore, the ultimate stability of the apparatus will be tied to the stability floor of this laser beam.

5.3.3 Differential AC Stark shift stability

The AC Stark shift, also known as the light shift, is a change in the atomic energy levels due to the presence of a time-varying (AC) electric field, typically due to a laser. For a far off-resonant laser, the atomic energy levels shift by $\Omega^2/(4\Delta)$. With our two Raman lasers, the shift to the hyperfine ground states have the same sign. However, there is a residual energy difference known as the differential AC Stark

shift, which is given by $(\Omega_1^2 - \Omega_2^2)/(4\Delta)$. Traditionally, this shift is nullified by tuning $\Omega_1 = \Omega_2$. In our experiment, we achieve this by tuning the RF power delivered to the Raman EOMs, thus changing the relative power between the carrier and sideband. To calculate the differential light shift δ_{AC}, we note that the two resonances observed in Fig. 5.4 are derived from $\delta_{\pm} = \delta_{\mathrm{AC}} \pm \mathbf{k}_{\mathrm{eff}} \cdot \mathbf{v}$. Thus, the differential light shift is revealed by the average of these two resonances.

We thus conduct a measurement of the stability of this frequency shift. We monitor the resonance conditions for the Raman transition as a function of time. The differential light shift is revealed by the average of the resonances corresponding to $+\mathbf{k}_{\mathrm{eff}}$ and $-\mathbf{k}_{\mathrm{eff}}$. A plot of the light shift as a function of time is shown in Fig. 5.12 for each of the interferometers. We see a substantial change in the resonance condition as a function of time. The differential light shift varies by 40 kHz on a timescale of a few minutes. We recall that the Rabi frequencies typically differ between the interferometers. We choose an intermediary Rabi frequency, which results in an error of a couple percent. Thus, from Eq. 5.11 we find this light shift in conjunction with Rabi frequency error is sufficient to account for the observed fringe stability. We note that the shifts are highly correlated between the interferometers, indicating the source of the instability to be common mode.

To further investigate the instability of the differential AC stark shift, we investigate the output of the EOM. The EOM we use is a Photline 800 nm band 10 GHz phase modulator (NIR-MPX800-LN-10). We assume the light field of the input laser beam is given by $Ae^{i\omega t}$. The phase of this expression is modulated by the input RF field with modulation depth β and frequency Ω. The output of the EOM is given by [87],

$$Ae^{i(\omega t + \beta \sin(\Omega t)} = Ae^{i\omega t}\left(J_0(\beta) + \sum_{k=1}^{\infty} J_k(\beta)e^{ik\Omega t} + \sum_{k=1}^{\infty}(-1)^k J_k(\beta)e^{-ik\Omega t}\right), \quad (5.12)$$

where we applied the Jacobi-Anger identity [88] and $J_k(\beta)$ is the Bessel function of the first kind. This expression represents sidebands which vary from the carrier wave

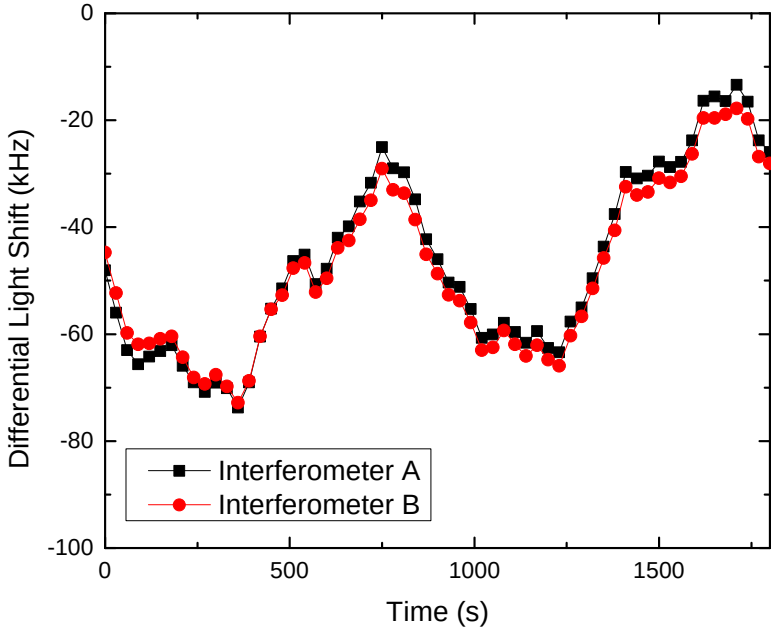

Figure 5.12: Differential light shift of each interferometer as a function of time. The light shift varies as a function of time by approximately 40 kHz every few minutes. The lights shifts of the two interferometers are well correlated, indicating the instability to be common to both interferometers.

by a frequency Ω and with amplitudes given by the Bessel functions. The modulation depth β is proportional to the applied RF power. We typically tune β such that the amplitudes of the zero and first-order sidebands are approximately equal. We achieve fine tuning in this by minimizing the differential light shift in the experiment. Thus, the ratio of the amplitude of the two laser frequencies is governed by the stability of the RF source. We find this source to be stable to a level of 10^{-4}, which does not explain the observed differential light shift instability.

We thus seek to measure the optical sideband amplitude stability directly. The most direct way of observing this is to monitor the sideband intensity in a FabryProt cavity. However, we find this measurement to be imprecise beyond fluctuations on the order of 1%. This is limited by the stability of the cavity. We thus seek an alternative method of measurement. One possibility is to monitor the light on a fast

photodiode and measure the beatnote between the sidebands. However, as shown in Eq. 5.12, the sidebands have opposite phase with respect to the opposing sideband (for example, the +1 sideband with respect to the −1 sideband). This results in destructive interference so that no beatnote is observed.

We conducted this measurement with the light out of the EOM, and found a minimal beatnote at the hyperfine frequency indicating the two sideband amplitudes to be equal to within a level of 0.1%. However, in the experiment the light out of the EOM is directed towards a tapered amplifier. The amplifier has a gain profile over which some sidebands are amplified with different gains. A variation in this gain profile over time would cause the relative sideband amplitudes to fluctuate, resulting in an unstable differential light shift. We thus repeated this measurement using light out of the TA, and found a sideband amplitude mismatch as large as 10%. This does indeed indicate that the TA gain profile selectively amplifies different sidebands. Furthermore, by monitoring the beatnote amplitude over time, we find that over the course of several minutes the amplitude varies on the order of a few percent. When compared with the Rabi frequency of $2\pi \times 300$ kHz, this variation corresponds to a differential AC stark shift of ten kilohertz. This is in qualitative agreement with the observed drift in the differential light shift from Fig. 5.12. Despite the lack of sufficient resources to conclude this analysis, we have provided strong evidence for the source of our interferometer instability.

There are many methods by which we may correct for this source of instability. The first method involves interlacing shots of the Doppler-sensitive interferometer with a Doppler-free interferometer. From the Doppler-free interferometer, we find the systematic phase shift independent of inertial conditions which we may use to correct the Doppler-sensitive interferometer. However, the polarization of the Raman beams is configured to suppress the Doppler-free transition. This would require an upgrade to the Raman beam module to dynamically switch the polarization of the light; for example, with a Pockels Cell. Furthermore, the software control system would

require significant upgrades to support this measurement and feedback. While data-rate operation would support such a solution by increasing the number of interlaced Doppler-free scans, this comes at the cost of a reduced number of Doppler-sensitive scans and thus a reduction in sensitivity. Another solution involves re-engineering the Raman laser system. One such system involves two independent lasers for each frequency, combined and phase-locked on a common optical path. This enables the intensity of each laser to be locked independently, ensuring a stable differential light shift. The combination of the lasers results in a significant loss of optical power, which may be recovered through the use of high power lasers [89].

Chapter 6

Dual-Axis Sensor Dynamics

We now seek to demonstrate the aspects that make our interferometer unique, namely robustness against dynamic inertial environments. We do so in three parts. First, we consider the current dynamic performance of the device as measured with the capabilities we have in the laboratory, and demonstrates that this far exceeds typical atom interferometer performance. Along with this, we consider the potential performance of the ensemble-exchange approach in terms of providing a robust flux of ultracold atoms. We then consider the device as an open-loop interferometer whereby auxiliary sensors provide information on which fringe the interferometer is operating, providing a means of enhancing the dynamic range. Finally, we demonstrate our implementation of a closed-loop sensor which should enable the interferometer to function as a fieldable device.

6.1 Demonstrations

A demonstration of the interferometer's sensitivity to acceleration and rotation is shown in Fig. 6.1. The first plot shows the interferometer outputs, while the second decouples these into acceleration and rotation rate components. We generated two

oscillations by pushing the optical table, restricting the magnitude to remain within one fringe. The first oscillation is generated by applying a force near the center of mass of the table, in an attempt to minimize the applied rotation. Indeed we observe the acceleration signal and a minimal rotation rate. The data-rate of the apparatus is high enough to capture dynamics of interest. The second oscillation corresponds to applying a force away from the table center of mass orthogonal to the direction of rotation sensitivity. This generates a small rotation about this axis which is seen in the figure. A residual acceleration signal is present, as the apparatus is not perfectly situated on the table center of mass, and thus a residual acceleration is present. The magnitude of force required for this demonstration is minimal. Indeed, to maintain the interferometer within one fringe for this oscillation frequency of 3 Hz, the optical table moves by a mere 30 μm. We will revisit the issue of dynamic range later in the chapter.

As a second demonstration, we compared the output of the interferometer with a seismic sensor (Kinemetrics EpiSensor ES-T) and gyroscope (ARS 16). These results are shown in Fig. 6.2. Calibration errors in the contrast of the interferometer fringe result in higher errors at larger accelerations and rotations. A residual delay between the interferometer and gyroscope is the subject of investigation. Nevertheless, this comparison increased our confidence in the accuracy of the sensor, and motivated the use of auxiliary consensors as will be described in Sec. 6.5.

Finally, we would like to note that these sensors are both AC coupled, and thus are not sensitive to slower DC accelerations and rotations. We have previously demonstrated sensitivity to DC accelerations from the absolute gravimeter in the high data-rate accelerometer. To demonstrate the DC rotation sensitivity of the apparatus, we carry out a measurement of the Earth's rotation rate [32]. To carry out this measurement, we rotate the apparatus in the $\hat{\mathbf{z}}$ direction by use of a turn table. This changes the projection of the Earth's rotation vector along the rotation measurement axis, $\hat{y}$. By measuring the rotation rate component of the interferometer

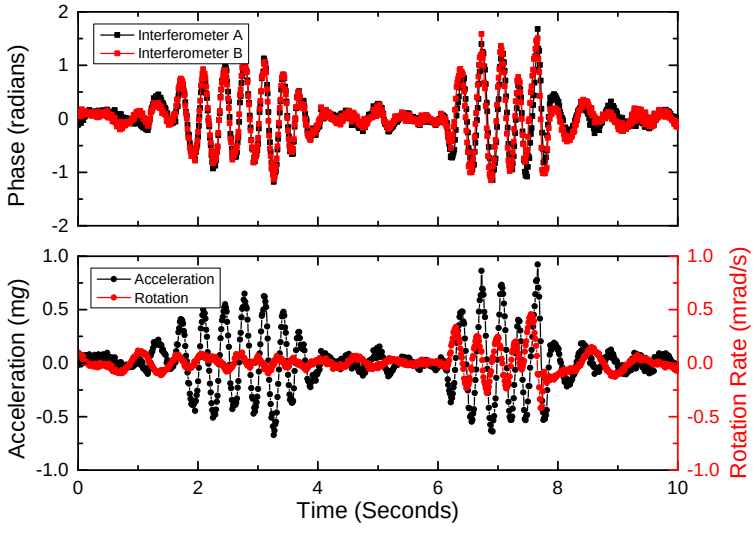

Figure 6.1: Demonstration of acceleration and gyroscopic sensitivity of the interferometer. Top: Phase readout of each interferometer. Bottom: Decoupled acceleration and rotation signals. The first oscillation corresponds to an induced acceleration, while the second is an induced rotation with residual acceleration. The amplitude of the impulses is restricted to one fringe.

fringe as a function of the rotation angle θ_z, we may fit to the amplitude sweeping the full range of projections. With knowledge of our latitude, we may deduce the Earth's rotation rate.

Constraints in the length of fibers and electronic cables supplying the sensor head limit the angle of rotation to $\pm 60°$. Nevertheless, we carried out the experiment and found this range to be sufficient. We scan the fringe at each angle to achieve an accurate measurement of the phase independent of detection drift. Results are shown in Fig. 6.3. The fit reveals a rotation rate of 57 ± 5 μrad/s, which in conjunction with our latitude (35.1° for Albuquerque) reveals one sidereal day to be 25 ± 2 Hours. We would like to note that this was not intended to be a precision measurement of the Earth's rotation rate, but rather a demonstration of the DC rotation sensitivity of the device.

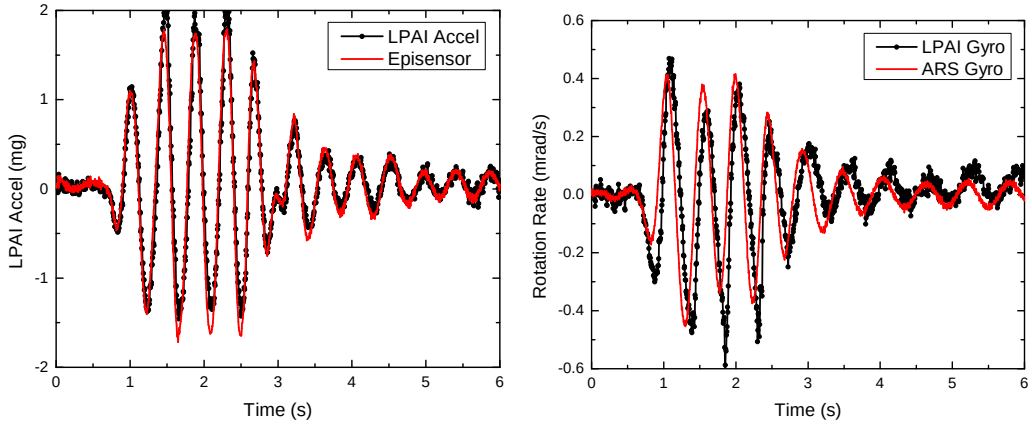

Figure 6.2: Comparison of the interferometer with commercial accelerometer and gyroscope. The amplitude of the impulses is restricted to one fringe. We find excellent agreement to the commercial accelerometer. There is a systematic delay between the interferometer and gyroscope of approximately 10 ms.

6.2 Observed Dynamic Performance

We evaluate the dynamic performance of our apparatus given the range of inertial conditions we may apply in our laboratory. A more rigorous testing platform would be necessary to exceed these limitations.

6.2.1 Tilt Test

Gravitational acceleration in conventional atom interferometers with $T \approx 100$ ms displaces the atomic ensemble by tens of centimeters. Thus, they are designed accounting for a fixed orientation of gravity. Given an arbitrary orientation of gravity, the apparatus will not function due to excessive displacement. The strength of our apparatus is that the short time-of-flight minimizes the deflection, and allows the apparatus to operate in any orientation. Furthermore, it is likely the apparatus can withstand accelerations beyond this range.

To demonstrate the immunity to orientation, we ran the interferometer while

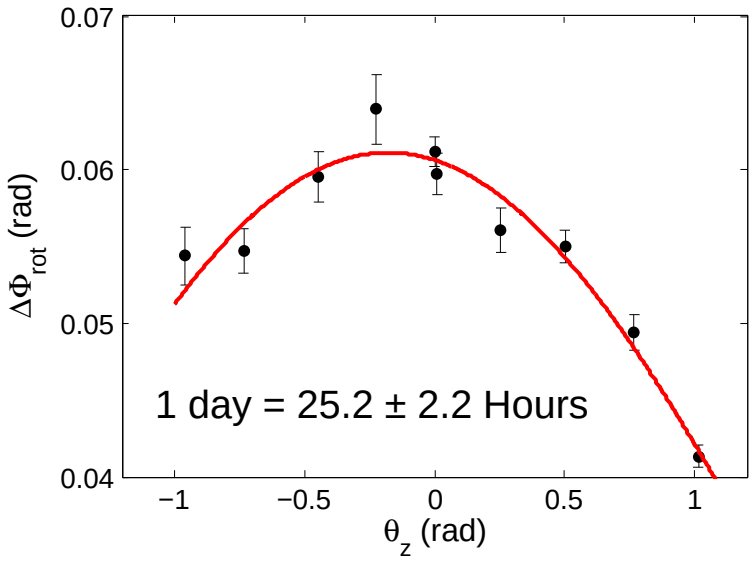

Figure 6.3: Measurement of the earth's rotation rate. We measure the rotational component of the interferometer phase as a function of orientation angle θ_z. This changes the propagation of the Earth's rotation axis on the interferometer rotation measurement direction. By fitting this to a cosine, the amplitude reveal a rotation rate of 57 ± 5 rad/s. The reduced ξ^2 of the fit is 1.16.

varying the orientation of the apparatus over a range of angles in the plane defined by $\mathbf{v}$ and $\mathbf{k}_{\text{eff}}$. This changes the projection of gravity on both the launch velocity and the Raman wavevector. We oriented the apparatus using hinges attached below the base of the apparatus (outside the magnetic shielding) while a winch bore the weight. The angle was measured with respect to gravity, using a Bosch Sensortec BMA150 accelerometer, ranging from 0° to 65°. We plot the fringe contrast and atom number as a function of this angle in Fig. 6.5. To within the measurement uncertainty, the fringe contrast and atom number remain unchanged up to a 65° tilt. This measurement uncertainty is limited by the typical drift in the contrast and atom number over the 1 hour timescale the experiment took place. This demonstrates robustness up to at least 1 g and likely beyond.

Figure 6.4: Picture of the interferometer subjected to variations in the orientation of gravity. A winch bears the approximately 100 kg load of the apparatus as it is secured. Not shown: One incredibly nervous graduate student.

6.2.2 Rotation Rate Limit

We note that the ensemble velocity distribution contributes an inhomogeneous interferometer phase shift in Eq. 2.18. This causes a phase gradient across the ensemble, the magnitude of which is proportional to rotation rate $\mathbf{\Omega}$. This gradient is averaged across the ensemble, and results in a systematic phase shift and contrast loss as a function of $\mathbf{\Omega}$. The systematic phase can be corrected by knowledge of the ensemble temperature and use of an auxiliary sensor. However, resolving the contrast loss is more difficult. We present an analysis and measurement of this contrast loss, as well as potential solutions to mitigating this effect.

Let ϕ_0 be the inertial phase shift we intend to measure. There is an additional phase from the atomic velocity with respect to the mean ensemble velocity, given by $\phi' = 2k_{\text{eff}} v' \Omega T^2 \sin(\theta)$, where θ is the angle between the $\mathbf{\Omega}$ and $\mathbf{k}_{\text{eff}}$. Integrating the

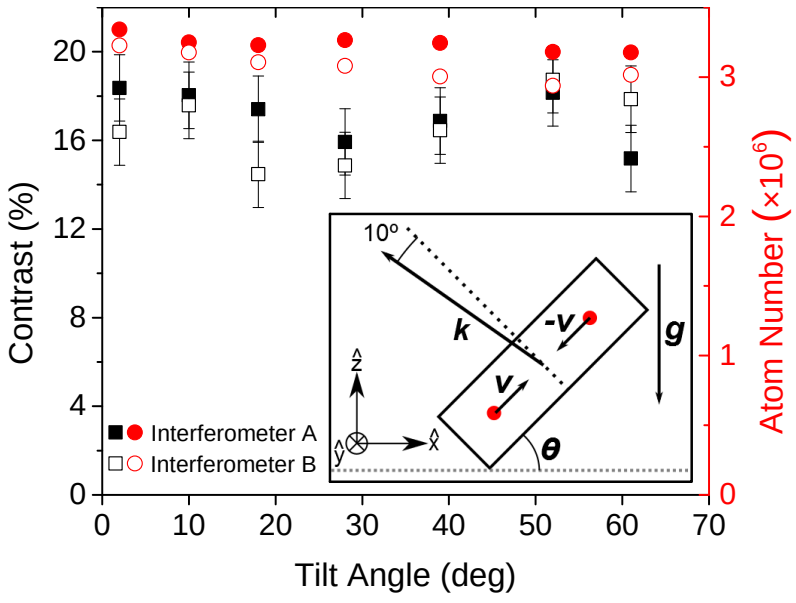

Figure 6.5: Immunity of the atom interferometer to orientation with respect to gravity. We plot the interferometer contrast and atom number as a function of orientation angle, θ_6. This changes the projection of gravity on both the Raman wavevector $\mathbf{k}_{\text{eff}}$ and launch direction $\mathbf{v}$. Error bars represent the typical long term drift over the 1 hr which this experiment took place. Figure reprinted from [59].

interferometer signal over the ensemble velocity distribution,

$$
\begin{aligned}
s(\phi) &= \int_{-\infty}^{\infty} \sin(\phi_0 + \phi') g_v(v') \mathrm{d}v' && (6.1)\\
&= A \sin(\phi) + B \cos(\phi), && (6.2)\\
A &= \int_{-\infty}^{\infty} \cos(2k_{\text{eff}} v' \Omega T^2) g_v(v') \mathrm{d}v', && (6.3)\\
B &= \int_{-\infty}^{\infty} \sin(2k_{\text{eff}} v' \Omega T^2) g_v(v') \mathrm{d}v', && (6.4)
\end{aligned}
$$

where the coefficients A and B represent the signals in phase and in quadrature with the inertial signal. The total contrast is then given by $\chi = \sqrt{A^2 + B^2}$ and systematic phase shift $\tan(\delta\phi) = B/A$. These integrals are readily evaluated as the

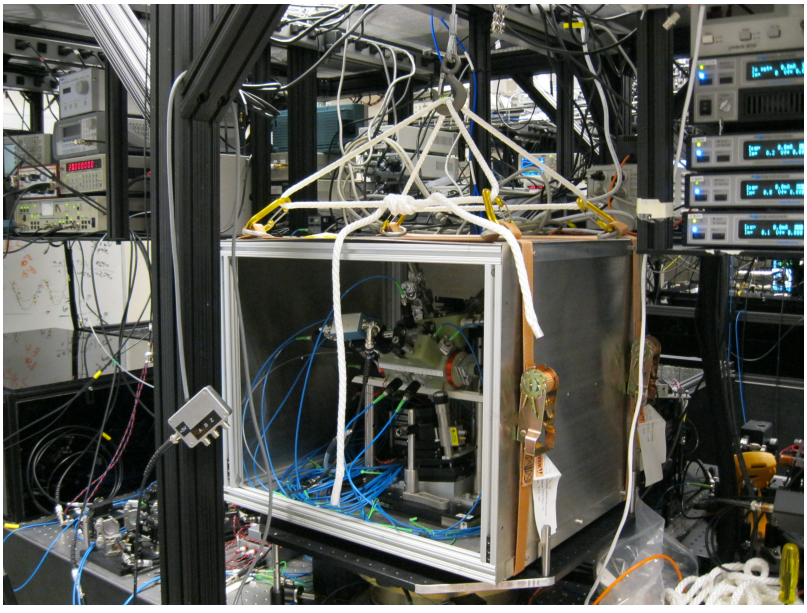

Figure 6.6: Picture of the interferometer mounted to a rotation table. A rotary encoder measures the rotation angle. The optical fiber and electric cabling restricts the range of movement to approximately ±60°. This was used in both the Earth rotation rate measurement and the rotation contrast loss investigation.

Fourier transforms of Gaussian functions. The contrast is then given by,

$$\chi = \exp(-\Omega^2/(2(\sigma_\Omega)^2)), \tag{6.5}$$

$$\sigma_\Omega = \frac{1}{2}\sqrt{\frac{m}{k\mathcal{T}}}\frac{1}{\sin\theta k_{\text{eff}}T^2}. \tag{6.6}$$

We carried out an experiment to measure this effect. The apparatus was placed on a 22 cm rotation platform located outside the magnetic shielding. We rotated the apparatus manually about $\pm\hat{\mathbf{g}}$ up to ±1.5 rad/s. This direction is offset from the Raman wavevector by $\theta = 10°$. While the platform had to be rotated manually over a small range, the high data rate of the apparatus enabled us to scan the fringe amplitude in a tenth of a second. Thus, despite manual rotation the rate was relatively constant over this interval. Fig. 6.7 shows the fringe amplitude as a function of rotation rate. As expected, the loss is Gaussian with respect to Ω.

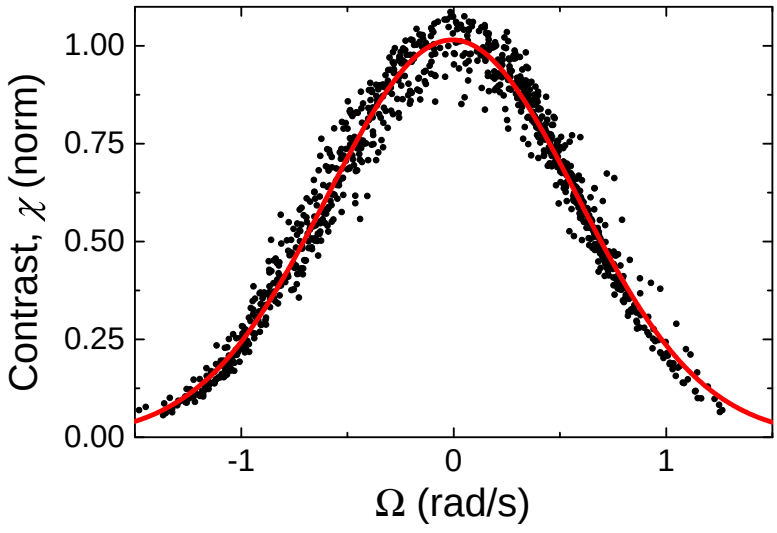

Figure 6.7: Contrast loss under high rotation rate. The interferometer fringe is scanned rapidly (2π radians over 100 ms) and the normalized contrast (black dots) is plot as a function of rotation rate. The red line is a Gaussian fit with a width of $\sigma = 0.60(1)$ rad/s. Figure reprinted from [59].

The width $\sigma_\Omega = 0.60(1)$ rad/s corresponds to a temperature of 36 μK, which is in agreement with independent temperature measurements. We note that by Eq. 6.6, the contrast loss is most severe with $\theta = 90°$, in a direction perpendicular to $\mathbf{k}_{\text{eff}}$. This would cause the contrast to vanish $\sin(90°)/\sin(10°) \approx 6$ times faster.

This limit may be extended by a couple methods. First, the ensemble may be cooled more efficiently reducing the velocity spread. However, as shown in Eq. 6.6 the contrast loss scales as $\sqrt{1/\mathcal{T}}$. Thus, even cooling to a value of $\mathcal{T} = 5$ μK (approximate limit for many cold atom experiments with polarization gradient cooling), we would only expect the rotation range to increase by a factor of 2.7. Another solution involves placing the apparatus on gimbals. This has been employed in other inertial measurement units [37, 36]. However, this comes with the cost of increased system size and complexity.

We now note that although the ensemble contrast is diminished, the individual

atoms still maintain phase coherence and inertial purity. If the ensemble meets the condition $2T\sigma_v \gg \sigma_{x_0}$, where σ_{x_0} is the initial spatial width, at the end of the interferometer the position of each atom corresponds strongly with its velocity. Thus, the phase gradient becomes a function of position. The inertial information for each velocity class may then be retrieved with a sufficiently well-resolved detector [32, 90].

6.3 Atom Number Limitations

We now seek to observe the maximum acceleration and rotation rate the apparatus can endure. We do this in two parts. First, we consider just the ensemble exchange independent from the interferometer. We may think of this as estimating the limitation on the flux of available atoms, which sets an upper bound on interferometer performance. We will then consider the interferometer limitations separately. Unfortunately, there was no practical method for us to subject the apparatus to inertial forces exceeding 1 g of acceleration and 1 rad/s of rotation. Thus, we will seek to estimate these limitations by a variety of other methods.

6.3.1 Delayed Recapture

The first of these methods estimates the maximum overlap between ensemble position and trap position before significant recapture losses ensue. From this, we will calculate the acceleration and rotation rate necessary to replicate such a displacement from the trap center. We need a method to precisely control the position of the ensemble at the onset of recapture. One way to achieve this is to delay the recapture time so that the ensemble travels past the trap center. By scanning this delay time, we begin recapturing the MOT at different points along its trajectory, and thus at different locations relative to the trap center. One potential pitfall is that the ensemble has a significant velocity for this experiment due to the launch. However, the

launch velocity of 2.5 m/s is still well within the capture velocity $v_c \approx 4.7$ m/s and thus shouldn't significantly affect recapture probability. We measure the recapture efficiency similar to that of Fig. 5.2, where we measure the buildup of atom number over multiple shots of the experiment.

By scanning the recapture delays from -2 ms to 2 ms, we scan the ensemble position by 1 cm over the trapping region, as shown in Fig. 6.8. We note that by activating the trap early, the ensemble velocity carries it into the trap, and we observe our peak recapture efficiency of 82%. This is a consequence of the methodology we used to conduct the experiment. A true displacement of the ensemble in an orthogonal direction would be symmetric about zero delay, in a manner similar to a late activation (shown in the right half of the figure). Here, we see the high recapture efficiency is maintained until approximately 5 mm from the trap center. This is just shy of the beam waist for the cooling beams, as indicated by dashed lines on the plot. From this 5 mm number and our 10 ms time-of-flight, we may roughly estimate the maximal acceleration we may endure before recapture losses become significant. From calculating the kinematics, we find an acceleration of 10 g and rotation rate of 20 rad/s would be necessary to replicate this level of excursion. This demonstrates that ensemble exchange under our parameters provides a highly robust source of atoms. Currently the MOT capture volume is of the same order as the MOT beam waist. Ideally, we would have the MOT beams much larger than this capture volume to ensure sufficient saturation. Thus, it is possible this limit may be extended further by using larger MOT beams.

6.4 Open-Loop Interferometer Limitations

Thus far, we have demonstrated ensemble exchange to provide a high flux of atoms which is very robust against dynamic conditions. We have also demonstrated operation under large but *static* inertial conditions. We now consider the impact of

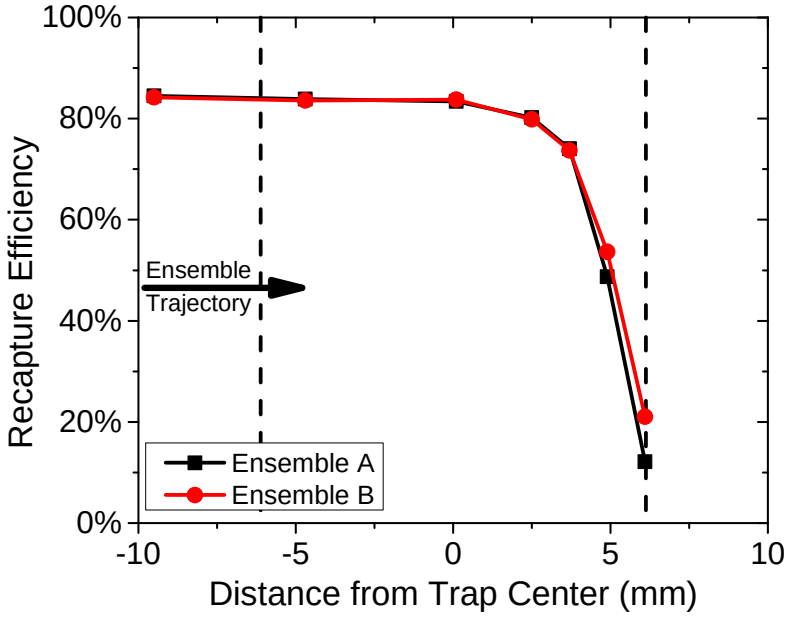

Figure 6.8: Recapture efficiency for various recapture delay times. With knowledge of the ensemble velocity, we map the delay times to a position. We find the recapture efficiency drops to 50% approximately 5 mm from the trap center. Figure reprinted from [59].

dynamic stimuli on the interferometer performance.

6.4.1 Dynamic Range

As a standalone, the sensor's dynamic range would be extremely limited. Indeed, the sensor would be limited to one fringe, with an amplitude of $\pm(\pi/2)/(k_{\text{eff}}T^2) = \pm 0.5$ mg and $\pm(\pi/2)/(2k_{\text{eff}}vT^2) = \pm 1.0$ mrad/s. This may be partially extended by using the interferometer output to feedback to the phase of the next shot. This would limit the change in acceleration (known as "jerk") and the angular acceleration to one fringe every shot of the interferometer. In practice, we found that even under a slow input acceleration at approximately 1 Hz, this technique only increased the dynamic range by a factor of 2 or 3.

Similar to atomic clocks, we may consider a system where the atomic sensor serves as a stable reference for a high bandwidth, locked sensor. In an open-loop configuration, the auxiliary sensors would identify the fringe the interferometer was operating, and the interferometer would provide an error with respect to that value. However, in this scenario the interferometer would operate at any location along the fringe. As shown previously in Eq. 5.2, the average sensitivity drops by approximately 40%. Furthermore, this may result in some ambiguity if the interferometer readout is near the top or bottom of a fringe.

6.5 Closed-Loop Interferometer

We present a closed loop system with feedback and feedforward mechanisms. In this design, the auxiliary sensors track the acceleration and rotation in real time during the ensemble ballistic trajectory. From this information, using their current bias and scale factor values, they feedforward the predicted mid-fringe phase to the interferometer. This keeps the interferometer locked near the center of the fringe, even for inertial conditions exceeding one fringe and rates greater than the time-of-flight. The interferometer measures the true phase, and then feedsback this information to the cosensors to adjust the bias and scale factors. While there has been work in this domain for vibration stabilization [91], a system designed for a dynamic signal has not been demonstrated.

There are a number of technical challenges to this approach. First of all, the cosensors must be sampled at a rate faster than the time of flight of the ensemble to ensure an accurate trajectory propagation. This corresponds to a rate of approximately 1 kHz. Secondly, the last sample must be as close as possible to the final pulse, and the resulting calculation and DDS update must occur with minimal delay. It is this limitation which will determine the final dynamic range of the system. Finally, the phase shifts for the two interferometers will be different and need to be

independently controlled. This requires updating the Raman laser system to support two independent lasers. Furthermore, the Raman control system must be upgraded to support real-time trajectory integration using data from the inertial cosensors.

6.5.1 Upgraded Raman Control System

We present an analysis of a variety of possible approaches for implementing the trajectory propagation and interferometer feedforward, starting with the least technically challenging but lowest performance. Numerical studies demonstrated that to achieve the desired trajectory propagation accuracy, we require a fourth order Runge-Kutta integration on the cosensor outputs.

One approach is to simply perform the trajectory propagation in software and writing the DDS update using our current control system interface. The advantage of this is that most of the hardware control was already in place, and translation of the propagation algorithm from pseudocode to CPU code is the most straightforward. However, the delay for the final cosensor update would be limited by software. We estimated that 1 ms would be sufficient for our purposes. However, latency in the communication interface between the cosensors and the PC, and the PC and the FPGA would render this approach infeasible.

Another possibility is a microcontroller based approach which would form a separate Raman control subsystem independent of the PC. This would limit the communication delays to purely hardware-based timings. Investigating the decompiled code, and the cycle counts of typical implementations of the AVR instruction set, we find that even in the best case scenario the algorithm would not meet our timing constraints. The limited clock speed of typical microcontrollers of approximately 10 MHz to 100 MHz results in a slow calculation of the Runge-Kutta integration.

As a result of these limitations, we decided in favor of an FPGA-based approach.

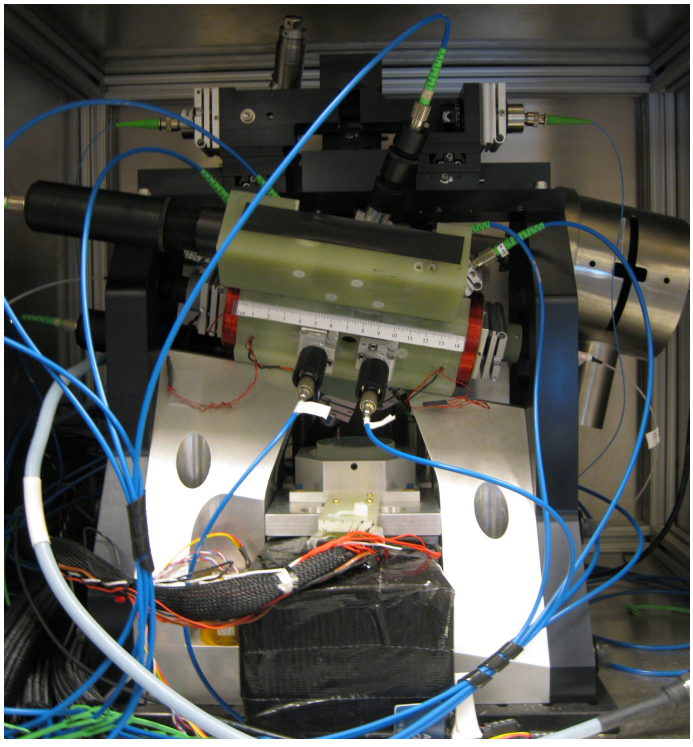

Figure 6.9: Picture of upgraded sensor head with rigid Raman delivery system and cosensor testbench. The Raman light is delivered by three launchers with independent orientation and position control. The Raman beam is oriented parallel to gravity to reduce systematic phase shifts caused by variations in Raman beam direction, which change the propagation of gravity on the measurement axis. Below the Raman retro mirror are the cosensors, which are occluded by a temperature-controlled oven.

A field-programmable gate array (FPGA) is a reconfigurable integrated circuit, which may be programmed "in the field". This has the advantage of speed comparable to application-specific integrated circuits (ASICs), while being readily programmable to facilitate development. FPGAs are seeing increased use in atomic physics, as experimental demands of timing and flexibility become more stringent [92, 93, 94]. The FPGA approach is guaranteed to hit the necessary timing constraints. However, there lies difficulty in translation of the propagation algorithm, which is inherently software based, to a hardware based approach. The propagation algorithm was written primarily by Draper Laboratories.

To maintain compatibility with the software control system, the FPGA has a toggle switch. In open-loop mode, the system uses frequencies and phases set by the software. In closed-loop mode, the FPGA overrides these values for the final pulse using values calculated from the propagator. This provides a straightforward method for maintaining the same laser scanning software we used before, while enabling closed-loop operation. Details of the code are shown in Appendix D. In the end, the algorithm easily met timing constraints, with an update delay of 50 μs. This corresponds to a fundamental jerk limit of 10 g/s, which is more than sufficient for our purposes.

Meanwhile, the Raman laser system was upgraded to support two independent lasers, along with a new optomechanical frame for enhanced mechanical stability. Previously, a single Raman laser was used for all three beams. Furthermore, the Raman module used a single, fixed orientation for all three beams. Optimizing the alignment for all pulses proved to be a difficult and time-consuming task. Theoretically, each beam can be oriented individually in favor of maximal Rabi frequency. This is because the Raman wavevector is not defined in terms of the orientation of each beam, but rather by the common retro-reflecting mirror. Furthermore, phase coherence is still maintained since the relevant phase is the phase of the two colors with respect to each other, not the phase of each beam. Thus, as described previously we expanded the system to include a second Raman laser, including a new EOM and TA.

A picture of the upgraded sensor module is shown in Fig. 6.9. The purpose of this design is to provide a rigid test bench rather than a demonstration of the potential size of the device. The retro-reflecting mirror was replaced with a new rigid base, orienting the Raman wavevector to be parallel with gravity. This suppresses systematic phase errors arising from orientation of the Raman wavevector with respect to gravity, by making such errors second-order sensitive. Furthermore, this base contained hardpoints for mounting auxiliary cosensors aligned with the Ra-

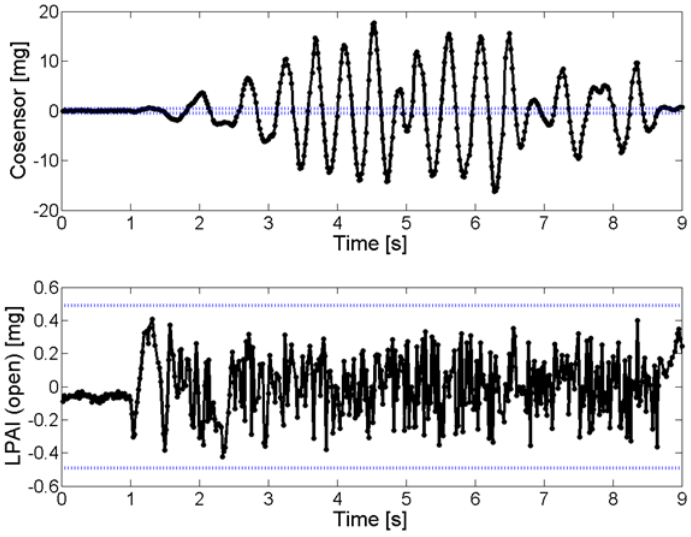

Figure 6.10: Open loop operation of the interferometer. The magnitude of acceleration exceeds several fringes. The resulting interferometer readout is noisy, operating at random points along the fringe.

man wavevector. The Raman laser mount was replaced with a platform bolted to the retro-reflecting mirror base, and containing three independent Raman launchers. Each of these launchers had independent position and orientation control, enabling us to optimize the interrogation time (by separating the beams) and Rabi frequency (orientation). We found that in practice, we were able to increase the interrogation time to $T = 4.5$ ms.

6.5.2 Closed Loop Demonstration

We perform a demonstration of the closed-loop interferometer. The cosensor bias and scale factor were tuned manually using the output of the interferometer. In a full system, the interferometer would feed back to the cosensor bias and scale factor using a Kalman filter [95]. Furthermore, for this demonstration we use the accelerometer and tilt cosensors, without the rotation sensor.

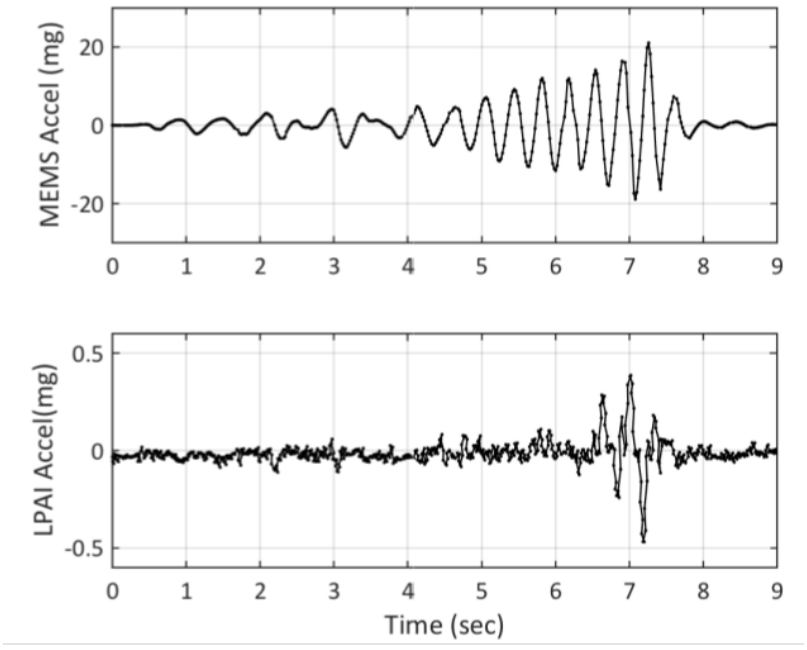

Figure 6.11: Demonstration of closed loop operation of the interferometer. The applied acceleration exceeds the fringe limits by a factor of 40. However, the interferometer fringe is constrained to well within zero phase shift. There is a slight residual phase at higher accelerations, but it is sufficiently slow to be tracked. The closed-loop data displays slightly better performance from what was actually observed, due to post-processing of the cosensor bias and scale-factor.

To carry out the demonstration, we apply an acceleration of approximately ± 20 mg and monitor the interferometer response in both closed and open loop operation. Results are shown in Fig. 6.11. The dashed lines in the plot correspond to the interferometer fringe limits. The applied acceleration exceeds these limits by a factor of 40. In the case of the open loop interferometer, the data occupies a random point within the interferometer fringe. This represents an overall reduction in the interferometer sensitivity, as well as possible ambiguity in the phase readout. However, the data for the closed loop interferometer is clearly constrained to nearly zero phase, and trackable up to ± 20 mg. Expanding the dynamic range beyond this level remains the subject of investigation. Systematic errors which may contribute to this include the absence of gyroscopic data, cosensor bias and scale factor, sensor non-

linearity, and axis misalignment. Nevertheless, we have successfully demonstrated closed loop operation and enhancement of the interferometer dynamic range by a factor of 40.

Chapter 7

Atom Interferometry in Warm Vapor

Much of the complexity of atom interferometers derives from the necessary lasers and optics for generating an ensemble of cold atoms. Indeed, our ensemble exchange atom interferometer required 19 beams, 12 of which were utilized for creating the MOTs. Eliminating the need for such a system would present a significant advance towards a compact, field-worthy device.

Success with compact systems based around warm atomic vapor cells has already been demonstrated with atomic clocks [96] and magnetometers [97, 98]. The bulk of the sensitivity derives from the sheer number of atoms available. For example, the density of atoms approaches $10^{12}/\text{cm}^3$, limited by radiation trapping [99]. Perhaps the greatest advantage is in the relative simplicity of the laser system. In the case of our experiment, only three lasers would be required: a pump, an interrogation beam, and a probe.

However, there are a number of significant challenges for adapting atom interferometry for use in warm vapor cells. The most pressing of these is that in clocks and

magnetometers, the interrogation time is maintained through the use buffer gasses and spin-relaxation coatings. However, both of these would destroy the inertial purity of the state. Thus, the interrogation must take place within a limited timeframe, severely limiting the sensitivity. In fact, for a 1 cm cell the atoms are ballistic for a mere 10 μs before colliding with the cell wall. Again, we may operate at a higher data-rate to recover some of the lost sensitivity.

7.1 Experiment

The experimental apparatus consists of a vacuum cell, pump beam, Raman interrogation beam, and probe beams Fig. 7.1. The presence of two probe beams will be visited later. The vacuum cell is a 2 cm $\times$ 4 cm $\times$ 10 cm rectangular cell. The full vacuum system consists of the cell, a 5 l/s ion pump, and a pure rubidium sample. We increase the vapor density of rubidium by heating the cell to 39 °C, corresponding to a vapor density of 4×10^{10} atoms/cm^3. The cell is heated by a warm air flow which maintains an even temperature distribution, avoiding thermal gradients across the cell which distort optical wavefronts.

The experiment proceeds as follows. Between shots of the experiment, an optical pumping beam detuned 80 MHz blue of the $|F = 2\rangle \rightarrow |F' = 2\rangle$ D1 transition pumps the atoms into $|F = 1\rangle$. Typically, atoms which make contact with the cell walls may undergo depumping into $|F = 2\rangle$, contributing a noisy background signal. We thus make use an anti-relaxation coating which maintains maintains the atomic spin polarization for several wall bounces. While there are many investigations of various anti-relaxation coatings, none of them consider the constraint of low vapor pressure, which is necessary to maintain the inertial purity of the detected atoms. We use octyldecyltrichlorosilane as our coating, which has demonstrated negligible outgassing due to its relatively high reactivity. We find there is sufficient circulation of atoms between the various velocity classes due to the wall bounces to polarize

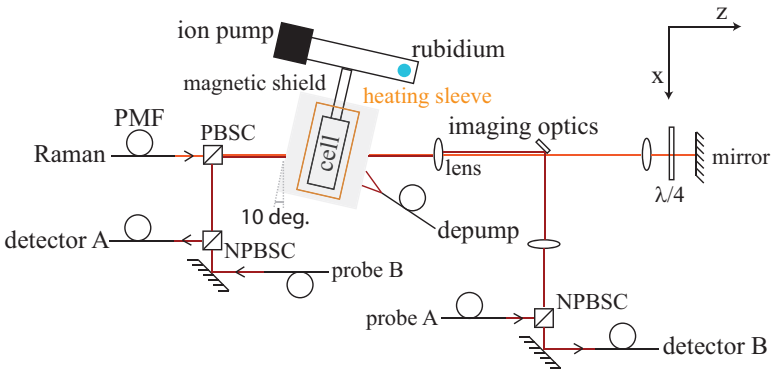

Figure 7.1: Apparatus for the warm vapor cell atom interferometer. It consists of the vacuum cell, a pump beam, two probe beams, and a Raman beam. A combination of polarization and imaging techniques separates the Raman beam from the probe beams for detection. A 10° tilt of the cell minimizes reflections which produce a Doppler-free signal. Figure reprinted from [61].

the entire thermal velocity distribution. We thus achieve a spin polarization of 90% in $|F = 1\rangle$ with a spin relaxation time of 23 ms, which is representative of several thousand wall bounces without depumping.

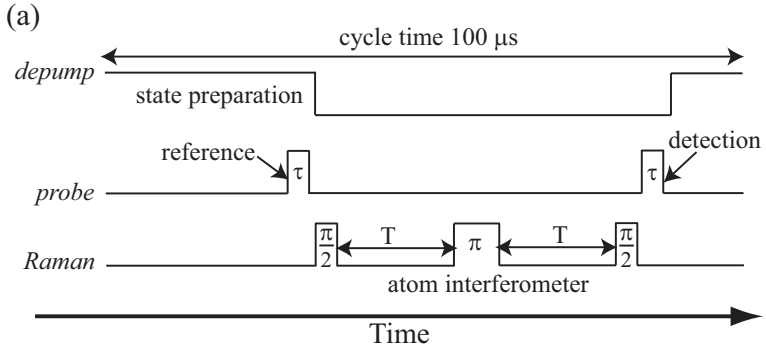

Figure 7.2: Timing diagram for the warm vapor cell atom interferometer experiment. A reference probe pulse marks the start of the experiment. The pumping beam is shut off, and the interferometer takes place with a $T = 15$ μs interrogation. A probe pulse detects the number of atoms in $|F = 2\rangle$ by absorption, and the pump is activated until the next shot. Figure reprinted from [61].

A background shot of the probe laser beam marks the start of the experiment. The pumping beam is switched off, and the Raman interrogation takes place with a $\pi/2 - \pi - \pi/2$ pulse sequence, with some interrogation time T on the order of 10 μs. The Raman laser is seeded by a fiber laser at 1560 nm and modulated near the hyperfine transition. The light is then amplified to 30 W and doubled to 780 nm in a periodically-poled lithium niobate crystal. The carrier light is locked 1.2 GHz red of the D2 $|F = 2\rangle \rightarrow |F' = 2, 3\rangle$ crossover transition via a beatnote offset lock. This results in a peak power of approximately 3 W which is collimated to a 5.6 mm $1/e^2$ radius. This corresponds to a two-photon Rabi frequency of $\Omega_{\text{eff}} = 2\pi \times 1.61$ MHz. The beam is delivered to the cell polarized linearly, and retro-reflected with a mirror and quarter-waveplate. The lin $\perp$ lin polarization configuration suppresses the Doppler-free transition. Although the Raman beam contains both laser frequencies co-propagating, the selected velocity class is detuned sufficiently far from zero to separate the resonance conditions, in a manner similar to that of the ensemble-exchange sensor.

A final probe pulse performs single-state absorption detection of the atomic ensemble. The probe is tuned 10 MHz blue of the D2 $|F = 2\rangle \rightarrow |F' = 3\rangle$ transition. The beam is collimated to a 2.8 mm $1/e^2$ radius, corresponding to an intensity of 0.18 mW/cm^2. This corresponds to a saturation parameter $s_0 = 0.1$, thus favoring a linear response of probe absorption. The output light is collimated into a fiber and directed towards a detector. After the detection event, the pump beam is activated and the cycle repeats.

The Raman and probe detunings are tuned to address the same velocity class of atoms. In a sense, this performs the role of ensemble preparation as a small velocity slice is selected from the entire thermal velocity distribution. In fact, one may consider a multitude of simultaneous interferometers operating on different velocity classes. This would in principle be limited by the Rabi width of the transition, with $2k_{\text{eff}}v_B/\Omega_{\text{eff}} \approx 22$ interferometers possible in our experiment. As a demonstration

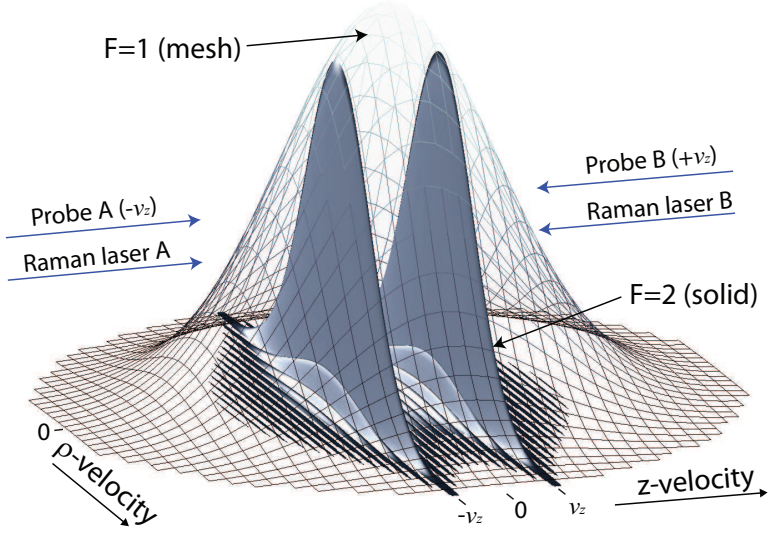

Figure 7.3: Conceptual diagram of velocity selection and dual interferometers in warm vapor. The mesh represents the Maxwell-Boltzmann velocity distribution of the atoms. The probes select two velocity slices from this distribution (shown in blue) which constitutes the atoms participating in the interferometer. The interferometer operates on each velocity slice with opposite $\mathbf{k}_{\text{eff}}$ vectors, enabling common-mode noise rejection. Figure reprinted from [61].

of this concept, we employ two interferometers at velocity classes located ±7.8 m/s apart, corresponding to the probe detuning explained earlier. We achieve this by counter-propagating the probe laser and adding in a second detector. Since both colors of light are present in the Raman beam for both directions, the transition is able to address velocity classes with either sign. Furthermore, these transitions feature equal and opposite sensitivity to acceleration, due to the opposing Raman wavevectors. This provides common-mode rejection of many detection induced noise sources, doubling the acceleration sensitivity.

The experiment requires the Raman and probe beams to travel nearly co-propagating so that they address the same velocity class. However, since these lasers are nearly the same frequency (780 nm), we use polarization and imaging techniques to combine and separate the beams, preventing the Raman laser from saturating the detector.

7.1.1 Control System

The control system consists of a Labview interface to National Instruments DAQmx hardware and an FPGA-based Raman control subsystem. The software provides the capability of rapid laser scans at rates on the order of 100 kHz. Frequency and phase information is stored on FPGA registers, and incremented using a counter generated from the DAQmx output. Given the limitations of NI hardware, operation at this data rate required the use of continuous waveform output and continuous analog input. Clever use of dummy clocks was necessary to maintain synchronization of the analog input signal to the output waveform.

7.2 Performance

A frequency scan of the Raman hyperfine detuning is shown in Fig. 7.4. We observe two resonances corresponding to the velocity slices selected by the probe at ± 7.8 m/s. This also confirms that the resonances are sufficiently far apart to avoid the Doppler-free transition. The residual Doppler-free transition at $\delta = 0$ is minimal. We see approximately 4×10^7 atoms undergo the transition.

The interferometer is then constructed using a $\pi/2 - \pi - \pi/2$ sequence of Doppler-sensitive Raman pulses, with an interrogation time of $T = 15$ μs. We find this to be an optimal tradeoff of interferometer sensitivity and phase resolution. We generate a plot of the interferometer fringe by scanning the rf phase of the third Raman pulse, as shown in Fig. 7.5. This fringe is the average of 200 phase scans. The fringe contrast of approximately 5×10^6 atoms represents a significant reduction from that of the Doppler-sensitive transition, and will be discussed in the next section.

We operate the two interferometers simultaneously, and find significant rejection of common-mode noise of 12 dB. The resulting phase noise is 35 mrad/shot at a

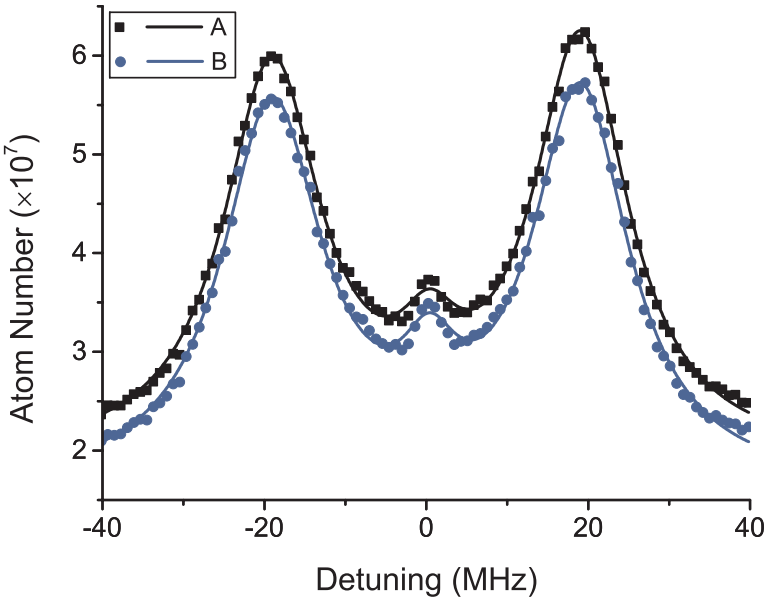

Figure 7.4: A scan of the hyperfine detuning in the warm vapor atom interferometer. The resonances correspond to the velocity slices selected by the probe at $v_z = \pm 7.8$ m/s. The widths of the Doppler-sensitive resonances are approximately $2\pi \times 15$ MHz. A small Doppler-free resonance is present. Figure reprinted from [61].

data rate of 10 kHz. This corresponds to an acceleration sensitivity of 10.4 $mg/\sqrt{\text{Hz}}$. The measured phase noise is a result of a fit over the entire fringe, resulting in an overestimation of the phase noise by a factor of $\pi/2$ compared with the optimal mid-fringe readout. We thus infer an acceleration sensitivity of 7.4 $mg/\sqrt{\text{Hz}}$.

To verify the Doppler-sensitivity of the interferometer, we conduct a measurement of the coherence length of the atomic wavepackets. By scanning the delay time of the final pulse $T_2 = T_1 + \delta T$, the average coherence length is revealed by the decay of the contrast envelope. This verifies that the atomic wavepackets do indeed separate by a distance exceeding the coherence length. This measurement is shown in the inset of Fig. 7.5. We measure a coherence length of 0.81(3) nm, corresponding to a velocity width of 0.37(2) m/s and a temperature of 1.44(6) mK. This is in agreement with the size of the velocity slice selected by the Raman beam, as we find the probe addresses

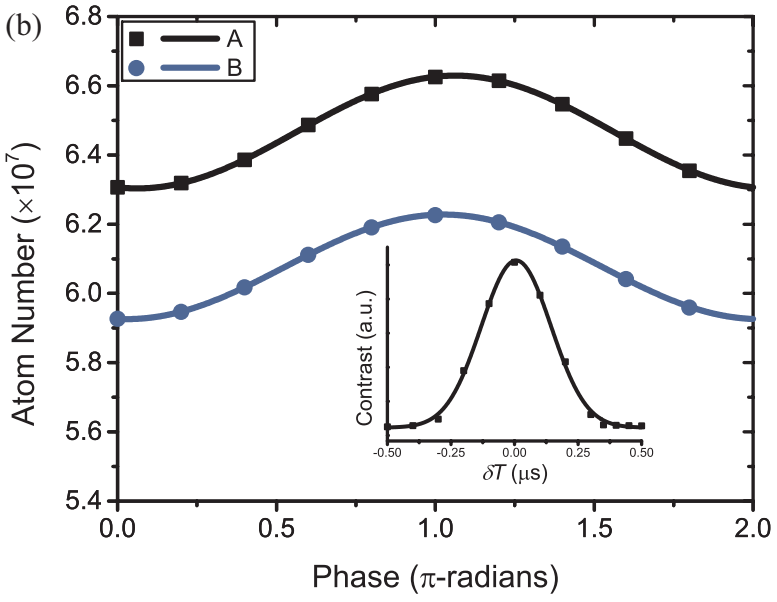

Figure 7.5: Demonstration of the warm vapor atom interferometer. The fringe is the average of 200 shots with $T = 15$ μs at a data-rate of 10 kHz. A π phase shift on this fringe corresponds to an acceleration of 88 mg. Inset: Contrast as a function of timing asymmetry $T_2 = T_1 + \delta T$. This reveals the size of the wavepacket overlap, corresponding to a velocity width of 0.37(2) m/s. This also serves to verify the Doppler-sensitivity of the interferometer. Figure reprinted from [61].

a velocity class which is approximately an order of magnitude larger, resulting in limited Raman pulse efficiency.

7.2.1 Atom Number Calculation

We now consider the fundamental sensitivity of the accelerometer under current and optimal conditions. We thus wish to calculate the number of atoms participating in the interferometer, as well as the number of atoms contributing to the noise.

In steady-state, the number of atoms addressed by the probe beam is constant. It is given by the product of the atomic density n, the probe beam volume $\pi r_p^2 l$ where r_p is the radius of the probe and l is the length of the cell, and the fraction

of the selected velocity class. The denominator of this fraction is given by the total number of atoms at that velocity group within the thermal velocity distribution. For $v_z \ll v_B$, we assume a nearly zero velocity class so the total number of atoms is $\sqrt{2\pi}v_B$. The number of atoms which actually contribute to the signal is the sum of atoms which reach $|F=2\rangle$ via the interferometer, and the atoms which fail to pump into $|F=1\rangle$ as a consequence of the limited optical pumping efficiency. This first term is given by the product of the interferometer fringe contrast ξ and the Raman velocity width, Ω_R/k_{eff}. The second term is given by the product of the optical pumping inefficiency $(1-\mathcal{E})$ and probe velocity width δv. Thus, the total number of detected atoms is

$$N_{\text{tot}} \approx \left(\frac{\xi\Omega_R}{k_{\text{eff}}} + (1-\mathcal{E})\delta v\right)\frac{n\pi r_p^2 l}{\sqrt{2\pi}v_B} \tag{7.1}$$

To calculate the number of atoms participating in the interrogation, we first model the number of atoms that leave some detection volume after a time t, due to their thermal velocity. We first calculate this in one dimension assuming an initially uniform distribution of atoms within some length $2a$. Averaging over all initial and final atom positions, the number of atoms remaining within the length $2a$ is then given by,

$$N(t) = \frac{1}{2av_B\sqrt{2\pi}}\int_{-a}^{a}\int_{-a}^{a}\exp\left(\frac{-(x-x_0)^2}{2v_B^2t^2}\right)\mathrm{d}x\mathrm{d}x_0, \tag{7.2}$$

where $v_B = \sqrt{k_B\mathcal{T}/m}$ is the Maxwell-Boltzmann atomic velocity. Defining $\tau = a/v_B$ as the characteristic time it takes to traverse the cell, this integral evaluates to

$$N(t) = \sqrt{\frac{2}{\pi}}\frac{t}{\tau}\left(e^{-\frac{1}{2}(\tau/t)^2}-1\right) + \text{erf}\left(\frac{1}{\sqrt{2}}\frac{\tau}{t}\right). \tag{7.3}$$

In the case of a multidimensional rectangular cell, the number of atoms is simply the product of Eq. 7.3 over each dimension. We find that in the case of a cylindrical cell, we may approximate this equation by matching the cross-sectional areas ($a = \sqrt{\pi}r/2$) which has a maximal error of 2.2% from the numerical integration over the cylinder.

However, in the direction of the probe and Raman beams there is significant velocity selection. While in the transverse directions this equation holds, we find the wall collisions in the longitudinal direction to be negligible. Therefore, the time-dependence exists solely in the transverse directions. After we include the number of atoms within the volume of the Raman beam and velocity width of the Raman transition, we have

$$N_{\text{int}} \approx \left[\sqrt{\frac{2}{\pi}} \frac{t}{\tau} \left(e^{-\frac{1}{2}(\tau/t)^2} - 1 \right) + \text{erf}\left(\frac{1}{\sqrt{2}} \frac{\tau}{t} \right) \right]^2 \frac{\xi \Omega_R n l \pi r_p^2}{\sqrt{2\pi} k_{\text{eff}} v_B}. \tag{7.4}$$

Substituting our current experimental parameters, we find an ideal phase noise of 4.9 mrad/shot corresponding to an acceleration sensitivity of 1.4 $\text{m}g/\sqrt{\text{Hz}}$. This estimate is approximately an order of magnitude lower than what we observe. We suspect this is a consequence of pulse area noise due to fluctuations in Raman beam intensity. In the case of an atom interferometer in resonance for all three pulses the phase is second order sensitive to this. However, many of the atoms participating in the interrogation are driven off-resonance. Furthermore, over $T = 15$ μs this is significant movement of atoms in and out of the detection and Raman beam volume. In particular, the final $\pi/2$ pulse transfers a significant fraction of non-participating atoms into the detection state, $|F = 2\rangle$. We measure a pulse area noise of 0.3%, which agrees approximately with the observed fringe offset noise of 1×10^4 atoms. While the dual interferometers should cancel this effect, we suspect there is some miss-match between the two Rabi frequencies.

Our experimental parameters are optimized under our limited optical pumping efficiency. If we were to assume perfect optical pumping, the number of background atoms contributing to our detection signal decreases significantly. In fact, while maintaining the total amount of Raman power we reoptimize our experimental parameters assuming perfect optical pumping. This expands the size of our detection cross section to approximately 1 cm^2 and increased the interrogation time to $T = 20$ μs.

From this, we predict an ideal acceleration sensitivity of 55 $\mu g/\sqrt{\text{Hz}}$.

Chapter 8

Conclusion & Outlook

We have demonstrated high data-rate atom interferometry with prospects towards a compact, field-worthy inertial sensor. As a prototype experiment, we demonstrated an atom interferometer accelerometer operating at data rates up to 300 Hz. This demonstrated the feasibility of a compact sensor robust against dynamic inertial conditions. Furthermore, this illuminated the necessity of ensemble recapture, and motivated development of a dual-axis sensor.

We designed and constructed a compact dual-axis atom interferometer inertial sensor capable of simultaneous acceleration and rotation rate measurements. The device relies on a technique we refer to as "ensemble exchange" to achieve a high flux source of ultracold atoms with 7×10^6 atoms/shot at a data-rate of 60 Hz, with high duty cycle and minimal loading time. We characterize the robustness of this source to dynamic inertial conditions, and estimate the technique may endure 10 g of acceleration and 20 rad/s of rotation rate before atom number losses become significant.

From this source of ultracold atom flux, we construct the atom interferometer using stimulated Raman transitions. We demonstrate an acceleration sensitivity of 0.9 $\mu g/\sqrt{\text{Hz}}$ and rotation rate sensitivity of 1.1 $\mu\text{rad/s}/\sqrt{\text{Hz}}$, making this a com-

pelling prospect for inertial navigation application. We then conducted an analysis of noise sources in the experiment, and predict a sensor achieving approximately 100 n$g/\sqrt{\text{Hz}}$ and 100 nrad/s/$\sqrt{\text{Hz}}$ with the same tolerance to inertial conditions to be feasible in a compact, engineered package. From here, we expanded the dynamic range of the device by a factor of 40 through the use of inertial cosensors, and predict this factor may be enhanced to cover dynamic input up to the limits of the ensemble flux. Finally, we have demonstrated a novel concept of atom interferometry in warm vapor, which presents a compelling prospect for simplifying the stringent requirements of engineering cold atom laser systems.

Atom interferometer technology is continually evolving with new methods to push the sensitivity to its absolute limits. While our approach was to engineer the simplest manifestation of light pulse atom interferometer techniques, a wide variety of enhancements may be possible in a robust, compact package. One possibility is the use of large momentum transfer which recoils several photons for each pulse in the interferometer [24, 100]. This increases the area enclosed by the interferometer, increasing the sensitivity in proportion to the number of photon recoils. Another possibility involves performing the Raman interrogation from inside an optical cavity to provide power enhancement, spatial filtering, and a precise beam geometry [55]. These frontiers are limited by the shot noise limit, fundamentally restricting the sensitivity of the phase readout to $\delta\phi = 1/\sqrt{N}$. However, through the use of entangled states it is possible to achieve a phase noise limited by $\delta\phi = 1/N$, known as the Heisenberg limit [101, 102, 103]. The field of quantum enhanced metrology is rich with investigations of squeezed atomic ensembles [104, 105], which present a compelling prospect for enhancing the sensitivity of atom interferometers [106, 105].

Atom interferometers have clearly demonstrated their potential as an emerging technology. This is evidenced by the rapid growth of companies such as AOsense and ColdQuanta which are actively developing cold atomic sensors. While there are still many challenges involving the transition from a laboratory physics experiment to an

engineered device, the prospect for cold atom sensor technology to make significant advances in applied metrology remains strong.

Appendices

Appendix A

Rubidium 87 Atomic Structure

We present a brief overview of relevant physical and optical parameters for ^{87}Rb and the D1 and D2 optical transitions. These numbers are all derived from reference [107].

Physical Constants		
Speed of Light	c	2.99792458×10^8 m/s
Planck's Constant	$\hbar$	$1.054571596(82) \times 10^{-34}$ J $\cdot$ s
Bohr Magneton	μ_B	$9.27400899(37) \times 10^{-24}$ J/T
Boltzmann's Constant	k_B	$1.3806503(24) \times 10^{-23}$ J/K
^{87}Rb **Physical Properties**		
Atomic Mass	m	$1.44316060(11) \times 10^{-25}$ kg
Melting Point	T_M	39.31 °C
D2 Optical Properties		
Frequency	ω_0	$2\pi \cdot 384.2304844685(62)$ THz
Wavelength	λ	780.241209686(13) nm
Natural linewidth	Γ	$2\pi \cdot 6.065(9)$ MHz
Recoil velocity	v_r	5.8845 mm/s
Doppler Temperature	T_D	146 μK
Saturation Intensity (cycling)	I_{sat}	1.669(2) mW/cm^2
D1 Optical Properties		
Frequency	ω_0	$2\pi \cdot 377.1074635(4)$ THz
Wavelength	λ	794.9788509(8) nm
Saturation Intensity (π-polarized)	I_{sat}	4.484(5) mW/cm^2

Table A.1: ^{87}Rb D line physical and optical properties.

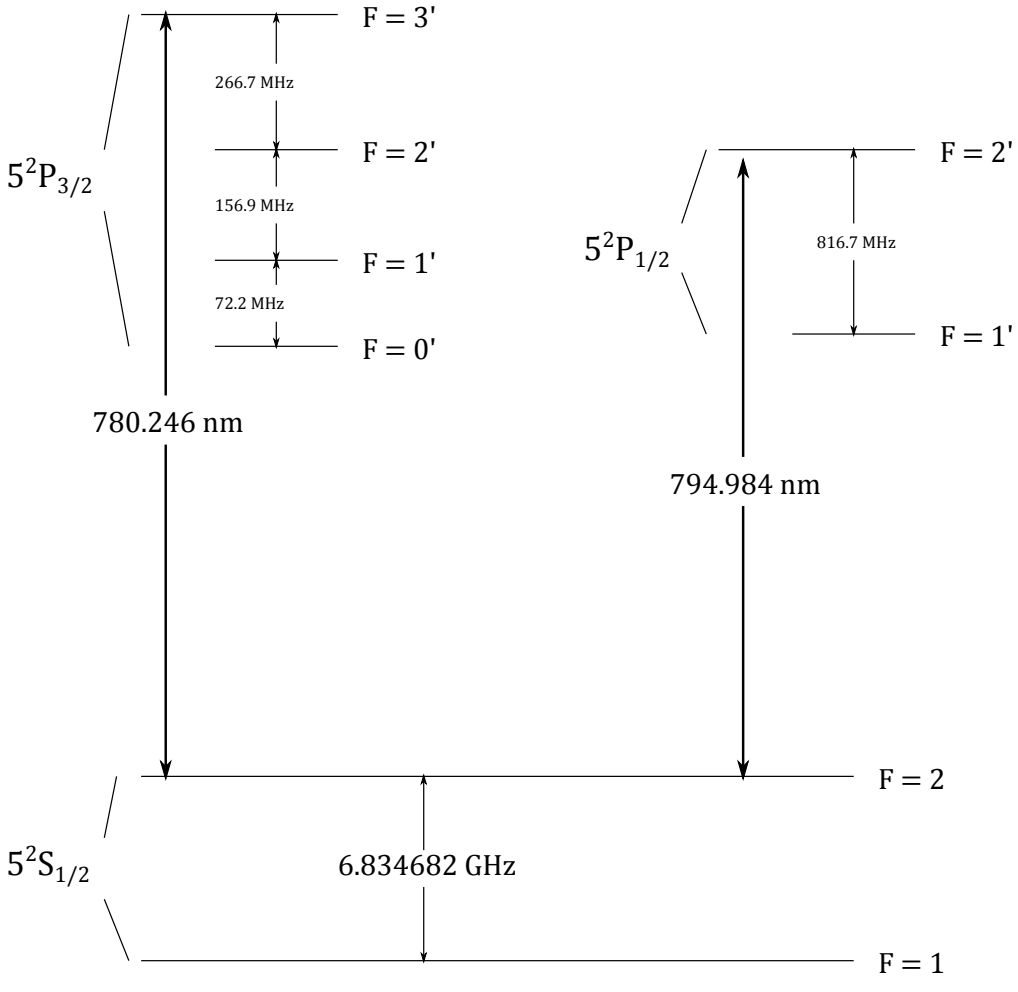

Figure A.1: ^{87}Rb D1 & D2 spectroscopy reference.

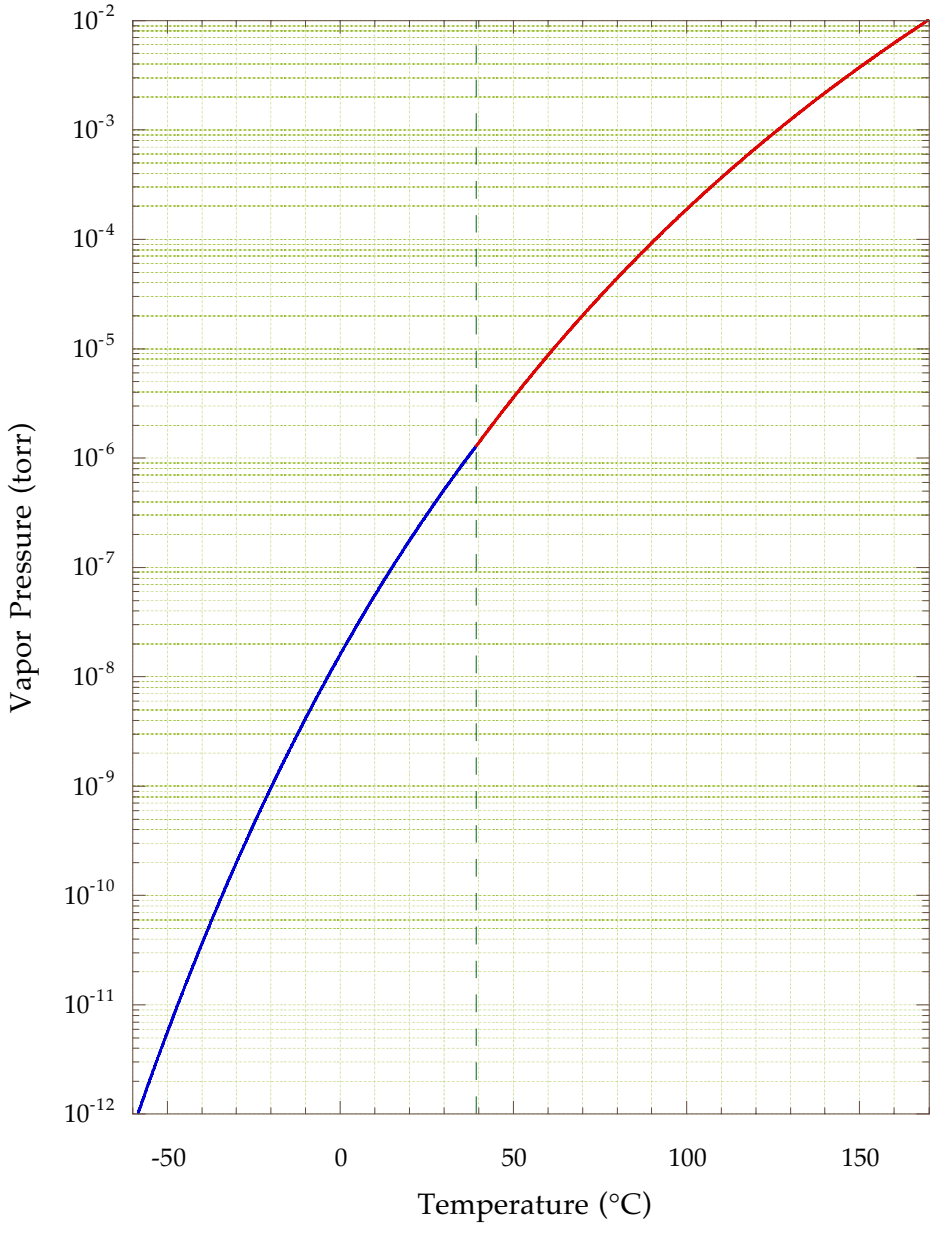

Figure A.2: Rubidium vapor pressure as a function of temperature.

Appendix B

MOT Calculation Overview

We present an overview of the code used to calculate the MOT atomic trajectories and recapture efficiency. While there is much literature on the subject of simulating MOTs [108, 109], we are concerned in particular with the problem of recapture. As such, we opted to develop our own simulation.

We use a Monte-Carlo technique [110] by simulating each photon scatter. Assuming some scattering rate γ, the number of photon scatters in some interval T obeys Poisson statistics, with distribution parameter $\lambda = \gamma/T$. The most direct way to simulate this is to step a small time δt. The probability of scattering a photon is simply $\gamma(\delta t)$, for $\delta t \ll 1/\gamma$. However, this is quite inefficient as for an accurate simulation, typically δt must be at most an order of magnitude less than $1/\gamma$. A much more efficient solution is to step the dynamics until the next photon scatter, Δt drawn from a probability distribution. It turns out, this distribution is the exponential probability distribution,

$$\Delta t = \gamma e^{-\gamma t}, \;\; t >= 0. \tag{B.1}$$

Now suppose we have multiple competing rates γ_k for $k = [1, n]$. One potential solution is to roll n random Δt_ks and simply choose the smallest one. However,

this requires rolling n random numbers, which can become quite inefficient. A more efficient solution is to utilize the properties of the exponential distribution. Namely, the exponential distribution is memoryless. That is, the conditional probability for the event to occur is independent of the time of the actual event. This enables [111] the following technique.

First, roll a random Δt from the exponential distribution with $\gamma = \sum_k \gamma_k$. This correctly gives the time of the next photon scatter. However, for our simulation it is necessary to know which of the ks generated the scatter to calculate the direction of the photon recoil. Thankfully, as a consequence of the Poisson distribution being memoryless, the scattering beam is simply given by the discrete probability distribution $p_i = r_i / \left(\sum_k r_k\right)$. Thus, by calculating the sum of the r_ks and rolling two random numbers, it is possible to perform this calculation for any n.

We thus present our simulation algorithm in pseudocode. Our simulation system consists of an array of atoms to form the ensemble, an array of laser beams, and an array of magnetic-field coils. The simulation proceeds as follows.

```
For each step
  For each atom
    For each coil
      Calculate magnetic field and append to total B.
    For each laser
      Calculate scattering rate r[i] using magnetic field B.
    Draw a random scattering-time dt via sum r[i]'s.
    Draw a random j via r[i]'s.
    Step the atomic trajectory by dt.
    Recoil atomic velocity by hbar*k[j]/m.
    Increment time by dt.
```

Note that this algorithm may be sped up by using the same probability dis-

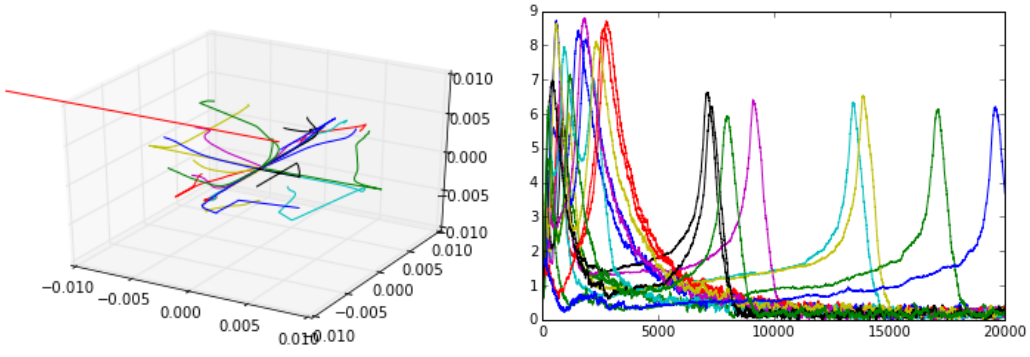

Figure B.1: Sample results from magneto-optical trap simulation. Left: Trajectories of atoms as they fall into the trap. The coordinate axes are in units of meters. Right: RMS velocity of atoms as a function of time. The x-axis is in units of $10/\Gamma$, and the y-axis in units of Γ/k.

tribution for multiple photon scatters n. This is valid as long as the constraint $n\hbar k/m \ll \Gamma/k$ is maintained. This states that the Doppler shift doesn't change significantly after n photon scatters. The ratio of these quantities is approximately 1000, so 100 scatters should maintain this constraint. Furthermore, the distance the atom travels must be small relative to the size of the magnetic field gradient. At the capture velocity, 100 photon scatters is well within this limit.

Another possible speedup is threading the simulation over the ensemble. For this simulation, threading is trivial as the atoms act independently over each other. A more advanced simulation would take the atomic interaction into account, and threading is likely to provide a smaller speedup.

With this simulation, we were able to model trapping of the cold atomic ensemble, and measure a Doppler-limited temperature (see Fig. B.1). Using the simulation to drop and recapture the ensemble is the subject of future work.

Appendix C

Control System Overview

The control system for the experiment is written in C#, and based heavily on the National Instruments DAQmx library and hardware system. It was designed in three layers, according to the Model-view-controller (MCV) software architectural pattern. First, a general purpose library which abstracts away many of the details concerning the specifics hardware operation. For example, control of an AD9852 DDS is abstracted away into a "Frequency Generator" interface. This enables the user to replace the DDS by providing a new class to match the interface without replacing higher-level code. The second layer defines the experiment itself using components derived from the first layer. For example, parameters such as "Raman detuning" are routed to a particular parameter in a particular piece of hardware. This layer also handles tasks such as experimental sweeps, data processing, and data storage. The third layer consists of the user interface at which point most of the hardware details are abstracted away.

These components are described in Fig. C.1. This figure showcases the important classes in the control system, as well as a sample of relevant methods. The "User Interface", "Controller", and "Experiment" classes provide an implementation of the MCV model described above. Each of these classes exists in an independent thread,

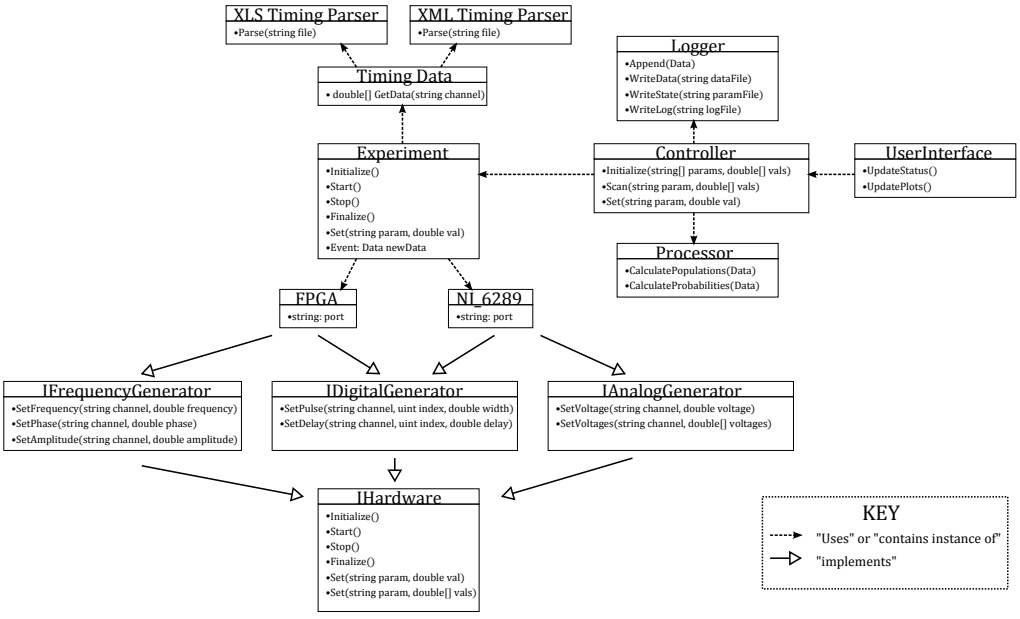

Figure C.1: Class diagram for the software control system.

with data queue's used to transfer data between them. This ensures any bottlenecks do not affect the performance of the experiment.

Every piece of hardware used in the experiment has an associated class. This class inherits from interfaces describing the functionality of the device, for example "IFreqGen" for a frequency generator. This enables a single piece of hardware to adhere to multiple templates. For example, our FPGA functions as both a frequency generator (which in the FPGA code is routed to the DDS) or a pulse generator (in this case, the Raman pulses). The Experiment class then types these as their relevant interfaces, and the FPGA class is only used on object instantiation. This enables simple replacement of hardware: as the new piece of hardware (assuming the class inherits the correct interfaces) only needs to be replaced in one line of code. Furthermore, this abstracts away details concerning specific hardware in the experiment class, i.e. the class is only aware of a "Raman Frequency Generator".

The timing data for the experiment is provided in the "TimingData" class. This

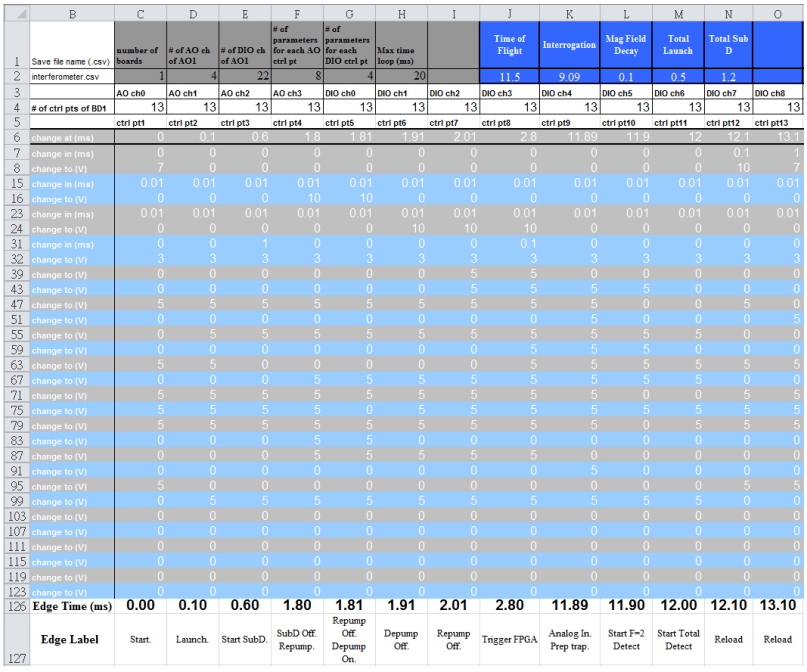

	B	C	D	E	F	G	H	I	J	K	L	M	N	O
1	Save file name (.csv)	number of boards	# of AO ch of AO1	# of DIO ch of AO1	# of parameters for each AO ctrl pt	# of parameters for each DIO ctrl pt	Max time loop (ms)		Time of Flight	Interrogation	Mag Field Decay	Total Launch	Total Sub D	
2	interferometer.csv	1	4	22	8	4	20		11.5	9.09	0.1	0.5	1.2	
3		AO ch0	AO ch1	AO ch2	AO ch3	DIO ch0	DIO ch1	DIO ch2	DIO ch3	DIO ch4	DIO ch5	DIO ch6	DIO ch7	DIO ch8
4	# of ctrl pts of BD1	13	13	13	13	13	13	13	13	13	13	13	13	13
5		ctrl pt1	ctrl pt2	ctrl pt3	ctrl pt4	ctrl pt5	ctrl pt6	ctrl pt7	ctrl pt8	ctrl pt9	ctrl pt10	ctrl pt11	ctrl pt12	ctrl pt13
6	change # (ms)	0	0.1	0.6	1.8	1.81	1.91	2.01	2.8	11.89	11.9	12	12.1	13.1
7	change in (ms)	0	0	0	0	0	0	0	0	0	0	0	0.1	1
8	change to (V)	7	0	0	0	0	0	0	0	0	0	0	10	7
15	change in (ms)	0.01	0.01	0.01	0.01	0.01	0.01	0.01	0.01	0.01	0.01	0.01	0.01	0.01
16	change to (V)	0	0	0	10	10	0	0	0	0	0	0	0	0
23	change in (ms)	0.01	0.01	0.01	0.01	0.01	0.01	0.01	0.01	0.01	0.01	0.01	0.01	0.01
24	change to (V)	0	0	0	0	0	10	10	10	0	0	0	0	0
31	change in (ms)	0	0	1	0	0	0	0	0.1	0	0	0	0	0
32	change to (V)	3	3	3	3	3	3	3	3	3	3	3	3	3
39	change to (V)	0	0	0	0	0	0	5	5	0	0	0	0	0
43	change to (V)	0	0	0	0	0	0	5	5	5	5	0	0	0
47	change to (V)	5	5	5	5	5	5	5	5	5	0	0	5	0
51	change to (V)	0	0	0	0	0	0	0	0	5	0	0	0	5
55	change to (V)	0	5	5	5	5	5	5	5	5	5	5	0	0
59	change to (V)	0	0	0	0	0	0	0	5	5	5	0	0	0
63	change to (V)	5	5	0	0	0	0	0	5	5	5	5	5	5
67	change to (V)	0	0	0	5	5	5	5	5	5	5	5	0	0
71	change to (V)	5	5	5	5	5	5	5	5	5	0	0	5	5
75	change to (V)	5	5	5	5	0	5	5	5	5	5	5	5	5
79	change to (V)	5	5	5	5	5	5	5	5	5	0	5	5	5
83	change to (V)	0	0	0	5	5	0	0	0	0	0	0	0	0
87	change to (V)	0	0	0	5	5	5	5	5	0	0	0	0	0
91	change to (V)	0	0	0	0	0	0	0	0	5	0	0	0	0
95	change to (V)	5	0	0	0	0	0	0	0	0	0	0	5	5
99	change to (V)	0	5	5	5	5	5	5	5	5	5	5	0	0
103	change to (V)	0	0	0	0	0	0	0	0	0	0	0	0	0
107	change to (V)	0	0	0	0	0	0	0	0	0	0	0	0	0
111	change to (V)	0	0	0	0	0	0	0	0	0	0	0	0	0
115	change to (V)	0	0	0	0	0	0	0	0	0	0	0	0	0
119	change to (V)	0	0	0	0	0	0	0	0	0	0	0	0	0
123	change to (V)	0	0	0	0	0	0	0	0	0	0	0	0	0
126	**Edge Time (ms)**	**0.00**	**0.10**	**0.60**	**1.80**	**1.81**	**1.91**	**2.01**	**2.80**	**11.89**	**11.90**	**12.00**	**12.10**	**13.10**
127	**Edge Label**	Start.	Launch.	Start SubD.	SubD Off. Repump.	Repump Off. Depump On.	Depump Off.	Repump Off.	Trigger FPGA	Analog In. Prep trap.	Start F=2 Detect	Start Total Detect	Reload	Reload

Figure C.2: Experiment timing specification interface for the control software.

contains information on digital and analog outputs, as well as triggering and clock information. The data for this class is specified as either an Excel file, or XML. The Excel interface encodes tabular data, while the XML interface uses a list of "control points" to specify changes in the waveform. Either of these is encoded into an output waveform, which is directed to the Experiment class.

While the hardware detail is encoded in the Experiment class, the Controller functions as a bridge between the user interface and experiment. The controller regulates all the non-hardware components of the experiment, such as data processing, data logging, etc.

Logging the data has proven to be a bottleneck in the past. The delay in writing to the hard disk may be as large as 10 ms as the hard drive may need to seek. In an experiment with a cycle-time as low as 3 ms, this is highly problematic. The most direct solution is to simply maintain the data in memory until the end of the

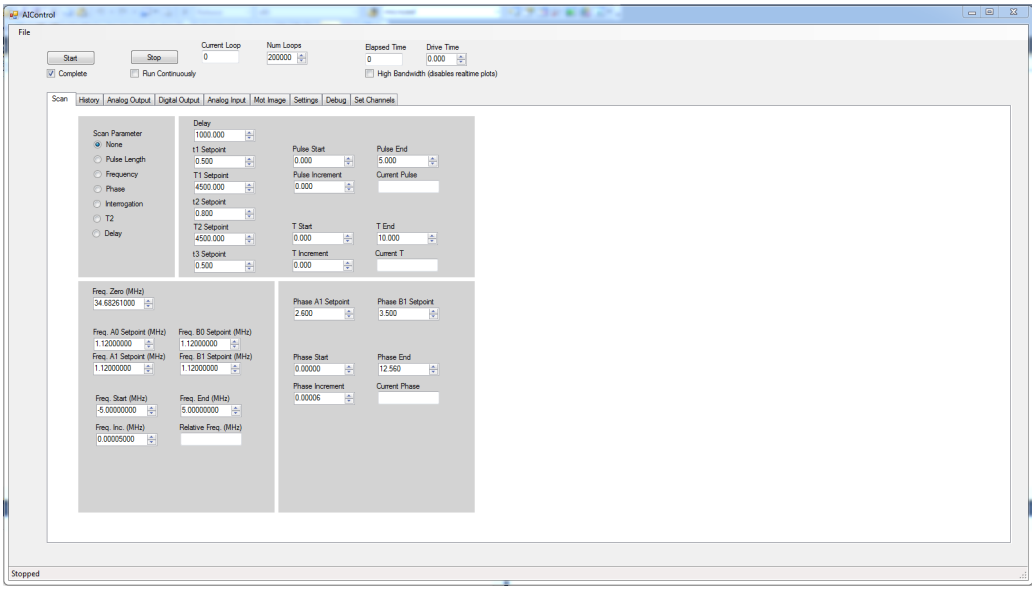

Figure C.3: Scanning and data-processing interface for the control software.

experiment, and log the data to disk. However, in the event of a software crash all the acquired data will be lost. Fortunately, once the seek time has elapsed, the data is written quickly to disk. Thus, the solution we employ is to maintain a queue. Adding data to the queue is very quick, and no longer bottlenecks the experiment. This enables the logger to stream the data to disk at it's own pace. Typically, we find the number of data points in the queue rarely exceeds 2 at a data-rate of 60 Hz.

Appendix D

FPGA Code Overview

In this section, we present an overview of the code used to control the Raman laser system and inertial feed-forward. This subsystem is responsible for controlling Raman pulse duration, frequency, and phase. The inputs consist of timing and frequency data from the PC, and four cosensors corresponding to acceleration, rotation, and two tilt sensors. The outputs are two Raman RF frequencies, AOM pulses, and an AOM selector for the middle pulse. For closed loop operation, the code must be able to perform Runge-Kutta integration on two ensemble trajectories using cosensor data sampled at 1 kHz, and rapidly program the result into the DDS. We attempted a microcontroller-based solution, but the execution time of the code did not meet timing constraints. We wrote an FPGA program as a combination of raw VHDL (Sandia), and VHDL compiled from Matlab HDL coder and Simulink (Draper). I present a brief overview of this code.

The Sandia team was responsible for the top level code, as well as the PC interface and pulse generation. The Draper team handled interfacing with the ADC and FPGA hardware, and porting the algorithm to VHDL. The PC interface was based on a serial communication program developed by Walter Gordy, and upgraded to support writes to the PC (rather than solely reads). Data was sent in 8 byte data

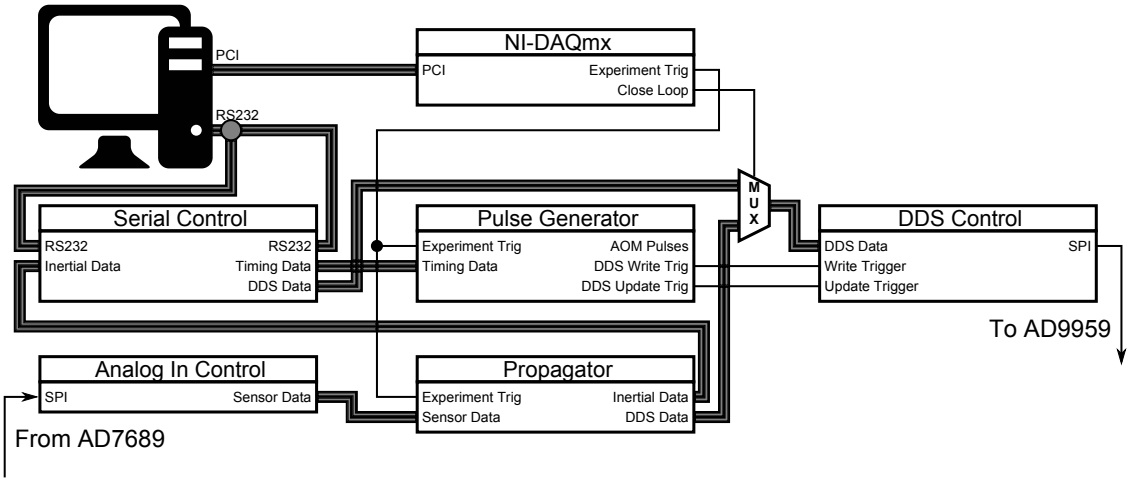

Figure D.1: FPGA system diagram.

bursts containing a 1 byte header which represented the address to write the data. Registers represented various Raman beam parameters, such as frequency and phase. Additionally, some registers contained timing parameters for the pulses. These registers were routed to the DDS and pulse generation modules, which were synchronized to the experiment via a trigger from the NI DAQ system.

The order of events is as follows. Prior to the first pulse, frequencies and phases given by parameters "Frequency/Phase-A/B-1" were programmed to the DDS. These represent the resonance conditions of each ensemble A and B for the first pulse. These frequencies and phases are maintained while the system outputs the first and second Raman pulse triggers. A secondary trigger for just the second pulse switches light from one of the Raman lasers to the middle beam, which is shared for the two ensembles.

During the ensemble trajectory, the analog input samples the cosensors at a rate of 1 kHz and the Runge-Kutta integration algorithm developed by Draper propagates the atomic trajectory. At each propagation step, the algorithm extrapolates the predicted third pulse phase and frequency which will lock the interferometer on

resonance and with zero phase. 50 μs before the final pulse, the software produces the last propagation update. In open loop operation, this update is ignored and parameters "Frequency/Phase-A/B-2" are programmed to the DDS. This enables diagnostic functions such as phase scanning of the final pulse. In closed loop mode, these parameters are overridden with the propagator result. After the final pulse, the result of the algorithm is sent to the computer via the serial interface, while the computer prepares the parameters for the next scan (if necessary). The inertial information is thus logged in both open and closed loop operation.

References

[1] Sandia National Laboratories is a multi-program laboratory managed and operated by Sandia Corporation, a wholly owned subsidiary of Lockheed Martin Corporation, for the U.S. Department of Energy's National Nuclear Security Administration under contract DE-AC04-94AL85000.

[2] Funded by DARPA: The views expressed are those of the author(s) and do not reflect the official policy or position of the Department of Defense or the U.S. Government. Distribution "A": Approved for Public Release, Distribution Unlimited. Contract: 017120917.

[3] "Iso 80000-3:2006, quantities and units – part 3: Space and time," Mar 2006.

[4] P. R. Berman, *Atom Interferometry*. Academic Press, 1997.

[5] F. Riehle, T. Kisters, A. Witte, J. Helmcke, and C. J. Bordé, "Optical ramsey spectroscopy in a rotating frame: Sagnac effect in a matter-wave interferometer," *Phys. Rev. Lett.*, vol. 67, pp. 177–180, Jul 1991.

[6] M. Kasevich and S. Chu, "Atomic interferometry using stimulated raman transitions," *Phys. Rev. Lett.*, vol. 67, pp. 181–184, Jul 1991.

[7] Q. Bodart, S. Merlet, N. Malossi, F. P. Dos Santos, P. Bouyer, and A. Landragin, "A cold atom pyramidal gravimeter with a single laser beam," *Applied Physics Letters*, vol. 96, no. 13, pp. –, 2010.

[8] J. M. McGuirk, G. T. Foster, J. B. Fixler, M. J. Snadden, and M. A. Kasevich, "Sensitive absolute-gravity gradiometry using atom interferometry," *Phys. Rev. A*, vol. 65, p. 033608, Feb 2002.

[9] G. Biedermann, *Gravity Tests, Differential Accelerometry and Interleaved Clocks with Cold Atom Interferometers*. PhD thesis, Standford University, 2007.

[10] T. L. Gustavson, *Precision Rotation Sensing Using Atom Interferometry*. PhD thesis, Stanford University, 2000.

[11] L. P. Parazzoli, A. M. Hankin, and G. W. Biedermann, "Observation of free-space single-atom matter wave interference," *Phys. Rev. Lett.*, vol. 109, p. 230401, Dec 2012.

[12] A. Hankin, *Rydberg Excitation of Single Atoms for Applications in Quantum Information and Metrology*. PhD thesis, University of New Mexico, 2014.

[13] B. Canuel, F. Leduc, D. Holleville, A. Gauguet, J. Fils, A. Virdis, A. Clairon, N. Dimarcq, C. J. Bordé, A. Landragin, and P. Bouyer, "Six-axis inertial sensor using cold-atom interferometry," *Phys. Rev. Lett.*, vol. 97, p. 010402, Jul 2006.

[14] S. Wu, E. Su, and M. Prentiss, "Demonstration of an area-enclosing guided-atom interferometer for rotation sensing," *Phys. Rev. Lett.*, vol. 99, p. 173201, Oct 2007.

[15] A. Wicht, J. M. Hensley, E. Sarajlic, and S. Chu, "A preliminary measurement of the fine structure constant based on atom interferometry," *Physica Scripta*, vol. 2002, no. T102, p. 82, 2002.

[16] M. Cadoret, E. de Mirandes, P. Clade, S. Guellati-Khelifa, C. Schwob, F. Nez, L. Julien, and F. Biraben, "Determination of the fine structure constant with atom interferometry and bloch oscillations on 87rb atoms," in *Precision Electromagnetic Measurements Digest, 2008. CPEM 2008. Conference on*, pp. 38–39, June 2008.

[17] J. B. Fixler, G. T. Foster, J. M. McGuirk, and M. A. Kasevich, "Atom interferometer measurement of the newtonian constant of gravity," *Science*, vol. 315, no. 5808, pp. 74–77, 2007.

[18] G. Lamporesi, A. Bertoldi, L. Cacciapuoti, M. Prevedelli, and G. M. Tino, "Determination of the newtonian gravitational constant using atom interferometry," *Phys. Rev. Lett.*, vol. 100, p. 050801, Feb 2008.

[19] G. Rosi, F. Sorrentino, L. Cacciapuoti, M. Prevedelli, and G. M. Tino, "Precision measurement of the newtonian gravitational constant using cold atoms," *Nature*, vol. 510, pp. 518–521, Jun 2014. Letter.

[20] G. W. Biedermann, X. Wu, L. Deslauriers, S. Roy, C. Mahadeswaraswamy, and M. A. Kasevich, "Testing gravity with cold-atom interferometers," *Phys. Rev. A*, vol. 91, p. 033629, Mar 2015.

[21] S. Dimopoulos, P. W. Graham, J. M. Hogan, M. A. Kasevich, and S. Rajendran, "Atomic gravitational wave interferometric sensor," *Phys. Rev. D*, vol. 78, p. 122002, Dec 2008.

[22] S. Dimopoulos, P. W. Graham, J. M. Hogan, M. A. Kasevich, and S. Rajendran, "Gravitational wave detection with atom interferometry," *Physics Letters B*, vol. 678, no. 1, pp. 37 – 40, 2009.

[23] A. Peters, K. Y. Chung, and S. Chu, "Measurement of gravitational acceleration by dropping atoms," *Nature*, vol. 400, pp. 849–852, Aug 1999.

[24] H. Müller, S.-w. Chiow, S. Herrmann, S. Chu, and K.-Y. Chung, "Atom-interferometry tests of the isotropy of post-newtonian gravity," *Phys. Rev. Lett.*, vol. 100, p. 031101, Jan 2008.

[25] M. A. Hohensee, S. Chu, A. Peters, and H. Müller, "Equivalence principle and gravitational redshift," *Phys. Rev. Lett.*, vol. 106, p. 151102, Apr 2011.

[26] F. Sorrentino, K. Bongs, P. Bouyer, L. Cacciapuoti, M. de Angelis, H. Dittus, W. Ertmer, A. Giorgini, J. Hartwig, M. Hauth, S. Herrmann, M. Inguscio, E. Kajari, T. Knemann, C. Lmmerzahl, A. Landragin, G. Modugno, F. Pereira dos Santos, A. Peters, M. Prevedelli, E. Rasel, W. Schleich, M. Schmidt, A. Senger, K. Sengstock, G. Stern, G. Tino, and R. Walser, "A compact atom interferometer for future space missions," *Microgravity Science and Technology*, vol. 22, no. 4, pp. 551–561, 2010.

[27] J. Hogan, D. Johnson, S. Dickerson, T. Kovachy, A. Sugarbaker, S.-w. Chiow, P. Graham, M. Kasevich, B. Saif, S. Rajendran, P. Bouyer, B. Seery, L. Feinberg, and R. Keski-Kuha, "An atomic gravitational wave interferometric sensor in low earth orbit (agis-leo)," *General Relativity and Gravitation*, vol. 43, no. 7, pp. 1953–2009, 2011.

[28] D. Johnson, *Long baseline atom interferometry.* PhD thesis, Stanford University, 2011.

[29] K. Moler, D. S. Weiss, M. Kasevich, and S. Chu, "Theoretical analysis of velocity-selective raman transitions," *Phys. Rev. A*, vol. 45, pp. 342–348, Jan 1992.

[30] E. L. Raab, M. Prentiss, A. Cable, S. Chu, and D. E. Pritchard, "Trapping of neutral sodium atoms with radiation pressure," *Phys. Rev. Lett.*, vol. 59, pp. 2631–2634, Dec 1987.

[31] S. M. Dickerson, J. M. Hogan, A. Sugarbaker, D. M. S. Johnson, and M. A. Kasevich, "Multiaxis inertial sensing with long-time point source atom interferometry," *Phys. Rev. Lett.*, vol. 111, p. 083001, Aug 2013.

[32] A. Sugarbaker, S. M. Dickerson, J. M. Hogan, D. M. S. Johnson, and M. A. Kasevich, "Enhanced atom interferometer readout through the application of phase shear," *Phys. Rev. Lett.*, vol. 111, p. 113002, Sep 2013.

[33] D. S. Durfee, Y. K. Shaham, and M. A. Kasevich, "Long-term stability of an area-reversible atom-interferometer sagnac gyroscope," *Phys. Rev. Lett.*, vol. 97, p. 240801, Dec 2006.

[34] T. L. Gustavson, P. Bouyer, and M. A. Kasevich, "Precision rotation measurements with an atom interferometer gyroscope," *Phys. Rev. Lett.*, vol. 78, pp. 2046–2049, Mar 1997.

[35] P. Groves, "Navigation using inertial sensors [tutorial]," *Aerospace and Electronic Systems Magazine, IEEE*, vol. 30, pp. 42–69, Feb 2015.

[36] A. D. King, "Inertial navigation - forty years of evolution," *GEC Review*, vol. 13, pp. 140–149, 1998.

[37] W. Wrigley, "History of inertial navigation," *Navigation*, vol. 24, pp. 1–6, Apr 1977.

[38] W. M. Macek and D. T. M. Davis, "Rotation rate sensing with travelingwave ring lasers," *Applied Physics Letters*, vol. 2, no. 3, pp. 67–68, 1963.

[39] G. Sagnac, "L'ther lumineux dmontr par l'effet du vent relatif d'ther dans un interfromtre en rotation uniforme," *Comptes Rendus*, vol. 157, pp. 708–710, 1913.

[40] V. Vali and R. W. Shorthill, "Fiber ring interferometer," *Appl. Opt.*, vol. 15, pp. 1099–1100, May 1976.

[41] J. L. Hall, M. Zhu, and P. Buch, "Prospects for using laser-prepared atomic fountains for optical frequency standards applications," *J. Opt. Soc. Am. B*, vol. 6, pp. 2194–2205, Nov 1989.

[42] S. R. Jefferts, J. Shirley, T. E. Parker, T. P. Heavner, D. M. Meekhof, C. Nelson, F. Levi, G. Costanzo, A. D. Marchi, R. Drullinger, L. Hollberg, W. D. Lee, and F. L. Walls, "Accuracy evaluation of nist-f1," *Metrologia*, vol. 39, no. 4, p. 321, 2002.

[43] T. P. Heavner, E. A. Donley, F. Levi, G. Costanzo, T. E. Parker, J. H. Shirley, N. Ashby, S. Barlow, and S. R. Jefferts, "First accuracy evaluation of nist-f2," *Metrologia*, vol. 51, no. 3, p. 174, 2014.

[44] V. Gerginov, N. Nemitz, S. Weyers, R. Schr?der, D. Griebsch, and R. Wynands, "Uncertainty evaluation of the caesium fountain clock ptb-csf2," *Metrologia*, vol. 47, no. 1, p. 65, 2010.

[45] J. Guena, M. Abgrall, D. Rovera, P. Rosenbusch, B. Chupin, M. Lours, G. Santarelli, P. Laurent, S. Bize, A. Clairon, and M. Tobar, "Recent atomic fountain clock comparisons at lne-syrte," in *Frequency Control and the European Frequency and Time Forum (FCS), 2011 Joint Conference of the IEEE International*, pp. 1–3, May 2011.

[46] C. W. Chou, D. B. Hume, J. C. J. Koelemeij, D. J. Wineland, and T. Rosenband, "Frequency comparison of two high-accuracy al^+ optical clocks," *Phys. Rev. Lett.*, vol. 104, p. 070802, Feb 2010.

[47] B. J. Bloom, T. L. Nicholson, J. R. Williams, S. L. Campbell, M. Bishof, X. Zhang, W. Zhang, S. L. Bromley, and J. Ye, "An optical lattice clock with accuracy and stability at the 10-18 level," *Nature*, vol. 506, pp. 71–75, Feb 2014. Letter.

[48] "Integrated micro primary atomic clock technology (impact)," 2008.

[49] R. Lutwak, "Micro-technology for positioning, navigation, and timing towards pnt everywhere and always," in *Inertial Sensors and Systems (ISISS), 2014 International Symposium on*, pp. 1–4, Feb 2014.

[50] S. Knappe, V. Shah, P. D. D. Schwindt, L. Hollberg, J. Kitching, L.-A. Liew, and J. Moreland, "A microfabricated atomic clock," *Applied Physics Letters*, vol. 85, no. 9, pp. 1460–1462, 2004.

[51] P. D. D. Schwindt, Y.-Y. Jau, H. Partner, D. K. Serkland, R. Boye, L. Fang, A. Casias, R. P. Manginell, M. Moorman, J. Prestage, and N. Yu, "Micro ion frequency standard," *Proc. SPIE*, vol. 8031, pp. 80310O–80310O–10, 2011.

[52] W. Xinan, *Gravity Gradient Survey with a Mobile Atom Interferometer*. PhD thesis, Stanford University, 2009.

[53] M. Kasevich, "Atom interferometric navigation sensors," in *Sensors, 2010 IEEE*, pp. 15–16, Nov 2010.

[54] J. Fang and J. Qin, "Advances in atomic gyroscopes: A view from inertial navigation applications," *Sensors*, vol. 12, no. 5, p. 6331, 2012.

[55] P. Hamilton, M. Jaffe, J. M. Brown, L. Maisenbacher, B. Estey, and H. Müller, "Atom interferometry in an optical cavity," *Phys. Rev. Lett.*, vol. 114, p. 100405, Mar 2015.

[56] D. L. Butts, J. M. Kinast, B. P. Timmons, and R. E. Stoner, "Light pulse atom interferometry at short interrogation times," *J. Opt. Soc. Am. B*, vol. 28, pp. 416–421, Mar 2011.

[57] R. Stoner, D. Butts, J. Kinast, and B. Timmons, "Analytical framework for dynamic light pulse atom interferometry at short interrogation times," *J. Opt. Soc. Am. B*, vol. 28, pp. 2418–2429, Oct 2011.

[58] H. J. McGuinness, A. V. Rakholia, and G. W. Biedermann, "High data-rate atom interferometer for measuring acceleration," *Applied Physics Letters*, vol. 100, no. 1, pp. –, 2012.

[59] A. V. Rakholia, H. J. McGuinness, and G. W. Biedermann, "Dual-axis high-data-rate atom interferometer via cold ensemble exchange," *Phys. Rev. Applied*, vol. 2, p. 054012, Nov 2014.

[60] T. L. Gustavson, A. Landragin, and M. A. Kasevich, "Rotation sensing with a dual atom-interferometer sagnac gyroscope," *Classical and Quantum Gravity*, vol. 17, no. 12, p. 2385, 2000.

[61] G. W. Biedermann, H. J. McGuinness, A. V. Rakholia, Y.-Y. Jau, D. R. Wheeler, J. D. Sterk, and G. R. Burns, "Atom interferometry in a warm vapor." In preparation., 2015.

[62] F. T. Arecchi and R. Bonifacio, "Theory of optical maser amplifiers," *Journal of Quantum Electronics*, vol. 1, pp. 169 – 178, Jul 1965.

[63] H. Metcalf and P. van der Straten, *Laser Cooling and Trapping*. Springer, 1999.

[64] C. J. Foot, *Atomic Physics*. Oxford University Press, 2004.

[65] S. Chu, L. Hollberg, J. E. Bjorkholm, A. Cable, and A. Ashkin, "Three-dimensional viscous confinement and cooling of atoms by resonance radiation pressure," *Phys. Rev. Lett.*, vol. 55, pp. 48–51, Jul 1985.

[66] D. B. Montgomery and J. Terrell, "Some useful information for the design of aircore solenoids," tech. rep., MASSACHUSETTS INST OF TECH CAMBRIDGE FRANCIS BITTER NATIONAL MAGNET LAB, Nov 1961.

[67] T. Bergeman, G. Erez, and H. J. Metcalf, "Magnetostatic trapping fields for neutral atoms," *Phys. Rev. A*, vol. 35, pp. 1535–1546, Feb 1987.

[68] T. P. Meyrath, "Electromagnet design basics for cold atom experiments," tech. rep., Atom Optics Laboratory, Center for Nonlinear Dynamics, University of Texas at Austin, 2003.

[69] A. M. Steane, M. Chowdhury, and C. J. Foot, "Radiation force in the magneto-optical trap," *J. Opt. Soc. Am. B*, vol. 9, pp. 2142–2158, Dec 1992.

[70] A. Peters, *High precision gravity measurements using atom interferometry*. PhD thesis, Stanford University, 1998.

[71] D. Winester, "Albuquerque 5310 west," tech. rep., National Geological Survey, 2000.

[72] U. Schnemann, H. Engler, R. Grimm, M. Weidemller, and M. Zielonkowski, "Simple scheme for tunable frequency offset locking of two lasers," *Review of Scientific Instruments*, vol. 70, no. 1, pp. 242–243, 1999.

[73] S. Pollock, J. P. Cotter, A. Laliotis, and E. A. Hinds, "Integrated magneto-optical traps on a chip using silicon pyramid structures," *Opt. Express*, vol. 17, pp. 14109–14114, Aug 2009.

[74] K. I. Lee, J. A. Kim, H. R. Noh, and W. Jhe, "Single-beam atom trap in a pyramidal and conical hollow mirror," *Opt. Lett.*, vol. 21, pp. 1177–1179, Aug 1996.

[75] M. Vangeleyn, P. F. Griffin, E. Riis, and A. S. Arnold, "Laser cooling with a single laser beam and a planar diffractor," *Opt. Lett.*, vol. 35, pp. 3453–3455, Oct 2010.

[76] G. W. Hoth, E. A. Donley, and J. Kitching, "Atom number in magneto-optic traps with millimeter scale laser beams," *Opt. Lett.*, vol. 38, pp. 661–663, Mar 2013.

[77] J. A. Rushton, M. Aldous, and M. D. Himsworth, "Contributed review: The feasibility of a fully miniaturized magneto-optical trap for portable ultracold quantum technology," *Review of Scientific Instruments*, vol. 85, no. 12, pp. –, 2014.

[78] C. J. Dedman, K. G. H. Baldwin, and M. Colla, "Fast switching of magnetic fields in a magneto-optic trap," *Review of Scientific Instruments*, vol. 72, no. 11, pp. 4055–4058, 2001.

[79] J. Dalibard and C. Cohen-Tannoudji, "Dressed-atom approach to atomic motion in laser light: the dipole force revisited," *J. Opt. Soc. Am. B*, vol. 2, pp. 1707–1720, Nov 1985.

[80] C. S. Adams and E. Riis, "Laser cooling and trapping of neutral atoms," *Prog. Quant. Electr.*, vol. 21, no. 1, pp. 1–79, 1997.

[81] See Supplemental Material at http://link.aps.org/ supplemental/10.1103/PhysRevApplied.2.054012 for a video demonstrating the cold ensemble exchange.

[82] M. H. Levitt, "Symmetrical composite pulse sequences for {NMR} population inversion. i. compensation of radiofrequency field inhomogeneity," *Journal of Magnetic Resonance (1969)*, vol. 48, no. 2, pp. 234 – 264, 1982.

[83] D. L. Butts, K. Kotru, J. M. Kinast, A. M. Radojevic, B. P. Timmons, and R. E. Stoner, "Efficient broadband raman pulses for large-area atom interferometry," *J. Opt. Soc. Am. B*, vol. 30, pp. 922–927, Apr 2013.

[84] A. Dunning, R. Gregory, J. Bateman, N. Cooper, M. Himsworth, J. A. Jones, and T. Freegarde, "Composite pulses for interferometry in a thermal cold atom cloud," *Phys. Rev. A*, vol. 90, p. 033608, Sep 2014.

[85] P. Berg, S. Abend, G. Tackmann, C. Schubert, E. Giese, W. P. Schleich, F. A. Narducci, W. Ertmer, and E. M. Rasel, "Composite-light-pulse technique for high-precision atom interferometry," *Phys. Rev. Lett.*, vol. 114, p. 063002, Feb 2015.

[86] A. Gauguet, T. E. Mehlstäubler, T. Lévèque, J. Le Gouët, W. Chaibi, B. Canuel, A. Clairon, F. P. Dos Santos, and A. Landragin, "Off-resonant raman transition impact in an atom interferometer," *Phys. Rev. A*, vol. 78, p. 043615, Oct 2008.

[87] T. Saleh, *Fundamentals of Photonics*. Wiley-Interscience Publications, 1991.

[88] M. Abramowitz and I. A. Stegun, *Handbook of Mathematical Functions with Formulas, Graphs, and Mathematical Tables*. Dover, 1965.

[89] S. wey Chiow, T. Kovachy, J. M. Hogan, and M. A. Kasevich, "Generation of 43 w of quasi-continuous 780 nm laser light via high-efficiency, single-pass frequency doubling in periodically poled lithium niobate crystals," *Opt. Lett.*, vol. 37, pp. 3861–3863, Sep 2012.

[90] K. Sakmann and M. Kasevich, "Single shot three-dimensional imaging of dilute atomic clouds," 2014.

[91] J. Lautier, L. Volodimer, T. Hardin, S. Merlet, M. Lours, F. Pereira Dos Santos, and A. Landragin, "Hybridizing matter-wave and classical accelerometers," *Applied Physics Letters*, vol. 105, no. 14, pp. –, 2014.

[92] C. S. Nichols, "An fpga-based microarchitecture for the implementation of quantum gates with trapped ions," Master's thesis, Georgie Institute of Technology, 2012.

[93] A. Keshet and W. Ketterle, "A distributed, graphical user interface based, computer control system for atomic physics experiments," *Review of Scientific Instruments*, vol. 84, no. 1, pp. –, 2013.

[94] E. Mount, D. Gaultney, G. Vrijsen, M. Adams, S.-Y. Baek, K. Hudek, L. Isabella, S. Crain, A. van Rynbach, P. Maunz, and J. Kim, "Scalable digital hardware for a trapped ion quantum computer," 2015.

[95] R. E. Kalman, "A new approach to linear filtering and prediction problems," *Journal of Basic Engineering*, vol. 82, pp. 35–45, Mar 1960.

[96] J. Camparo, "The rubidium atomic clock and basic research," *Physics Today*, vol. 6, p. 33, nov 2007.

[97] S. J. Seltzer and M. V. Romalis, "High-temperature alkali vapor cells with antirelaxation surface coatings," *Journal of Applied Physics*, vol. 106, no. 11, pp. –, 2009.

[98] R. Kawabata, K. Fukuda, and A. Kandori, "Optimized condition for buffer gas in optical-pumped magnetometer operated at room temperature," *Japanese Journal of Applied Physics*, vol. 49, no. 8R, p. 082401, 2010.

[99] M. A. Rosenberry, J. P. Reyes, D. Tupa, and T. J. Gay, "Radiation trapping in rubidium optical pumping at low buffer-gas pressures," *Phys. Rev. A*, vol. 75, p. 023401, Feb 2007.

[100] S.-w. Chiow, T. Kovachy, H.-C. Chien, and M. A. Kasevich, "$102\hbar k$ large area atom interferometers," *Phys. Rev. Lett.*, vol. 107, p. 130403, Sep 2011.

[101] S. L. Braunstein and C. M. Caves, "Statistical distance and the geometry of quantum states," *Phys. Rev. Lett.*, vol. 72, pp. 3439–3443, May 1994.

[102] V. Giovannetti, S. Lloyd, and L. Maccone, "Quantum-enhanced measurements: Beating the standard quantum limit," *Science*, vol. 306, no. 5700, pp. 1330–1336, 2004.

[103] V. Giovannetti, S. Lloyd, and L. Maccone, "Advances in quantum metrology," *Nat Photon*, vol. 5, pp. 222–229, Apr 2011.

[104] J. Hald, J. L. Sørensen, C. Schori, and E. S. Polzik, "Spin squeezed atoms: A macroscopic entangled ensemble created by light," *Phys. Rev. Lett.*, vol. 83, pp. 1319–1322, Aug 1999.

[105] T. Fernholz, H. Krauter, K. Jensen, J. F. Sherson, A. S. Sørensen, and E. S. Polzik, "Spin squeezing of atomic ensembles via nuclear-electronic spin entanglement," *Phys. Rev. Lett.*, vol. 101, p. 073601, Aug 2008.

[106] C. Gross, T. Zibold, E. Nicklas, J. Estève, and M. K. Oberthaler, "Nonlinear atom interferometer surpasses classical precision limit," *Nature*, vol. 464, pp. 1165–1169, Apr 2010.

[107] D. A. Steck, "Rubidium 87 d line data," tech. rep., Theoretical Division (T-8), Los Alamos National Laboratory, Los Alamos, New Mexico, September 2001.

[108] C. D. Wallace, T. P. Dinneen, K. Y. N. Tan, A. Kumarakrishnan, P. L. Gould, and J. Javanainen, "Measurements of temperature and spring constant in a magneto-optical trap," *J. Opt. Soc. Am. B*, vol. 11, pp. 703–711, May 1994.

[109] M. Anwar, D. V. Magalhes, S. T. Mller, M. Faisal, M. Nawaz, and M. Ahmed, "Revisiting the capture velocity of a cesium magneto-optical trap: model, simulation and experiment," *Laser Physics*, vol. 24, no. 12, p. 125502, 2014.

[110] N. Metropolis and S. Ulam, "The monte carlo method," *Journal of the American Statistical Association*, vol. 44, no. 247, pp. 335–341, 1949. PMID: 18139350.

[111] R. Gallager, "Lecture notes in discrete stochastic processes," 2011.